BRIDGING THIOLATES IN METALLOENZYMES: FROM MODEL COMPLEXES TO CATALYTIC SMALL MOLECULE ACTIVATION

A Dissertation

by

ALLEN MICHAEL LUNSFORD

Submitted to the Office of Graduate and Professional Studies of
Texas A&M University
in partial fulfillment of the requirements for the degree of

DOCTOR OF PHILOSOPHY

Chair of Committee,	Marcetta Y. Darensbourg
Committee Members,	Kim R. Dunbar
	Michael Nippe
	Tatyana I. Igumenova
Head of Department,	Simon W. North

December 2016

Major Subject: Chemistry

ABSTRACT

The discovery of cyano-iron carbonyls in the hydrogenases has inspired synthetic efforts to reproduce the active sites of these efficient H_2-producing or H_2-oxidation enzymes. Recent demonstration of the possibility of loading apo-HydA ([FeFe]-H_2ase enzyme) and apo-HydF (maturase protein) with synthetic analogues of the active site provides evidence that small molecular models are indeed the essential catalyst.

Interrogation by EPR spectroscopy of the biohybrids indicate a role for the cyanide in attaching the organometallic unit to a carrier protein; in fact, the cyanide has flipped from its origin in the synthetic diiron unit and inserts into the maturation protein, HydF, resulting in a 4Fe4S docking of the diiron model complex, but placing the cyanide nitrogen next to the 2Fe site. In order to probe the requirements for such cyanide isomerization, we have prepared cyanide-bridged constructs of 3-Fe systems with features related to the organoiron moiety within the loaded HydF protein. The orientation of the CN bridge is determined by the precursors; no cyanide flipping was observed. Density function theory computations find a high barrier accounts for the kinetically controlled products.

In another study, complexes of formulation $(\mu\text{-SCH}_2\text{XCH}_2\text{S})[\text{Fe(CO)}_3]_2$, with X=$CH_2$, CMe_2, CEt_2, NMe, NtBu, and NPh were determined to be photocatalysts for release of H_2 gas from $H_3B{\leftarrow}NHMe_2$. The thermal displacement of $H_3B{\leftarrow}NEt_3$ from photochemically generated $(\mu\text{-SCH}_2\text{XCH}_2\text{S})[\text{Fe(CO)}_3][\text{Fe(CO)}_2(\mu\text{-H})(\text{BH}_2\text{-NEt}_3)]$ by $P(OEt)_3$ was monitored by time-resolved FTIR spectroscopy. Kinetic data reveals an associative mechanism for X=CH_2 and dissociative mechanism for the alkylated and nitrogen bridgehead species. This allows us to rank the catalysts in terms of their B-H unit binding ability, a key step in the dehydrogenation process. The rate of H_2 production from the initially formed $(\mu\text{-}SCH_2XCH_2S)[Fe(CO)_3][Fe(CO)_2(\mu\text{-}H)(BH_2\text{-}NHMe_2)]$ complexes was inversely correlated with the lifetime of the analogous $(\mu\text{-}SCH_2XCH_2S)[Fe(CO)_3][Fe(CO)_2(\mu\text{-}H)(BH_2\text{-}NEt_3)]$ adducts.

Finally, a new series of complexes featuring MN_2S_2 metallodithiolates bound to $Mn/Re(CO)_3X$ were synthesized and characterized as electrocatalysts for CO_2 reduction. Butterfly type structures resulted from binding of the lone pairs of the sulfur atoms to the $Re/Mn(CO)_3X$ unit. Under a CO_2 atmosphere, there was a current enhancement in the cyclic voltammogram which is indicative of CO_2 reduction to CO. Detailed electrochemical experiments are presented along with an appropriate characterization of catalytic processes using cyclic voltammetry and bulk electrolysis. Two complexes will be used as a case study.

DEDICATION

This dissertation is dedicated to my beautiful wife Adriana, whose support and unconditional love has given me the drive to accomplish this work; to my loving parents who have supported me in everything I have done; and to my brothers who have provided encouragement through the whole process.

ACKNOWLEDGEMENTS

First and foremost I would like to thank my advisor, Marcetta Y. Darensbourg for all of the guidance and support she has provided me. You allowed me freedom in determining where to take my projects and provided guidance when necessary which helped in developing me as a scientist and mentor. You were open to any and all ideas (no matter how crazy they sounded at the time) and fostered a relationship where I felt comfortable coming to you for help. I truly admire your passion for teaching and mentorship, a quality which you have passed down to me and I am forever grateful for. I would like to thank my committee members, Professor Kim R. Dunbar, Michael Nippe, and Tatyana I. Igumenova for serving on my committee and providing advice when necessary.

I would like to thank all past and present Darensbourg group members. Tiffany, thank you for mentoring me as an undergraduate and really encouraging me to go to graduate school. You provided a fundamental foundation that really put me a step up in my first year of graduate school. Danielle and Jason, thanks to both of you for being good friends and never getting frustrated at me when I would interrupt you multiple times a day to ask questions. You both provided encouragement and were willing to pass your knowledge onto me. Randara, thanks for being such a great lab-mate. Your smile and uplifting attitude made the day that much better. I would like to especially thank all of the undergraduates that have worked with me. Christopher, Donald, Kristina, Matthew, and Steven you are all so talented and I appreciate how much hard work you accomplished.

Stephen, even though you weren’t a group member, you were such a good friend to both Adriana and me. Thank you for so many good times together and being someone that we could count on for anything.

To my family, there is no way I can thank you enough for the love and support you all have shown me through this long journey. Mom and Dad, I am thankful every day for the way you raised me and the values you instilled in me. Adriana and I are so thankful to both of you for all of the advice in life and providing an oasis away from graduate school that we can escape to occasionally. You both have shown me unconditional love and support as well as what it means to be a Godly man/woman and husband/wife. Whenever things got tough I would always remember “It’s a game. You just got to play the game”. Matthew and James, thanks for the laughs and good times as brothers growing up and as roommates in college. You both have huge hearts and a genuine love for people. Nanny, it has been great getting to know you the last few years. I really appreciate your smile and love and support. Finally, thank you to Grandma and Grandpa for the love and support you both have provided. It was always fun having meals at your house and talking about graduate school and research.

To my wife, Adriana, it is incredible to think that five years ago we started graduate school having no idea that we would find our significant other. You have been with me through the good times and bad and supported me whole heartedly while I pursued this passion of mine and I cannot thank you enough. I am excited to see what the future holds for us, but no matter what I know we will tackle it together.

Finally, I would like to thank my high school chemistry teachers, Mrs. Champagne and Dr. de Pierre. It is because of both of you that I pursued a degree in chemistry in college which eventually led me to graduate school. I admire the passion you have for teaching and mentoring students, encouraging them to think for themselves and develop critical thinking.

NOMENCLATURE

H_2ase	Hydrogenase
H_4MPT^+	Tetrahydromethanopterin
HydA	[FeFe]-Hydrogenase protein
apo-HydA	Protein lacking the 2Fe subsite
TOF	Turnover frequency
GTPase	Enzyme that hydrolyzes guanosine triphosphate
SAM	S-adenosylmethionine
HYSCORE	Hyperfine sub-level correlation spectroscopy
NHC	N-heterocyclic carbenes
Bzl	Benzyl
pdt	1,3-Propanedithiolate
dmpdt	2,2-Dimethylpropanedithiolate
depdt	2,2-Diethylpropanedithiolate
adt	2-Aza-1,3-propanedithiolate
1-CO	$(\mu\text{-pdt})[Fe(CO)_3]_2$
2-CO	$(\mu\text{-dmpdt})[Fe(CO)_3]_2$
3-CO	$(\mu\text{-depdt})[Fe(CO)_3]_2$
4-CO	$(\mu SCH_2N(Me)CH_2S)[Fe(CO)_3]_2$
5-CO	$(\mu SCH_2N(Ph)CH_2S)[Fe(CO)_3]_2$
6-CO	$(\mu SCH_2N(^tBu)CH_2S)[Fe(CO)_3]_2$

Cp	Cyclopentadienyl
dppe	1,2-Bis(diphenylphosphino)ethane
IMe	1,3-Dimethylimidazole-2-ylidene
BArF	Tetrakis[(3,5-trifluoromethyl)phenyl]borate
bme-dach	*N,N*-bis(mercaptoethyl)-1,5-diazacyclo
Fc	Ferrocene
Fc^+	Ferrocenium
$B:A^t$	H_3BNEt_3
$B:A^s$	H_3BNHMe_2
CoA	Coenzyme A
ACS	Acetyl-CoA
TFA	Trifluoroacetic acid
PNNL	Pacific Northwest National Lab
NHE	Normal hydrogen electrode
CODH	Carbon monoxide dehydrogenase
bipy	Bipyridine
ENDOR	Electron nuclear double resonance

TABLE OF CONTENTS

Page

LIST OF FIGURES

LIST OF TABLES

CHAPTER I

INTRODUCTION AND LITERATURE REVIEW

Introduction

A top challenge faced by the current generation of scientists is the need for a clean, sustainable energy source. Fossil fuels currently support the growing energy demand; however, with the ever increasing population and diminishing supply of fossil fuels, the need for a reliable form of renewable energy grows daily. As an extremely efficient energy user and producer; Nature stores solar energy in the form of chemical bonds. Scientists have sought to develop the use of hydrogen as a renewable energy source for years, but as of now the cost of producing hydrogen, currently from CH_4, outweighs the benefits.[1] This is at least partially due to the fact that platinum is currently the fastest and most stable catalyst both for the reduction of H^+ and oxidation of H_2.[2,3] The high cost and insufficient supply of this rare metal makes it impractical to utilize for large scale, long term catalytic hydrogen processing.[4] In order to utilize dihydrogen as an energy source, scientists must turn their attention to the cheaper and sustainable first row transition metals and focus on designing catalysts around these more abundant elements.

Figure I-1 displays the idealized system for the development and storage of power using alternative energy methods.[5-7] Electrons generated from the sun using photosensitizers, solar panels, or wind turbines can be passed to an electrolyzer or transition metal catalyst and convert water into H_2 and O_2. Hydrogen is stored in some form until needed when it can be oxidized into two protons and two electrons by an anode or metal catalyst. The protons are passed through a membrane to the cathode while the electrons flow through an external circuit, generating an electrical current which can be used to power electronics, cars, or houses. Finally, the protons and electrons are combined with oxygen to reform water, closing the cycle. This idealized system requires several catalysts and functioning parts before it can be fully realized.

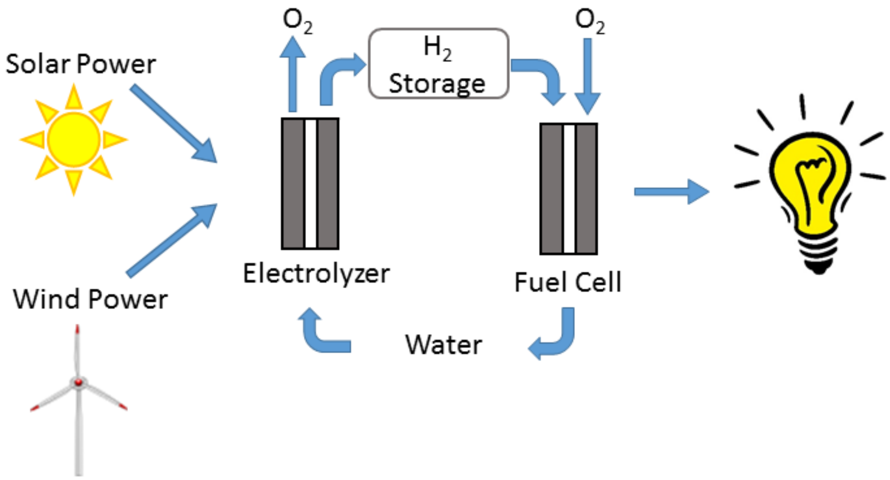

Figure I-1. Idealized system for the generation of electricity from solar or wind power and storage in chemical bonds such as H_2.

Through the evolutionarily perfected metalloenzyme active sites, many of which feature nickel or iron in sulfur-rich coordination environments, Nature provides a guide for synthetic chemists to emulate. Heterobimetallic and homobimetallic molecular compositions utilizing thiolate-sulfurs as bridges are widespread in biology, especially in the active sites of metalloenzymes such as the hydrogenases.[8] These biocatalysts facilitate organometallic-like transformations, using first-row/abundant transition metals, and have inspired scientists of various expertises to address the features that control their mechanisms of action through the development of synthetic analogues. Although the structures of individual components of the biocatalysts that are site-isolated by the protein are readily interpreted from crystallography and various spectroscopies, functional reproductions in small molecule models in the absence of the protein matrix have not been entirely successful. This has led synthetic chemists to design molecules, hopefully catalysts, which resemble the active metal clusters. We also ask the question of whether the role of the protein structure may be reproduced by first and second coordination environments around the metal center.

Before the first crystal structures of [FeFe]- or [NiFe]-H_2ase were reported, the possibility of diatomic CO/CN^- ligands was suggested from vibrational studies conducted by spectroscopists.[9-11] These techniques and spectra aided in the refinement of the X-ray crystal structures as well as identifying, with the help of electrochemistry, various oxidation states in the catalytic cycles.[12,13] In addition from the structures of the various enzymes key features of the active sites are reasonable as indicators of function. Included in these are hydrogen bonding networks, electron transfer pathways, substrate channels, and protein conformational changes.[14,15] Enzymologists, through site directed mutagenesis, have confirmed the assignments of the structural biologists by studying the catalytic efficiency and composition of the enzymes/active sites when key amino acid residues are substituted, vide infra. There exist plenty of reviews where more in-depth information can be gathered, see Table I-1.

Table I-1. List of reviews aimed at the understanding of the maturation, catalytic cycle, structure/function relationship, and classification of [FeFe]-, [NiFe]-, and [Fe]-H_2ase

Short Description	**Reference**
Occurrence, classification, and biological function of hydrogenases	Vignais et al. *Chem. Rev.* **2007**, *107*, 4206
Spectroelectrochemical studies relevant to the mechanism of hydrogenases	De Lacey et al. *Chem. Rev.* **2007**, *107*, 4304
Structure/function relationship of [FeFe]- and [NiFe]-H_2ase	Fontecilla-Camps et al. *Chem. Rev.* **2007**, *107*, 4273
Computational studies of [FeFe]- and [NiFe]-H_2ase	Siegbahn et al. *Chem Rev.* **2007**, *107*, 4414
Enzymes as electrocatalysts for fuel cells	Cracknell et al. Chem. Rev. 2008, 108, 2439
Insights into [FeFe]-H_2ase structure, mechanism, and maturation	Mulder et al. *Structure* **2011**, *19*, 1038
Thorough review of maturation, catalytic cycle, and spectroscopic studies of all three classes of hydrogenases (most up-to-date)	Lubitz et al. *Chem. Rev.* **2014**, *114*, 4081
Overview of the active sites, maturation, structure/function relationship, and model complexes of all three hydrogenases	Bethel and Darensbourg Bioorganometallic Chemistry; Wiley-VCH Verlag GmbH & Co. KGaA: **2014**, p 239

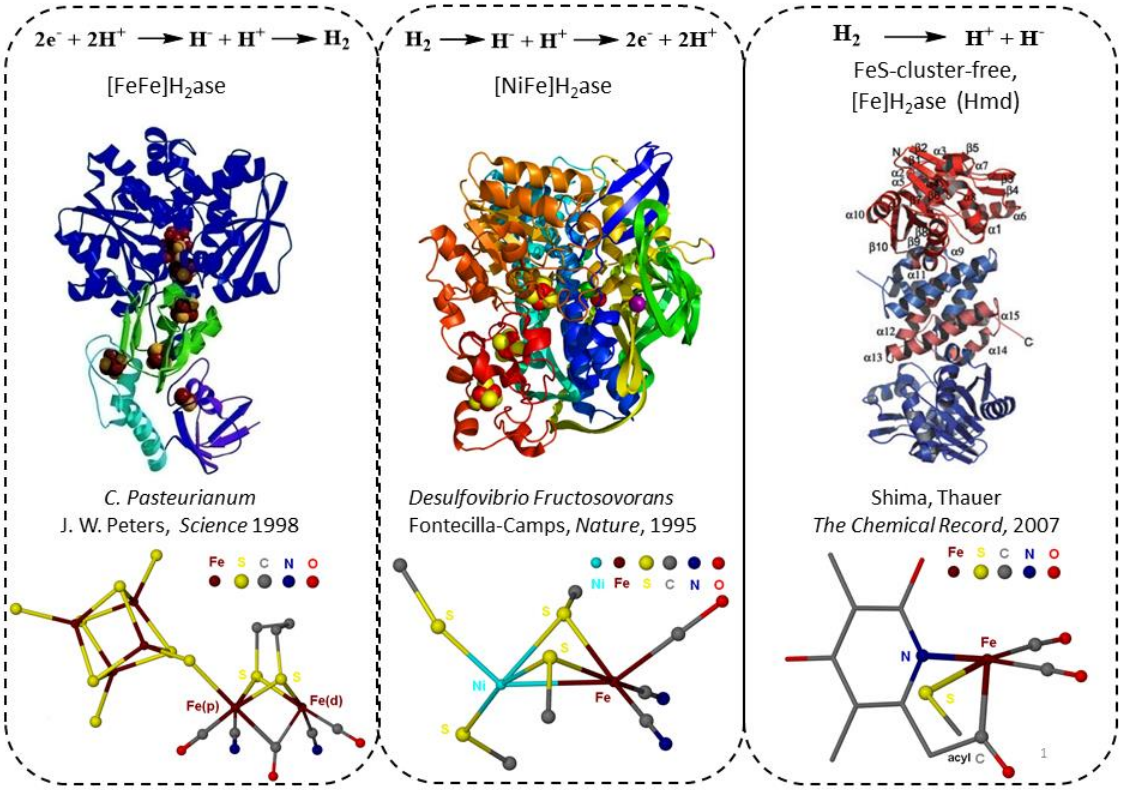

Figure I-2. Structures of [FeFe]-, [NiFe]-, and [Fe]-hydrogenase with the active sites highlighted in ball and stick representation. The preferred direction for catalyzed transformation of protons and electrons are located above the protein structures.

There exists three different categories of hydrogenase enzymes based on the metal content of the active site: [FeFe]-, [NiFe]-, and mono-Fe hydrogenase, Figure I-2.[16-22] Each enzyme offers a different approach to the interconversion of protons, hydrides, hydrogen, and electrons. Mono-Fe hydrogenase is responsible for the heterolytic cleavage of dihydrogen with the hydride being transferred to the H_4MPT^+ cofactor and the proton being transferred to a basic site somewhere in the active site.[18] While the other two hydrogenases involve some redox change at the metal center, mono-Fe hydrogenase is redox inactive (at least at the single iron active site). Both the [FeFe]- and [NiFe]-H_2ase have the capability to reversibly reduce H^+ or oxidize H_2, however many organisms with a requirement for electron removal via proton reduction utilize [FeFe]-H_2ase to produce H_2, while others that have a need for electrons produced from H_2 oxidation more typically call upon the [NiFe]-H_2ase.[14,23] Nevertheless H_2ases, as in all enzymes, lower the barrier for two proton and two electron conversions in both directions.

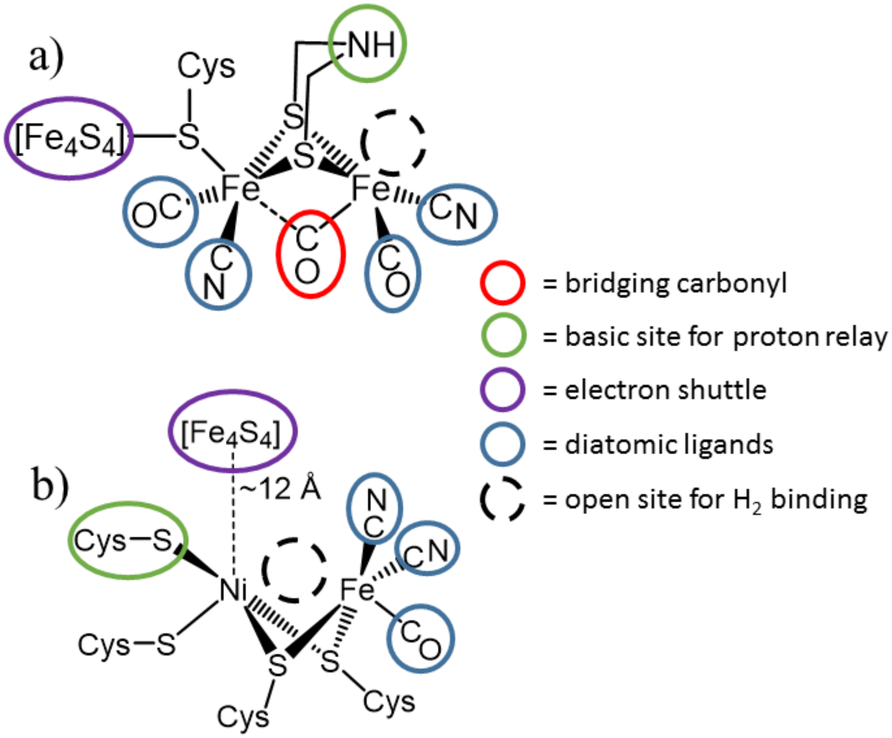

Figure I-3. Features of the active sites of a) [FeFe]- and b) [NiFe]-H_2ase that aid in catalytic activity. The bridging thiolates also provide a basic site for proton relay as well as electronic communication between both metals.

The diiron hydrogenase protein, [FeFe]-H_2ase or HydA, is a metalloenzyme found in many microorganisms that is biased towards hydrogen production. There are notable features of the 2Fe2S subsite within the 6Fe, H-cluster that facilitates proton uptake and combination with electrons, Figure I-3a.[14,24] One feature that promotes hydrogen metabolism in [FeFe]-H_2ase is the dithiolate linker (S-CH_2-X-CH_2-S). In early crystal structures, the identity of this central atom was ambiguous and was thought to be CH_2, O, or NH, however DFT and early pulsed-EPR studies gave evidence which pointed towards the assignment being NH resulting in a dithiomethylamine (S-CH_2-NH-CH_2-S) linker.[25-27] This was further confirmed through the synthesis of hybrid enzymes where apo-HydA (enzyme lacking the 2Fe2S active site) was loaded with synthetic model complexes containing the three different dithiolate linkers, vide infra.[28,29] This NH unit, termed a pendant base, is oriented above the "open site" on the distal iron (iron furthest from the 4Fe4S cluster) and is responsible for directing protons to the catalytically active distal iron. Numerous complexes featuring pendant bases have been synthesized, both in hydrogenase models as well as homogeneous catalysts, and attest to the functional role of the NH in [FeFe]-H_2ase.[30-33]

The oxidation state of the irons in the isolated enzyme are Fe^IFe^{II}. Both iron centers are coordinated by a CO and a CN ligand which are required to stabilize low valent, low spin iron, in the Fe^IFe^I and Fe^IFe^{II} oxidation states within the catalytic cycle. A unique aspect of the H-cluster is a shared third carbonyl ligand between the two irons which permits an "open site" to be exposed on the distal iron. The generation of this open site is thought to facilitate the high catalytic activity of [FeFe]-H_2ase and is the location of protonation and subsequent hydrogen generation.[24] This configuration is rarely seen in synthetic organoiron compounds of similar, (µ-SRS)$[Fe(CO)_2L]_2$, composition and is referred to as the “rotated” geometry.[9] The protein super structure is expected to stabilize this rotated isomer, which is achieved by bulky, hydrophobic groups found in the second coordination sphere making the rotated structure more favorable.[34] Once the CO unit is in the rotated position, methionine, lysine, and cysteine residues form hydrogen bonds to the cyanide ligands, the bridging carbonyl, and the aza-dithiolate linker and “lock” this structure into place throughout the redox states of the enzyme, see Figure I-4a.[35] To prove how important these interactions are, the amino acids were mutated for alanine or leucine which lack the hydrogen bonding capability. Mutating Lys 228, which hydrogen bonds to the cyanide ligand, results in no detectable H-cluster as determined by EPR and IR spectroscopy demonstrating the role the hydrogen bonding network plays in stabilizing and immobilizing the 2Fe2S unit.[36] When Met 415 or Met 223 are mutated for Leu, the H-cluster is intact, but the activity for H_2 production drops to 5% and 15% respectively, again highlighting the role of hydrogen bonding in the catalytic cycle.[36] Interestingly, the only bonding connection the 2Fe subsite has to the [FeFe]-H_2ase protein is through a bridging cysteinal sulfur connecting the 4Fe4S cluster to the 2Fe unit.

Similarly, [NiFe]-H_2ase has features which are identified as important to catalysis, see Figure I-3b.[17,19,37] When activated there exists an open site positioned between the two metal centers allowing for the binding of H_2 within close proximity to the S-Cys. This sulfur atom acts as a pendant base to abstract a proton from H_2 in the catalytic cycle as confirmed by X-ray crystallography, DFT calculations, and spectroscopy.[27,37-39] One carbon monoxide and two cyanide ligands complete the coordination sphere of the iron center.[40] The strong σ-donating ability of cyanide and the good π-accepting ability of carbon monoxide assist in maintaining a low spin Fe^{2+}. These diatomic molecules also serve to anchor the active site in the optimum confirmation for catalytic activity through hydrogen bonds to the surrounding amino acid residues, see Figure I-4b.[39,41,42] Mutation of these amino acids to residues which cannot form hydrogen bonds saw a shift in the CN^- stretching frequencies, demonstrating the role the protein matrix plays in interacting with the diatomic ligands.[43] These interactions are thought to be important for tuning the electronics and redox potential of the two metals in the active sites. The $Ni(\mu\text{-}SCys)_2Fe$ core appears in a butterfly confirmation with the two sulfurs from the cysteines bridging the nickel and the iron just as in [FeFe]-H_2ase. Two other S-Cys coordinate the nickel center; thus the nickel site is covalently attached to the protein.

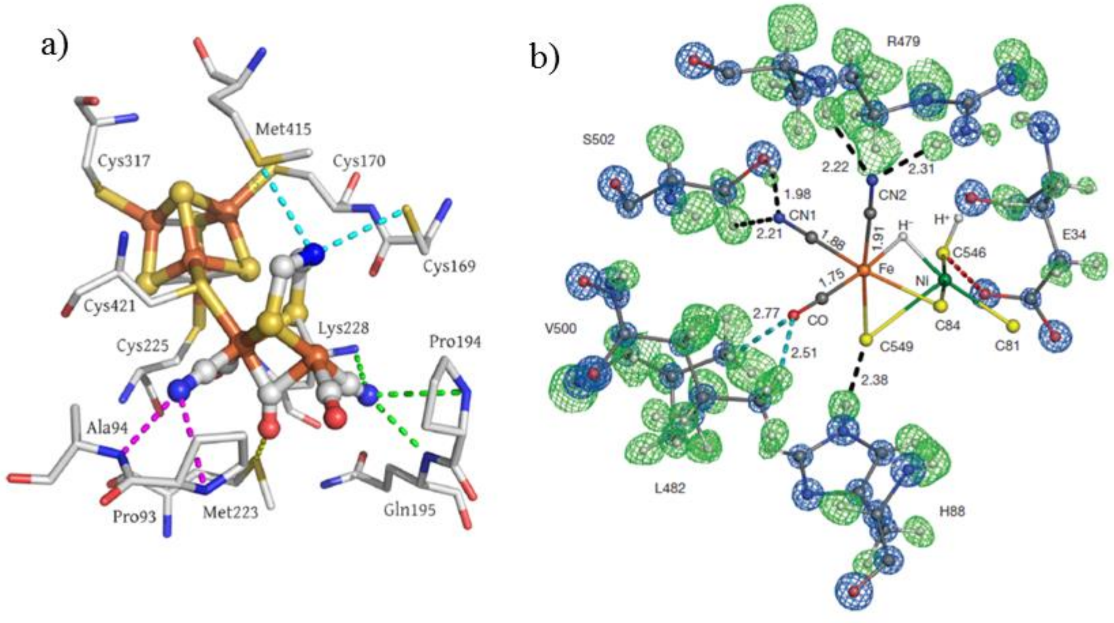

Figure I-4. Active sites of a) [FeFe]-H_2ase (Reprinted with permission from Siebel, J. F.; Adamska-Venkatesh, A.; Weber, K.; Rumpel, S.; Reijerse, E; Lubitz, W. *Biochemistry* **2015**, *54*, 1474. Copyright **2015** American Chemical Society.)[35] and b) [NiFe]-H_2ase (Reproduced with permission from Ogata, H.; Nishikawa, K.; Lubitz, W. *Nature*, **2015**, *520*, 571. Copyright **2015** Macmillan Publishers Limited)[39] highlighting the importance of hydrogen bonding in stabilizing the catalytically relevant geometries.

There are other features of the [FeFe]- and [NiFe]-H_2ase enzymes that facilitate the catalytic functions. A series of iron-sulfur clusters aid in the redox chemistry of the enzymes by shuttling electrons from the outside of the protein to the active sites which are buried inside the protein to shield the oxygen intolerant active sites.[39,41,44] In [FeFe]-H_2ase, the last 4Fe4S cluster is directly attached to the active site and its redox activity is inseparable from the redox activity of the 2Fe2S subsite.[45] Similarly there exists a series of basic amino acids that transport protons to and from the active sites as well as a hydrophobic gas channel for H_2 storage.[37,46,47] When bulkier amino acid residues are

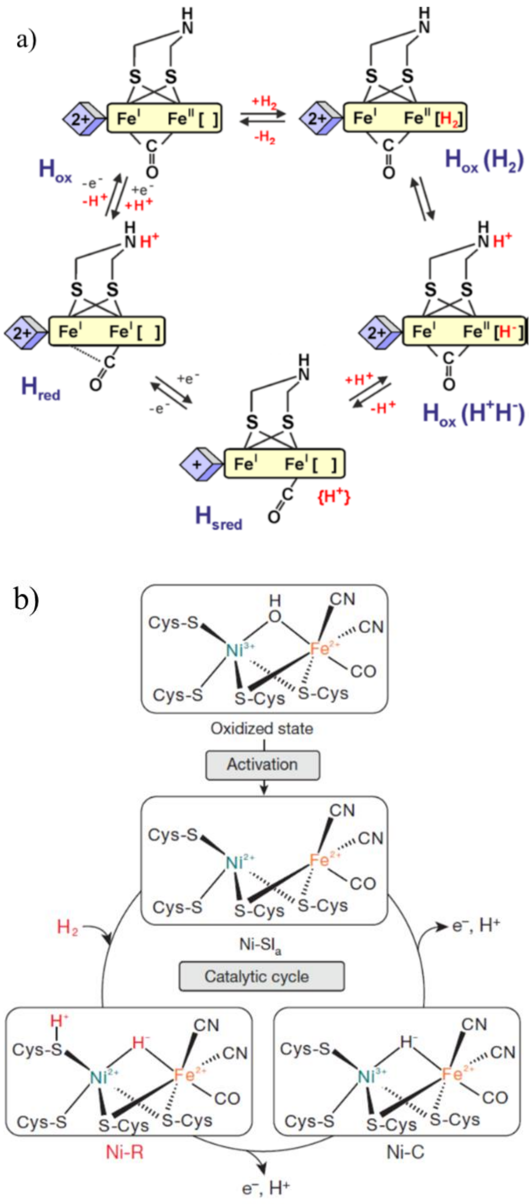

Figure I-5. Proposed catalytic cycle for the reversible reduction of protons to hydrogen as well as the oxidation of hydrogen by a) [FeFe]-H_2ase (Reprinted with permission from Lubitz, W.; Ogata, H.; Rüdiger, C.; Reijerse, E. *Chemical Reviews* **2014**, *114*, 4081. Copyright **2014** American Chemical Society)[41] and b) [NiFe]-H_2ase (Reproduced with permission from Ogata, H.; Nishikawa, K.; Lubitz, W. *Nature*, **2015**, *520*, 571. Copyright **2015** Macmillan Publishers Limited)[39]. The purple cubane represents the [4Fe4S] cluster directly attached to the active site.

mutated into these gas channels, catalysis is slowed down dramatically pointing towards the conclusion that not only do these gas channels exist but that they are important in the features of the molecular machinery.[48]

These characteristics of the active site have led to what is now regarded as the catalytic cycle for [FeFe]-H_2ase that is presented in Figure I-5a.[49-51] Starting at the $Fe^{I}Fe^{II}$ resting state of the enzyme (H_{ox}), concerted proton/electron addition generates the $Fe^{I}Fe^{I}$ oxidation state with the ammonium cation at the bridgehead. The second electron, generating the H_{sred} state, is added at the 4Fe4S cluster and leads to uptake of a proton at the distal iron center. A two-electron reduction, one electron derived from the distal iron and one electron from the 4Fe4S cluster, of the proton generates a metal-hydride intermediate. Subsequent protonation of the hydride to form hydrogen closes the catalytic cycle. The reaction is reversible, however [FeFe]-H_2ase is said to be biased towards hydrogen production with a TOF between 6000-9000 s^{-1} to rid the biological system of excess electrons.[52]

Figure I-5b displays the proposed intermediates of the catalytic cycle for H_2 oxidation by [NiFe]-H_2ase based on X-ray crystallography, spectroscopy, and DFT computations.[17,19,27,37-39] Activation to generate the catalytically active species is required to remove the bridging OH group which is featured in the isolated, oxidized form of the enzyme. Dihydrogen is then heterolytically cleaved to form a protonated S-Cys and a bridging hydride known as the Ni-R state. Interestingly, this state has recently been isolated and crystallized.[39] Here the lone pair of the S is acting as the pendant base, similar to the NH group of [FeFe]-H_2ase. From Ni-R, a one electron reduction results in the Ni-

C state featuring a bridging hydride $Ni^{3+}(\mu\text{-}H)Fe^{2+}$ and removal of the proton from the S-Cys. Interestingly, all redox activity occurs on the nickel center implying the iron is present to tune the electronics of the nickel and support the bridging hydride ligand. Another reduction and proton removal reforms the initial Ni-SI state and completes the catalytic cycle. Similar to [FeFe]-H_2ase, the reaction is reversible but [NiFe]-H_2ase seems to be the hydrogenase of choice by nature when the cell or organism needs to produce electrons via oxidation of H_2.

Biosynthesis of Native [FeFe]-H_2ase

While the structure-function relationship of the H-cluster is well understood, the biosynthesis of the 2Fe2S unit still has many unanswered questions. A typical assumed biosynthetic route generates the 4Fe4S clusters present in apo-HydA whereas the 2Fe2S unit is built outside the protein and inserted at a later time.[15,53] The presence of both carbon monoxide and cyanide ligands implies a maturase system where the assembly of the active site is well contained and systematic in order to limit the possibility of toxic free cyanide or carbon monoxide causing damage to the cell or organism. The biosynthesis mechanism expressed by Figure I-6 assumes validity of the David Britt et al. hypothesis that the iron-diatomic ligand moieties that are precursors to the 2Fe subsite are both derived from a single iron attached to a 4Fe4S cluster subsequently assembled on apo-HydF.[54] It should be mentioned at this point (2016) the alternative argument involves derivation from a 2Fe2S cluster.[15,55]

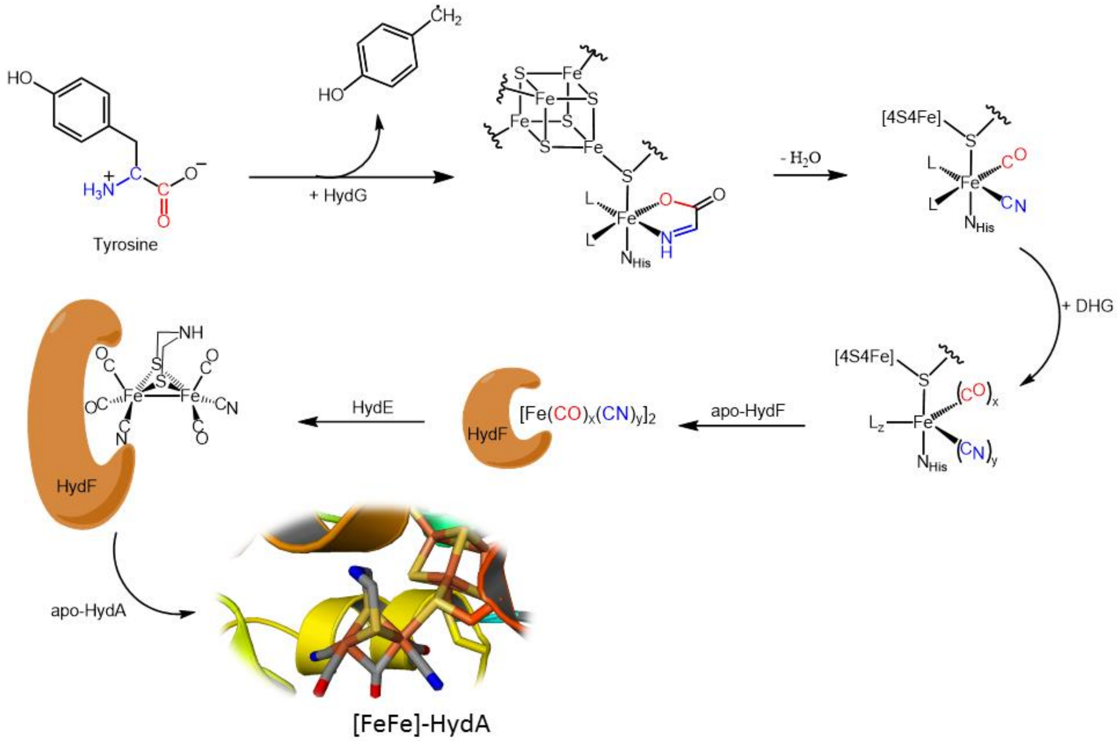

Figure I-6. Proposed biosynthetic scheme for the synthesis of the 2Fe2S unit of the H-cluster catalyzed by the maturase proteins HydG. HydE, and HydF with final insertion into apo-HydA.[54,56-58]

There are three maturase proteins responsible for the biosynthesis of HydA which are HydE, HydF, and HydG.[15,41] HydF is a GTPase and is thought to be a scaffold protein where the 2Fe subunit is assembled and ultimately inserted into apo-HydA.[59] HydG is a radical SAM enzyme and is responsible for the synthesis of the diatomic ligands around the 2Fe unit from the breakdown of tyrosine.[56] The dehydroglycine moiety, generated from the cleavage of tyrosine, binds to a "dangling" iron attached to a 4Fe4S cluster of HydG followed by elimination of H_2O to produce the CO and CN ligands.[54,57,58] This dangling iron in HydG is unique to GTPases and was determined to be present from an X-ray crystal structure.[54] While the subsequent steps are speculative, it can be imagined that two of these dangling irons might combine on HydF to generate the 2Fe subunit.

It has recently been shown that apo-HydF is able to accept synthetic 2Fe model complexes containing CN ligands, however the IR spectra in the diatomic region of these biohybrids does not match that of the natural maturase protein.[28] Despite this difference, the ability of HydF to incorporate diiron constructs points towards its aptitude to act as a maturase protein and receive a 2Fe subunit from HydG.

There is some mystery as to the role of HydE which is required for maturation; however the reactants involved in its catalysis are unknown.[15,60] If HydF is a scaffold protein, and HydG is responsible for the diatomic ligand synthesis this implies the possible role of HydE is to develop the dithiolate linker. Recently, Rohac and coworkers demonstrated that HydE is capable of cleaving a sulfur-carbon bond of 1,3-thiazolidines by formation of a carbon centered radical followed by attack of a sulfur atom on a thioether.[61] While 1,3-thiazolidines are not reactants in the biosynthesis of the 2Fe subunit, this proves that HydE is capable of manipulating atoms located in the dithiolate linker. Finally, the preformed diiron cluster is transferred to apo-HydA through an open cavity to the 4Fe4S cluster followed by collapse of the cavity and CO displacement by a cysteinal sulfur to form the fully assembled HydA.[55,62]

Biohybrids Derived from Synthetic $(\mu\text{-SRS})[Fe(CO)_2CN]_2^{2-}$

While the crystal structure of [FeFe]-H_2ase has been known since 1998 the identity of the central atom of the dithiolate linker has only been unambiguously assigned in the last few years.[14] This came about through a unique study which involves the insertion of synthetic analogues resembling the active site of [FeFe]-hydrogenase into apo-HydA, that is, HydA lacking the 2Fe2S portion of the H-cluster. In the first paper published, Berggren et al. demonstrated that the diiron complexes with NH, O, or CH_2 at the central atom of the dithiolate linker could be bound to the 4Fe4S cluster of apo-HydF through the cyanide ligand by simply incubating apo-HydF with a concentrated solution of the appropriate diiron precursor.[28] Exposing apo-HydA to this biohybrid resulted in transfer of the diiron unit to the cysteinal sulfur of the 4Fe4S cluster of apo-hydA concomitant with stoichiometric CO dissociation as confirmed by analysis of the headspace of the reaction mixture using gas chromatography. The spectroscopic features of the EPR and IR spectra as well as the redox potentials match the natural enzyme, indicating the oxidation state of the two irons as well as the bridging CO match that of HydA in nature. Interestingly, switching between NH, O and CH_2 does not alter this observation implying a similar structural arrangement of the synthetically derived H-cluster to that of the natural enzyme. This was later confirmed by Esselborn et al. in a structural analysis of the three semisynthetic HydA analogues as well as a fourth featuring a sulfur at the central atom of the dithiolate bridgehead.[63] The X-ray crystal structures revealed the protein matrix was nearly identical in all four biohybrids. In another paper dealing with the synthesis of biohybrids by Esselborn et al., it was reported that there is no need to first insert the synthetic diiron complex into HydF but it can spontaneously add into, and activate, apo-HydA.[29] This provides a much simpler route to study these artificial HydA analogues.

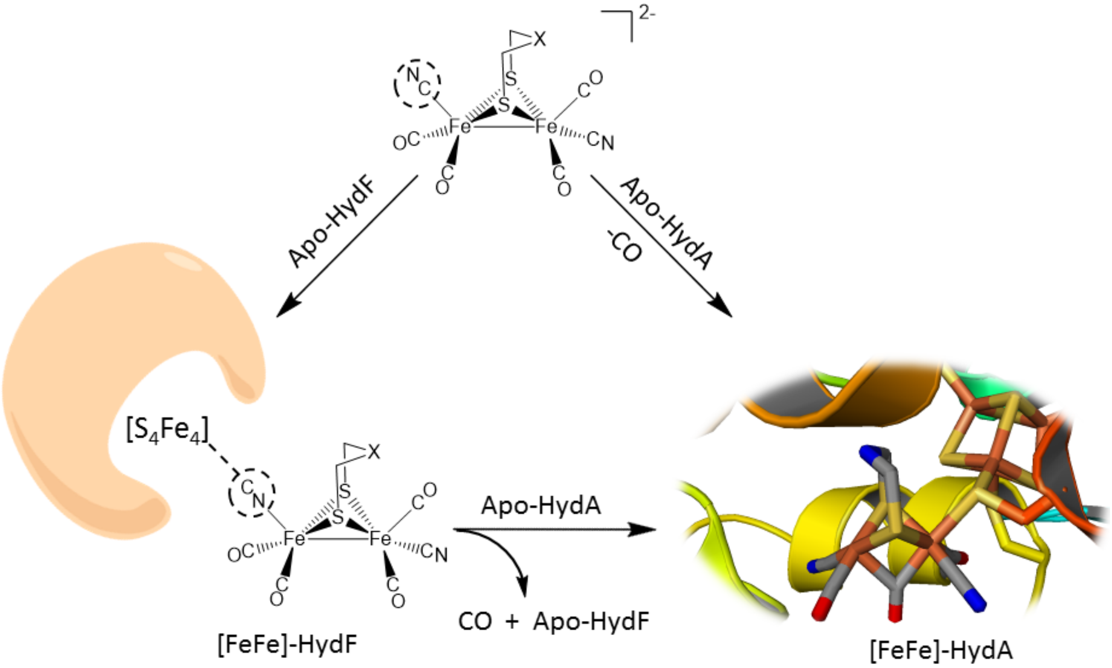

Figure I-7. Hydrogenase precursor protein, HydF, loaded with synthetic analogues of the active site and hydrogenase enzyme, HydA.

While insertion of model complexes to generate HydA is interesting and provides new routes to study the [FeFe]-H_2ase enzyme it does not offer any insight into the identity of the central atom of the dithiolate linker in the natural protein. This assignment arose from the H_2 release studies of the biohybrids using reduced methyl viologen as an electron source and water as a proton source. When compared to the natural enzyme, 100% of the proton reduction activity was observed with the biohybrid containing the NH bridgehead while almost no activity was seen for the CH_2 or O bridgehead.[28,29] Since it was observed that there is no structural differences in the protein or active site between the different biohybrids in the crystal structure, the difference in catalytic activity can be attributed to the identity of the central atom of the dithiolate linker which confirms unambiguously that it is NH in the natural enzyme.

It was clear from the IR spectrum that the synthetic analogue was docked into the HydF protein through the cyanide of the diiron unit to a 4Fe4S cluster. However, a fascinating discovery was made when studying the adduct by pulsed EPR spectroscopy. As is shown in Figure I-7, the cyanide had undergone linkage isomerism so that now the carbon end is bound to the 4Fe4S cluster where as it was bound to the diiron unit in the precursor complex.[28] This was determined by substituting the naturally abundant C-12 cyanide with the I = ½ C-13 nuclei and studying the adduct using HYSCORE spectroscopy. The simulation of the resulting spectrum led them to believe that the unpaired electron on the 4Fe4S cluster was strongly coupled to the C-13 nucleus of the bridging cyanide supporting the cyanide isomer assignment depicted in Figure I-7.

The ability to insert model complexes into apo-HydA has sparked a drive to further understand the roles that features of the active site play in catalysis with the intent of possibly developing an artificial system that exceeds the catalytic activity of the natural enzyme. Several analogues were successfully introduced into apo-HydA as seen in Figure I-8 in order to probe the effects on hydrogen production.[35] Variations were made in the steric bulk of the dithiolate linker to examine if the binding pocket of the H-cluster could support a bulkier bridgehead by placing methyl groups at either the amine or the elbow carbon of the bridgehead. Mono cyanide derivatives were also introduced to probe the function that the second cyanide might play. None of the subsequent biohybrids could approach the activity of HydA even though all of the listed complexes were successfully introduced as was evident by IR and EPR spectroscopy. Interestingly, the mono-cyanide derivative with the NH bridgehead had ~1/2 the activity for hydrogen production compared to the natural enzyme. Nevertheless, insight into the roles the conformational and functional features of the H-cluster might play was expanded.

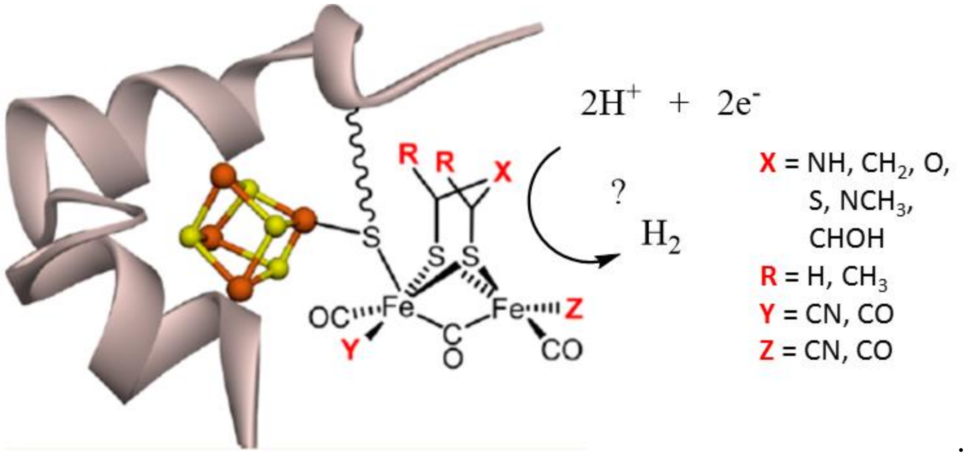

Figure I-8. Alternative model complexes inserted into apo-HydA. (Adapted with permission from Siebel, J. F.; Adamska-Venkatesh, A.; Weber, K.; Rumpel, S.; Reijerse, E; Lubitz, W. Biochemistry **2015**, *54*, 1474. Copyright **2015** American Chemical Society.)

Model Complexes

The constitution study with the synthetic 2Fe subsites and the fact a synthetic complex could insert into apo-HydA has reinvigorated synthetic efforts by organometallic chemists to continue their quest for diiron and nickel iron compounds that can do this chemistry. Organometallic [2Fe2S] clusters which resemble structural characteristics of the active site have been known since the late 1920’s with work by Reihlen including the ability of these model complexes to act as electrocatalysts for proton reduction albeit they were very poor compared to today's standards.[64] While the enzymes themselves are effective catalysts when supported on electrodes or in solution, there are many drawbacks to using the proteins in hydrogen metabolizing catalytic systems.[65-67] It is difficult to produce large quantities of the enzyme, many of the active sites suffer from extreme oxygen intolerance, and it is difficult to get a high catalyst density deposited on the electrode due to the large size of the protein. This has led synthetic chemists to design small molecules that resemble the active site both in function and catalytic activity.

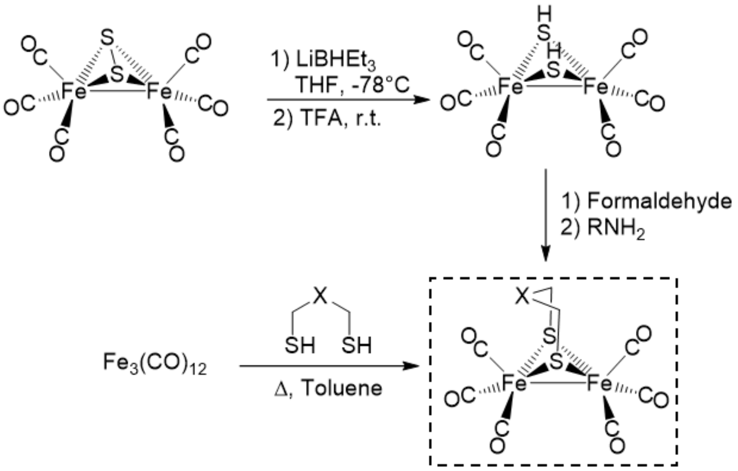

Figure I-9. Synthesis of the generic starting material (μ-SCH_2XCH_2S)[$Fe(CO)_3$]$_2$ via two different routes depending on the identity of the central atom.

The ultimate precursor to hundreds of model complexes is seen in Figure I-9 and can be synthesized via two different routes depending on the nature of the central atom of the dithiolate linker.[68] A simple reductive elimination of hydrogen from a dithiol containing organic molecule by an $Fe(CO)_3$ source such as $Fe_3(CO)_{12}$ results in the hexacarbonyl species in a decent yield.[69-71] This works efficiently for the all carbon bridgeheads or the oxygen/sulfur containing linkers but is more complicated when the central atom is nitrogen, owing to the availability or properties of the organic dithiols. An alternate route involves the reduction of a disulfide bond of $Fe_2S_2(CO)_6$ followed by protonation and condensation with formaldehyde and a primary amine.[72-74] Due to the simplicity of this route and the availability of a large number of primary amines, scores of derivatives featuring modifications of the nitrogen bridgehead have been synthesized for a variety of applications.

There are two fluxional processes important to the [FeFe]-H_2ase model complexes which can be probed using variable temperature NMR spectroscopy: a) the boat/chair interconversion of the six member ring generated from the FeS_2C_2X unit; and b) rotation/exchange of the CO ligands on either $Fe(CO)_3$ unit.[69,75,76] These processes have possible influence in ligand substitution rates/mechanism and catalytic oxidation/reduction reactions. My application of these processes is further explained in Chapter IV.

Hexacarbonyl model complexes can be further modified by substituting CO with some better, L-type donor ligand such as phosphines, cyanides, and carbenes just to name a few. Addition of one equivalent of the incoming ligand such as PR_3 and N-heterocyclic carbenes (NHCs) results in replacement of one CO in a matter of minutes while substitution of a second CO requires a second equivalent of ligand as well as elevated temperatures and increased reaction time.[77-81] Interestingly, CN^-/CO intermolecular exchange occurs at low temperatures and easily gives the disubstituted product.[69,82,83] In both cases, the second CO is displaced from the Fe adjacent to the first. Alternate methods for CO displacement include photolysis using either a sun lamp or UV lamp, or oxidation of the CO to CO_2 using trimethylamine N-oxide. Understanding the substitution pattern of these model complexes allows synthetic chemists to tune the electronic and steric character of the diiron unit. Also, it provides insight into strategies whereby the diiron complexes might be attached or anchored to photosensitizers, solid state supports, or electrodes for further catalytic study.[84-87]

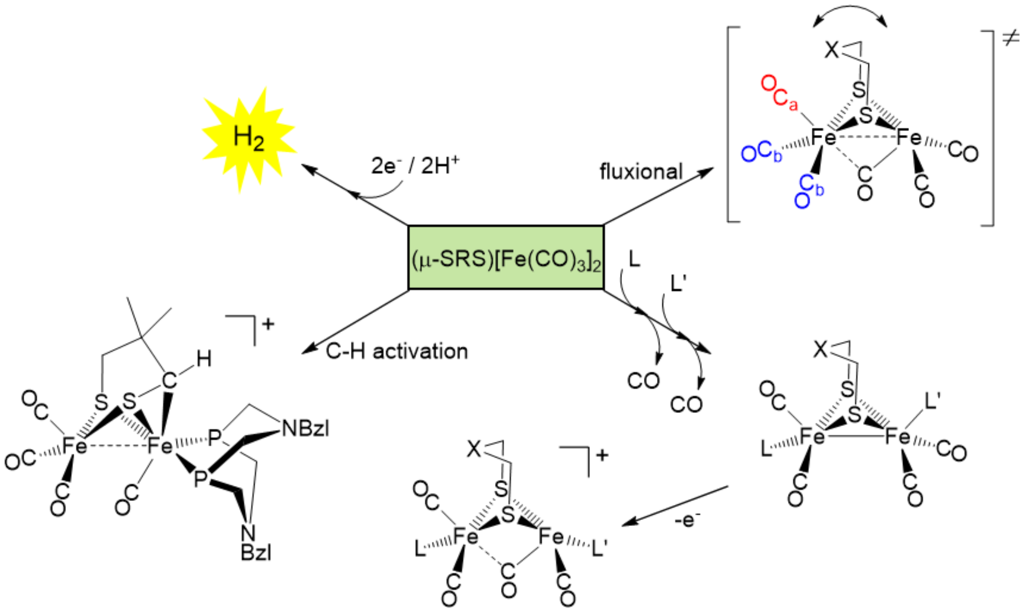

Figure I-10. Parent (μ-SRS)[Fe(CO)$_3$]$_2$ complex and reactivity including proton reduction, C-H activation, ligand substitution, and fluxional processes described and referenced in text.

These small diiron complexes exemplified by the center molecule of Figure I-10 have been said to be deceptively simple. They undergo a variety of structural changes as well as intermolecular reactions with exogenous ligands. By altering the complexes with ancillary ligands, or activating them by oxidation/reduction or photolysis, a wide range of catalytic and stoichiometric activation of small molecules have been achieved. The most widely studied reaction is the reduction of protons to hydrogen by either photocatalytic or electrocatalytic systems.[76,88,89] A majority of the diiron model complexes can accomplish this reaction albeit at varying turnover frequencies (TOF) and overpotentials. Even though the natural [FeFe]-H_2ase enzyme can oxidize hydrogen to two protons and two electrons, the small molecule analogues or model complexes require much more tuning to accomplish this reaction in a catalytic fashion. Rauchfuss et al. installed an NBenzyl group at the bridgehead, a redox active ferrocene derivative, and a diphosphine ligand to model the pendant base, 4Fe4S cluster, and low oxidation potential of the natural enzyme, respectively. This particularly elegant (and fragile) molecule was the first example of a diiron model complex that could catalytically oxidize hydrogen.[90] Hexacarbonyl complexes were also shown to catalytically reduce O_2 to H_2O_2 as well as release H_2 from amine-boranes. Finally, stoichiometric C-H activation was achieved by incorporating a P_2N_2 ligand into the diiron framework and doubly oxidizing the complex with ferrocenium.[91] A proton was abstracted from the elbow carbon of the dithiolate linker by the nitrogen of the pendant base and a metal carbon three membered ring was formed which was confirmed by x-ray crystallography.

The work herein will focus on the characterization of bridging cyanide complexes featuring the diiron starting materials described above and bridged to a second metal center. Chapter III aims at understanding the electronic and steric factors required to synthesize bridging cyanide isomers and the stability associated with each. Spectroscopic coupling constants from an EPR active species generated by bulk electrolysis are compared to the HydF biohybrid where cyanide isomerization is thought to take place. This study also exemplifies the possibility of using CN^- as a docking agent.

In Chapter IV, a photocatalytic reaction for diiron hydrogenase model complexes is explored, namely the dehydrogenation of amine-boranes to release hydrogen. This reaction has implications in hydrogen storage materials and the binding strength of the amine-boranes to an open site on iron, as determined by competitive binding studies, is correlated with the hydrogen production abilities of six different dithiolate linker hexacarbonyl species.

New heterobimetallic complexes featuring MN_2S_2 complexes bound to $Mn/Re(CO)_3$ moieties are presented in Chapter V and their applications to electrochemical CO_2 reduction to CO is described. Procedures to understand and completely describe cyclic voltammograms and bulk electrolysis experiments are developed in Chapter VI for two complexes which model certain features of the [FeFe]- and [NiFe]-H_2ase. Finally, Chapter VII is an overview of my perspective of how this field of base metal catalysis using nature as inspiration for synthetic approaches to the diverse ligand fields that tune the multi-metallic catalysts has advanced during my time as a graduate student in the chemistry department at Texas A&M University.

CHAPTER II

GENERAL EXPERIMENTAL DETAILS

General Procedures

All reactions and manipulations were performed using standard Schlenk-line and syringe/rubber septa techniques under N_2 or in an Ar atmosphere glovebox. Solvents were purified and degassed via a Bruker solvent system. Reagents were purchased from commercial sources and used as received.. The diiron complexes used in this study were synthesized following previously published procedures; **1**-CO,[92] **2**-CO,[75] **3**-CO,[75] **4**-CO,[72] **5**-CO,[72] **6**-CO,[72] $[(\eta\text{-}C_5H_5)Fe(CO)_2THF][BF_4]$,[93] $(\eta\text{-}C_5H_5)Fe(CO)_2CN$,[94] $(\eta\text{-}C_5H_5)Fe(dppe)CN$,[95] $(\mu\text{-pdt})[Fe(CO)_3][Fe(NO)(IMe)(CO)][BF_4]$,[77] $(\mu\text{-pdt})[Fe_2(CO)_5CN][Na]$,[96] $(\mu\text{-pdt})(\mu\text{-H})[Fe(CO)_2PMe_3]_2[PF_6]$,[97] NaBArF,[98] $[(\eta\text{-}C_5H_5)Fe(CO)_2PMe_3][BF_4]$,[99] and $(\mu\text{-pdt})[Fe_2(CO)_5PMe_3]$[100]. The MN_2S_2 complexes used in Chapter V were synthesized following previously published procedures; Fe(NO)(bme-dach)[101], Co(NO)(bme-dach)[101], and Ni(bme-dach)[102]. Elemental analyses was performed by Atlantic Microlab, inc., Norcross, Georgia, United States. Electrospray ionization mass spectrometry (ESI-MS) was performed by the Laboratory for Biological Mass Spectrometry at Texas A&M University. Infrared spectra were recorded on a Bruker Tensor 37 spectrometer using a CaF_2 solution cell of 0.2 mm path length. A Bioanalytical Systems 100 electrochemical workstation with a glassy carbon working electrode (0.071 cm^2) and a platinum wire auxiliary electrode was used to conduct the electrochemical analysis of all compounds. ^1H and ^{31}P NMR spectra were recorded on an Inova 400 MHz superconducting NMR instrument operating at 400 MHz and 161.92 MHz respectively. ^{1}H spectra were referenced to residual solvent while ^{31}P spectra were referenced to external H_3PO_4.

Cyclic Voltammetry

A standard three electrode cell under an Ar atmosphere at room temperature was used to obtain all voltammograms. Cyclic voltammograms of all complexes as well as starting materials were recorded in 2 mM solutions with 100 mM [n-Bu_4N][PF_6] as the supporting electrolyte in the solvent indicated in the text. The potentials were measured relative to a Ag/$AgNO_3$ electrode using a glassy carbon working electrode, and are referenced to Cp_2Fe/ Cp_2Fe^+ ($E_{1/2}$ = 0.00 V). Bulk electrolysis experiments are described in the experimental for Chapter VI.

X-ray Structure Analysis

Low temperature (150 K) X-ray data was obtained on a Bruker Apex-II CCD based diffractometer (Texas A&M University) (Mo sealed X-ray tube, K_α = 0.71073 Å) for complexes A-D. Crystal samples were coated in mineral oil, affixed to a Nylon loop, and placed under streaming N_2. Space groups were determined on the basis of systematic absences and intensity statistics, and structures were solved by direct methods and refined by full-matrix least-squares on F_2. All non-hydrogen atoms were refined with anisotropic thermal parameters. H atoms were placed at idealized positions and refined with fixed isotropic displacement parameters; anisotropic displacement parameters were employed for all non-hydrogen atoms. The following programs were used: data collection, APEX2;[103] data reduction, SAINT;[104] absorption correction SADABS;[105] cell refinement

SHELXTL;[105] structure solutions, SHELXS-97;[105] and structure refinement, SHELXL-97.[105] The final data presentation and structure plots were generated in X-Seed Version 2.0.[106]

Experimental Details for Chapter III

Computational Studies

Gaussian 09 Version D01[107] was used to execute all the calculations unless noted otherwise. The TPSS functional was applied for most calculations except EPR parameter determination, in which case functional B3LYP[108] was utilized. Triple-ζ 6-311++G(d,p)[109,110] basis set was used for all non-metal atoms, except the methyls and phenyls on phosphines in complex **B** and **D**, for which double-ζ 6-31G basis set[111,112] was used to save computational resources. For 1st row transition metal Fe, Wachters-Hay basis set with diffuse functions and polarization functions was applied, under the designation 6-311++G(d,p).[113,114] The crystal geometries of **A-D** determined by X-ray diffraction, were used as initial guesses in the optimizations. The unobserved CN-linkage isomers were generated by manually exchanging the positions of N and C. The initial structures of possible transition states were generated by relaxed scans with educated guesses. All the geometries were optimized to stationary points in vacuum and further verified by the existence of proper numbers of imaginary vibrational frequencies, i.e. zero for a minimal and one for a transition state. Thermal corrections from vibrational calculations, along with solvation corrections in acetonitrile by SMD model,[115] was added to calculate the Gibbs free energies in solution. Grimme's empirical dispersion GD3BJ[116,117] was only added to the evaluation of H-bond stabilization. The Intrinsic

Reaction Coordinate was tracked by following the normal mode related to the imaginary vibrational frequency of the transition state, given by normalized Hessian matrix. The Hessian matrix was updated every ten steps and the track stopped till a minimal was located on the electronic potential surface. The EPR parameters were calculated by ORCA[118] with the functional B3LYP.[108] The *g* tensors and *A* tensors were calculated based on the optimized geometries extracted from Gaussian. The *A* tensors include both the dipole part and the second order contribution part of spin-orbital coupling. These tensors were diagonalized to generate eigenvalues.

EPR Spectroscopy and Bulk Electrolysis

CW EPR spectrum were recorded using an X-Band Bruker 300E spectrometer equipped with an Oxford Instruments helium flow cryostat (Oxford Instr. ESR910) and an ITC 503 temperature controller. Measurement conditions: Microwave frequency: 9.643 GHz; Modulation amplitude: 0.3 mT; Microwave power: 0.04mW. Temperature: 10 K. Coulometric oxidation was performed in a glovebox at -35°C with an EG&G Potentiostat 273A, a Ag/$AgNO_3$ reference electrode in CH_3CN, a Pt-wire counter electrode, and a Pt-mesh working electrode. The solution was transferred to an EPR tube, removed from the glovebox, and immediately frozen in liquid N_2. A cyclic voltammogram was performed before and after the coulometric oxidation and gave similar features in both cases. The similarity of cyclic voltammograms of complex **D** performed before and after the coulometric oxidation indicated preservation of the structure in the **D**/**D**$^+$ conversion.

Synthesis of Compound A

A dark red solution of [Na][(μ-pdt)[$Fe_2(CO)_5CN$] was generated by the published procedure using 0.5 g (μ-pdt)[$Fe(CO)_3]_2$ (1.3 mmol) and 0.13 mL of a 1.0 M solution of sodium bis(trimethylsilyl)amide in 25 mL of THF. The resulting solution was transferred to a degassed round bottom flask containing 0.511 g of [(η-C^5H^5)$Fe(CO)_2$THF][BF_4] (1.3 mmol). The reaction was allowed to stir until complete conversion to the bridging cyanide product as determined by IR (~30 mins). The solvent was removed and the remaining solid was loaded onto a 30 cm silica gel column eluting first with hexanes to remove an orange band corresponding to (μ-pdt)[$Fe_2(CO)_6$] followed by a solvent gradient to pure diethyl ether to initially remove any [(η- C_5H_5)$Fe(CO)_2]_2$ generated during the reaction. Compound **A** finally elutes followed by solvent removal to produce 0.568 g of Compound **A** resulting in a 78% yield of an orange/brown solid. X-ray quality crystals were grown by slow diffusion of hexanes into a DCM solution of compound **A** at -30°C. IR (THF, cm^{-1}) ν(CO) 2069 (m), 2026 (m), 1986 (s), 1955 (s), 1930 (m); ν(CN) 2128 (m). Anal. Found (Calcd) for $Fe_3S_2NO_7C_{16}H_{11}$: C, 34.57 (34.26); H, 2.09 (1.98); N, 2.51 (2.50). ^1H NMR (400 MHz, CD_3OD): δ 1.5-2.4 (6H, br) 4.89 (5H, S).

Synthesis of Compound B

To a Schlenk flask containing 0.25 g (μ-pdt)[$Fe_2(CO)_6$] (0.64 mmol), 0.294 g (η-C_5H_5)Fe(dppe)CN (0.54 mmol), and 0.037 g Me_3NO (0.5 mmol) was added 30 mL of THF and stirred for 2 hours. The resulting dark brown solution was taken to dryness under reduced pressure, dissolved in 3 mL ether and filtered through a plug of Celite under an inert atmosphere. A dark green solid was precipitated with 40 mL hexanes followed by washing with hexanes until the supernatant was no longer orange. The solid was dried under vacuum yielding 0.336 g corresponding to a 69% yield. X-ray quality crystals were grown by slow evaporation of a 5:1 DCM:Hexanes solution at -30°C. IR (THF, cm^{-1}) ν(CO) 2035 (m), 2028 (m), 1980 (s), 1947 (m), 1919 (m); ν(CN) 2100 (w). Anal. Found (Calcd) for $Fe_3P_2S_2NO_5C_{40}H_{35}$: C, 52.96 (53.19); H, 1.56 (1.55); N, 3.94 (3.91). ^1H NMR (400 MHz, $CDCl_3$): δ 7.05-7.85 (20H, m) 4.16 (5H, s) 1.97-2.21 (4H, m) 1.25-1.8 (6H, m). ^{31}P NMR (400 MHz, CD_2Cl_2): δ 102.5-104.2 (CH_2**P**Ph, m).

Synthesis of Compound C

To a Schlenk flask containing 0.184 g (μ-pdt)$[Fe(CO)_3][Fe(NO)(IMe)(CO)][BF_4]$ (0.34 mmol) dissolved in 30 mL of DCM at 0°C was added 0.1 g (η- C_5H_5)$Fe(CO)_2CN$ (0.51 mmol) under back pressure of N_2. The solution was stirred for 30 mins and allowed to warm to room temperature followed by filtration through a plug of celite. The resulting solution was loaded onto a 30 cm silica gel column and eluted with 50% THF/DCM to elute a yellow band of (η- C_5H_5)$Fe(CO)_2CN$ followed by a red band of compound C. Removal of the solvent resulted in 0.166 g of a red solid in a 67% yield. X-ray quality crystals were grown by slow evaporation of a DCM solution at room temperature. IR (DCM, cm^{-1}) ν(CO) 2067 (m), 2060 (m), 2024 (s), 1995 (m); ν(CN) 2154 (w); ν(NO) 1755 (m). Anal. Found (Calcd) for $Fe_3S_2N_4O_6C_{19}H_{20}BF_4$: C, 32.04 (31.79); H, 2.75 (2.67); N, 7.55 (7.81). ESI-MS+ (CH_2Cl_2): m/z = 630.85 (μ-pdt) $[CpFe(CO)_2CN]$ [FeNO(IMe)] $[Fe(CO)_3]^+$. ^1H NMR (400 MHz, CD_2Cl_2): δ 7.17 (2H, s) 5.22 (5H, s) 3.78 (6H, s) 1.2-2.1 (6H, m).

Synthesis of Compound D

A Schlenk flask was loaded with 0.095 g solid (η-C_5H_5)Fe(dppe)CN (0.17 mmol) and 0.1 g (μ-pdt)(μ-H)[Fe(CO)$_2$PMe$_3$]$_2$[PF$_6$] (0.16 mmol) and purged with Ar for 15 mins followed by the addition of 30 mL of DCM. The flask was cooled to 0°C and illuminated with a 275 W GE ultraviolet Sunlamp for 6 h. Due to the heat produced by the sun lamp, care was taken to ensure the solution is kept at 0°C. The sunlamp was removed, the solution stirred at room temperature for 8 h and loaded onto a 30 cm column eluting with 5% THF in DCM. The dark green band was collected and the solvent removed to afford 0.107 g of compound **C** in a 58% yield. IR (DCM, cm^{-1}) ν(CO) 2020 (m), 1964 (m), 1949 (s); ν(CN) 2081 (w); Anal. Found (Calcd) for $Fe_3S_2P_5NO_3C_{44}F_6H_{54}\cdot OC_4H_{10}$ C, 47.46 (47.27); H, 5.19 (5.29); N, 1.22 (1.15). ESI-MS+ (CH_2Cl_2): m/z = 1000.11 (μ-pdt)(μ-H)[CpFe(dppe)CN][Fe(CO)PMe$_3$][Fe(CO)$_2$PMe$_3$]$^+$. ^{1}H NMR (400 MHz, CD_2Cl_2): δ -27.35 (1H, dd) -10.54 (1H, dd) 1.1-1.4 (18H, m) 1.5-2.9 (10H, m) 4.39 (5H, t) 6.9-8.0 (20H, m). ^{31}P NMR (400 MHz, $CDCl_3$): δ -145.0 (**P**F$_6$, sept) 21.5-28.0 (**P**Me$_3$, m) 101.0-103.0 (CH$_2$**P**Ph, m). X-ray quality crystals were grown by first conducting a counter ion exchange with NaBArF. Compound D (0.1 g or 0.087 mmol) and NaBArF (0.071 g or 0.08 mmol) were dissolved in 5 mL DCM in a schlenk flask and stirred overnight. The solvent was removed and the residue dissolved in 15 mL diethyl ether, filtered through a plug of Celite and the solvent removed to afford 0.143 g of compound. Crystals were grown by slow diffusion of hexanes into a solution of D in THF.

Cleavage Reactions Using Trimethylphosphine

To a 5 mL vial containing 0.05 mmol of the appropriate bridging cyanide compound and a stir bar was added 1 mL of a 0.05 mM solution of PMe_3 dissolved in THF. The resulting solution was stirred and monitored by IR spectroscopy until the reaction was judged to be complete by the disappearance of the bridging cyanide peak. Compound **D** showed no reaction with PMe_3 even at elevated temperatures or increased PMe_3 concentration.

Cleavage of Compound A

The reaction was judged to be complete after 6 h by the disappearance of the IR stretch at 2128 cm^{-1} corresponding to the bridging cyanide.

Cleavage of Compound B

The reaction was complete upon adding the PMe_3 evident by the immediate color change from green/brown to red.

Cleavage of Compound C

The reaction was complete after 30 minutes evident by the disappearance of the IR stretch at 2154 cm^{-1} corresponding to the bridging cyanide.

Cleavage Reactions Using Tetraethylammonium Cyanide

To a 5 mL vial containing 0.05 mmol of the appropriate bridging cyanide compound, 1 equiv. of $[NEt_4][CN]$, and a stir bar was added along with 3 mL of THF. The resulting solution was stirred and monitored by IR spectroscopy until the reaction was judged to be complete by the disappearance of the bridging cyanide peak. Compound **D** showed no reaction with $[NEt_4][CN]$ even at elevated temperatures or increased concentrations of $[NEt_4][CN]$.

Cleavage of Compound A

The reaction was judged to be complete after 4 h by the disappearance of the IR stretch at 2128 cm^{-1} corresponding to the bridging cyanide.

Cleavage of Compound B

The reaction was complete upon adding the $[NEt_4][CN]$ evident by the immediate color change from green/brown to red.

Cleavage of Compound C

The reaction was judged to be complete after 45 mins by the disappearance of the IR stretch at 2154 cm^{-1} corresponding to the bridging cyanide.

Experimental Details for Chapter IV

Physical Measurements.

The boron-containing product was identified by ^{11}B NMR spectroscopy, recorded on a Varian Unity Inova 400 FT NMR at 128.19 MHz and 21.0 °C referenced to $BF_3{\cdot}OEt_2 = 0$ ppm. When evolution of H_2 ceased, a 0.35 mL sample of the reaction solution was withdrawn and injected into an NMR tube and the solvent level adjusted to 5 cm with d_8-THF. Gas identification was accomplished with an Agilent Trace 1300 GC equipped with a thermal conductivity detector and a custom made 120 cm stainless steel column packed with Carbosieve-II from Sigma-Aldrich. The carrier gas was Ar and throughout the entire separation the column was kept at 200 °C, while the detector was at 250 °C. Identification of gases from the reactions was accomplished by withdrawing 400 µL of the headspace using a 0.5 mL Valco® Precision Sampling Syringe, Series A-2 equipped with a Valco® Precision Sampling syringe needle with a 5 point side port. Gas identification was accomplished by comparing to a reference GC trace of a sample consisting of 0.1 mL H_2, 0.1 mL of gas from the atmosphere (N_2/O_2), and 1 mL CH_4. H_2 is the first peak to elute from the column at 1.28 min., followed by N_2/O_2 at 2.52 min., and finally CH_4 at 4.09 min.

All infrared spectra in the kinetic study were recorded using a Bruker Vertex 80 FTIR spectrometer equipped with both step-scan and rapid-scan capabilities. A temperature controlled, 0.5 mm path length IR transmission cell (Harrick Scientific) with CaF_2 windows was used to acquire the spectra. The cell temperature was controlled with the use of a circulating water bath (± 0.1 °C). Photolysis of the solution was achieved using a Quantel Brilliant B Nd:YAG laser operating at 355 nm (70 mJ/pulse) with a 7 ns pulse width.

Kinetic Studies

An appropriate amount of the diiron complex was dissolved in methylcyclohexane solvent to yield a 2-4 mM solution that was purged with N_2. The required amounts of triethylamine borane ($B{:}A^t$) and triethylphosphite ($P(OEt)_3$) were added to this solution using a gas tight syringe. For each experiment, the concentration of borane was kept constant (1.35 M) and the amount of $P(OEt)_3$ was varied between 0.05 and 0.60 M. The resulting solution was transferred to the IR cell using a syringe pump and care was taken to minimize exposure of the photolysis solution to ambient light by covering the delivery syringe and flask in aluminum foil. After injection into the cell, the sample was allowed to thermally equilibrate for a few minutes before the experiment was initiated.

All experiments were conducted under pseudo first-order conditions with the concentration of the $P(OEt)_3$ ligand at least 10 times greater than that of the reactant metal complex. Observed rate constants (k_{obs}) were obtained from single exponential fits to the temporal profile of either reactant or product complexes. The stated errors in the rate constants and activation parameters were obtained from a least squares fit to the data as reported by the data analysis program Kaleidagraph.

Computational Studies

DFT calculations were performed using the development version of the Gaussian suite of programs.[107] All geometries were fully optimized using the ωB97XD functional and the all-electron, triple-ζ basis set def2-TZVPP.[119] Reported geometries were assigned to minima or transition states according to their number of imaginary frequencies. Numerical accuracy was ensured by using a large integration grid with 99 radial shells of 590 points (‘ultrafine’). Gibbs energies and enthalpies were calculated at 298 K and 1 atm with fully optimized geometries. Vibrational frequencies were scaled by a linear fitting of the frequencies of compound 5-CO with experimental values. This methodology was chosen based upon the performance of our previous calculations of diiron complexes of this type.[120]

Hydrogen Release Studies

In all cases solutions of the diiron catalyst and amine-borane were prepared in an Ar filled glovebox, placed in 2 mL and 10 mL volumetric flasks, respectively, capped with a rubber septa, parafilmed, copper wired, removed from the glovebox, and filled to the appropriate level with anhydrous THF. A degassed 5 mL Pyrex glass vial with a small stir bar and rubber septum was loaded with 2 mL of the amine-borane solution as well as 0.5 mL of the diiron solution corresponding to a 10 mol% loading of diiron catalyst. Prior to commencing the photolysis reaction, the vial was connected via PTFE tubing to a 50 mL burette filled with water connected to a variable height funnel. The pressure was equilibrated before irradiation by a Hg-arc lamp from ORIEL Instruments operating at 200W with a spectral window from 250 to 2500 nm. Following a short induction period, bubbles of a released gas were seen to displace water in the burette. Volume measurements were taken every 5 min until further changes ceased. A 200 µL sample of the headspace was analyzed by gas chromatography. Detection of H_2 was confirmed by comparison to standards composed of mixtures of H_2, CH_4, N_2 and O_2.

Control experiments were run in the same manner as the gas collection experiments except the reaction flask was not connected to the gas collection apparatus. To confirm the necessity of the diiron catalyst, $B{:}A^s$ was dissolved in THF and irradiated for 2 hours and the headspace analyzed via gas chromatography. No peak for H_2 was detected. To confirm the need for light the vial consisting of the diiron catalyst and $B{:}A^s$ was wrapped in aluminum foil and placed in the dark for 2 h before adding THF and stirring the reaction for 2 h. Analysis of the headspace gas showed no H_2 production. Irradiating the diiron catalyst in THF lacking $B{:}A^s$ for 2 h shows some CO but no H_2 release. Finally, to confirm the necessity for a hydrogen atom on both the nitrogen and boron, $B{:}A^t$ was used in place of $B{:}A^s$ from which no H_2 was detected. In all control experiments, after 2 h of irradiation 400 µL of the headspace was withdrawn followed by injecting 200 µL into the GC. No peak corresponding to H_2 could be detected.

Experimental Details for Chapter V

Bulk electrolysis experiments were carried out in a custom made three-neck truncated conical shaped flask with a gas inlet/outlet port. The necks were equipped with a 3 mm glassy carbon working electrode, a Ag/$AgNO_3$ reference electrode, and a Ni-Cr-coiled wire counter electrode. The reference electrode consisted of a glass tube containing a Ag wire dipped in a 1 mM solution of $AgNO_3$ in MeCN separated from the bulk solution by a Vycor frit. The counter electrode consisted of a glass tube containing a Ni-Cr-coiled wire and 0.1 M [n-Bu_4N][PF_6] in MeCN separated from the bulk solution via a medium glass frit. The electrochemical cell was loaded with 10 mL of 0.1 M [n-Bu_4N][PF_6] in MeCN and purged with Ar until the peak for O_2 was no longer present in the cyclic voltamogram. The appropriate catalyst (2×10^{-5} mole, ~10.5 mg) as well as 50 equivalents of trifluoroacetic acid was added to the cell. A cyclic voltammogram was recorded to ensure that the experiment was under catalytic conditions. Bulk electrolysis was performed at -1.56 V vs. Fc/Fc^+ for 30 minutes followed by injection of 1 mL CH_4 as an internal standard.

Gas identification was accomplished with an Agilent Trace 1300 GC equipped with a thermal conductivity detector and a custom-made 120 cm stainless steel column packed with Carbosieve-II from Sigma-Aldrich. The carrier gas was Ar, and throughout the entire separation, the column was kept at 200 °C, while the detector was at 250 °C. Identification and quantification of H_2 produced from bulk electrolysis was accomplished by withdrawing 200 μL of the headspace using a 0.5 mL Valco Precision Sampling Syringe, Series A-2 equipped with a Valco Precision Sampling syringe needle with a 5 point side port. Gas identification was accomplished by comparing to a reference GC trace of a sample consisting of 0.1 mL H_2, 0.1 mL of gas from the atmosphere (N_2/O_2), and 1 mL CH_4. H_2 is the first peak to elute from the column at 1.28 min., followed by N_2/O_2 at 2.52 min., and finally CH_4 at 4.09 min.

Quantification of H_2 produced was accomplished by determining the relative response factor of H_2 and the internal standard, CH_4. This was done by preparing vials containing varying amounts of H_2 with one mL of CH_4 and plotting the $\frac{\text{area of } H_2}{\text{area of } CH_4}$ vs. $\frac{\text{mL of } H_2}{\text{mL of } CH_4}$, as described in text.

Experimental Details for Chapter VI

Synthesis of [Ni-Re]

To a schlenk flask containing 0.277 g of Ni(bme-Dach) (1.0 mmol) and 0.361 g of $Re(CO)_5Cl$ (1.0 mmol) was added 50 mL of MeOH. The flask was wrapped in aluminum foil, connected to a gas bubbler, and heated at 60°C for 12 hours. The resulting red/orange solution (containing some suspended product) was cooled and diluted with 150 mL of diethyl ether to precipitate the remaining coral colored solid. Precipitated solid was collected and dried under vacuum to afford 0.495 g of **[Ni-Re]** corresponding to an 85% yield. X-ray quality crystals were grown by slow diffusion of diethyl ether into a concentrated DMF solution of **[Ni-Re]** at 22°C. IR (DMF, cm^{-1}) ν(CO) 2010, 1897, 1883. Anal. found (calcd) for $ReNiClS_2N_2O_3C_{12}H_{18}$: C, 24.97 (24.73); H, 3.09 (3.11); N, 4.97 (4.81).

Synthesis of [Co-Re]

To a schlenk flask containing 0.307 g of Co(NO)(bme-Dach) (1.0 mmol) and 0.361 g of $Re(CO)_5Cl$ (1.0 mmol) was added 75 mL of dichloromethane. The flask was wrapped in aluminum foil, connected to a gas bubbler, and heated at reflux for 12 hours. Solvent was removed via vacuum and the resulting brown/green solid was chromatographed on a 12 cm. x 1.5 cm. silica gel column eluting with 10% MeOH in THF. A purple band of Co(NO)(bme-Dach) eluted first followed by **[Co-Re]** as a dark green band which was collected and the solvent removed via vacuum. The resulting dark green solid weighed 0.374 g corresponding to a 61% yield. X-ray quality crystals were grown by cooling a saturated MeCN solution of **[Co-Re]** to -30°C overnight. IR (THF, cm^{-1}) ν(CO) 2015, 1907, 1893. Anal. found (calcd) for $ReCoClS_2N_3O_4C_{12}H_{18}$: C, 23.71 (23.51); H, 3.18 (2.96); N, 6.62 (6.85).

Synthesis of [Fe-Re]

To a schlenk flask containing 0.304 g of Fe(NO)(bme-Dach) (1.0 mmol) and 0.361 g of $Re(CO)_5Cl$ (1.0 mmol) was added 75 mL of dichloromethane. The flask was wrapped in aluminum foil, connected to a gas bubbler, and heated at reflux for 12 hours. Solvent was removed via vacuum and the resulting brown/green solid was chromatographed on a 12 cm. x 1.5 cm. silica gel column eluting with 10% MeOH in THF. A green band of Fe(NO)(bme-Dach) eluted first followed by **[Fe-Re]** as a green/brown band which was collected and the solvent removed via vacuum. The resulting green/brown solid weighed 0.35 g corresponding to a 57% yield. X-ray quality crystals were grown by cooling a saturated MeCN solution of **[Fe-Re]** to -30°C overnight. IR (THF, cm^{-1}) ν(CO) 2016, 1909, 1892. Anal. found (calcd) for $ReFeClS_2N_3O_4C_{12}H_{18}$: C, 23.73 (23.63); H, 3.01 (2.97); N, 6.89 (6.89).

Synthesis of [Ni-Mn]

To a schlenk flask containing 0.277 g of Ni(bme-Dach) (1.0 mmol) and 0.274 g of $Mn(CO)_5Br$ (1.0 mmol) was added 50 mL of MeOH. The flask was wrapped in aluminum foil, connected to a gas bubbler, and heated at 60^{o}C for 12 hours. The resulting orange solution (containing some suspended orange product) was cooled and diluted with 150 mL of diethyl ether to precipitate the remaining orange solid. Precipitated solid was collected and dried under vacuum to afford 0.495 g of **[Ni-Mn]** corresponding to an 89% yield. X-ray quality crystals were grown by slow diffusion of diethyl ether into a concentrated DMF solution of **[Ni-Mn]** at 22^{o}C. IR (DMF, cm^{-1}) ν(CO) 2008, 1917, 1897. Anal. found (calcd) for $MnNiBrS_2N_2O_3C_{12}H_{18}$: C, 29.76 (29.06); H, 3.74 (3.66); N, 5.84 (5.65).

Synthesis of [Co-Mn]

To a schlenk flask containing 0.307 g of Co(NO)(bme-Dach) (1.0 mmol) and 0.274 g of $Mn(CO)_5Br$ (1.0 mmol) was added 75 mL of dichloromethane. The flask was wrapped in aluminum foil, connected to a gas bubbler, and heated at reflux for 12 hours. Solvent was removed via vacuum and the resulting brown/green solid was chromatographed on a 12 cm. x 1.5 cm. silica gel column eluting with 10% MeOH in THF. A purple band of Co(NO)(bme-Dach) eluted first followed by **[Co-Mn]** as a dark green band which was collected and the solvent removed via vacuum. The resulting dark green solid weighed 0.408 g corresponding to a 78% yield. X-ray quality crystals were grown by cooling a saturated MeCN solution of **[Co-Mn]** to -30^{o}C overnight. IR (THF, cm^{-1}) ν(CO) 2020, 1927, 1908. Anal. found (calcd) for $MnCoBrS_2N_3O_4C_{12}H_{18}$: C, 27.92 (27.39); H, 3.25 (3.45); N, 7.62 (7.99).

Synthesis of [Fe-Mn]

To a schlenk flask containing 0.304 g of Fe(NO)(bme-Dach) (1.0 mmol) and 0.274 g of $Mn(CO)_5Br$ (1.0 mmol) was added 75 mL of dichloromethane. The flask was wrapped in aluminum foil, connected to a gas bubbler, and heated at reflux for 12 hours. Solvent was removed via vacuum and the resulting brown/green solid was chromatographed on a 12 cm. x 1.5 cm. silica gel column eluting with 10% MeOH in THF. A green band of Fe(NO)(bme-Dach) eluted first followed by **[Fe-Mn]** as a green/brown band which was collected and the solvent removed via vacuum. The resulting green/brown solid weighed 0.356 g corresponding to a 68% yield. X-ray quality crystals were grown by cooling a saturated MeCN solution of **[Fe-Mn]** to -30^{o}C overnight. IR (THF, cm^{-1}) ν(CO) 2019, 1930, 1912. Anal. found (calcd) for $MnFeBrS_2N_3O_4C_{12}H_{18}$: C, 27.12 (27.55); H, 3.31 (3.47); N, 7.80 (8.03).

CHAPTER III

CYANIDE-BRIDGED IRON COMPLEXES AS BIOMIMETICS OF TRI-IRON ARRANGEMENTS IN MATURASES OF THE H-CLUSTER OF THE DI-IRON HYDROGENASE[*]

Introduction

The recent demonstration of the possibility of loading the apo-HydA (the [FeFe]-H_2ase enzyme *sans* the 2Fe subsite) and apo-HydF (a precursor protein in the maturation process) with synthetic analogues of the active site is convincing that the *small molecular models are indeed representative of the essential catalyst*.[28,29,35,63] Such "simple methodology of controlled metalloenzyme activation" as described by Berggren, et al.[28] and Esselborn, et al.,[63] provided unambiguous evidence that the bridgehead atom X of the S to S linker, μ-SCH_2XCH_2S, in the 2Fe-subsite is NH. The need for such a pendant base adjacent to the open site on Fe was already proposed from a theory-generated mechanism of heterolytic hydrogen production or cleavage, and corroborated by spectroscopy.[25,26,50,121,122]

---

[*] Reprinted with permission from Lunsford, A. M.; Beto, C. C.; Ding, S.; Erdem, Ö. F.; Wang, N.; Bhuvanesh, N.; Hall, M. B.; Darensbourg M. Y. *Chem. Sci.*, **2016**, ***7***, 3710. Copyright **2016** The Royal Society of Chemistry. [123]
The computational results and their description presented in this chapter were performed by Shengda Ding.

The interrogation by pulsed EPR spectroscopy of the HydF maturase protein containing the 2Fe subsite derived from the synthetic analogue yielded an unexpected conclusion.[28] As shown in Figure I-7, a linear cyanide bridges the [4Fe-4S] cluster to the 2Fe subsite; HYSCORE data found the unpaired electron of the [4Fe-4S] cluster to be strongly coupled to the C-13 nucleus of cyanide derived from the 2Fe unit prepared with labeled $^{13}CN^{-}$. The molecular interpretation of this observation is that the cyanide that serves to couple the 2Fe unit to the apo-HydF carrier protein has flipped from its origin, placing the cyanide nitrogen next to the 2Fe site. As the 2Fe unit is transferred to the apo-HydA another flip occurs, returning the CN^{-} to the C-bound terminal position. While examples of μ-CN^{-} linkage isomers between two transition metals are found in inorganic and organometallic chemistry, such maneuvers as CN linkage isomerism, i.e. CN flipping, subsequent to adduct formation are not common.[124-126] Hence we have endeavored to prepare cyanide-bridged constructs of 3Fe systems with features related to the organoiron moiety within the loaded HydF protein. Further significance of such synthetic studies relates to the biosynthesis of the $Fe(CO)_2CN$ moiety itself, as fundamental background for cyanide interactions in iron-rich proteins.

Synthesis and Characterization

Synthetic efforts were guided by reports from Zhu and Vahrenkamp of the synthesis of several organometallic complexes of the type M-CN-M’/M-NC-M’ using a labile ligand approach and judicious balance of the electropositive character of M and M’.[127] The precursors chosen for diiron complexes, complexes **1** - **4** in Figure III-1, are noted to replicate certain features of the [FeFe]-H_2ase enzyme active site; the cyclopentadienyl iron derivatives, **x**, **y**, and **z**, are well known Fe(II) complexes, meant to mimic a ferrous iron in the [4Fe-4S] cluster of HydF. With these precursors, the four cyanide-bridged, 3Fe complexes displayed in Figure III-2 were prepared, isolated in crystalline form and characterized by X-ray diffraction. Note that the Fe—Fe distances in the diiron moiety are similar in all, however, the extent to which there is an Fe—Fe bond undoubtedly differs. For example, Complex **D** is not expected to have the possibility of a formal bond due to the existence of the (semi-) bridging hydride.

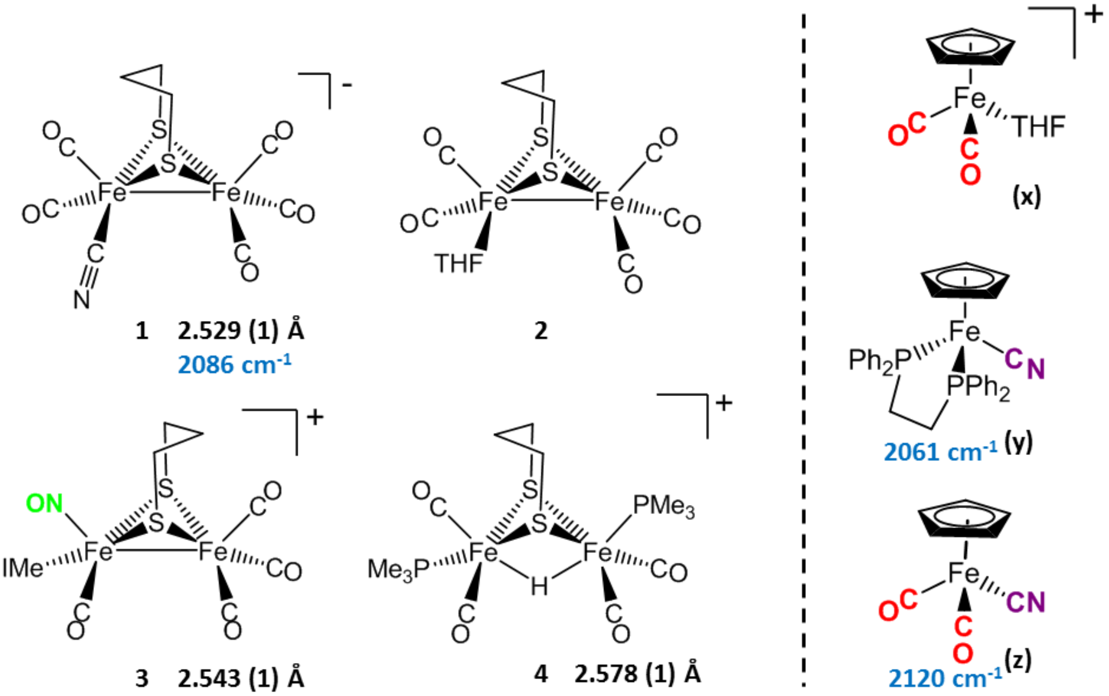

Figure III-1. [FeFe] and [Fe] precursors to µ-CN 3Fe complexes; Fe—Fe distances (Å) and ν(CN) values, cm^{-1} listed where appropriate.

Complex **A** was prepared from the eminent precursor for scores of [FeFe]-H_2ase mimetics, (μ-pdt)$[Fe(CO)_3]_2$, here with one CO ligand substituted by CN^-, namely complex **1**.[71] When **1** is exposed to the labile ligand-containing complex **x**, (η^5-C_5H_5)$Fe(CO)_2(THF)^+$, derived from halide abstraction of (η^5-C_5H_5)$Fe(CO)_2Br$ in THF solvent, conversion to the cyanide-bridged product **A** was completed within minutes. The isolated neutral complex **A** is bench-top stable, even submitting to column chromatography on silica without protection from air.

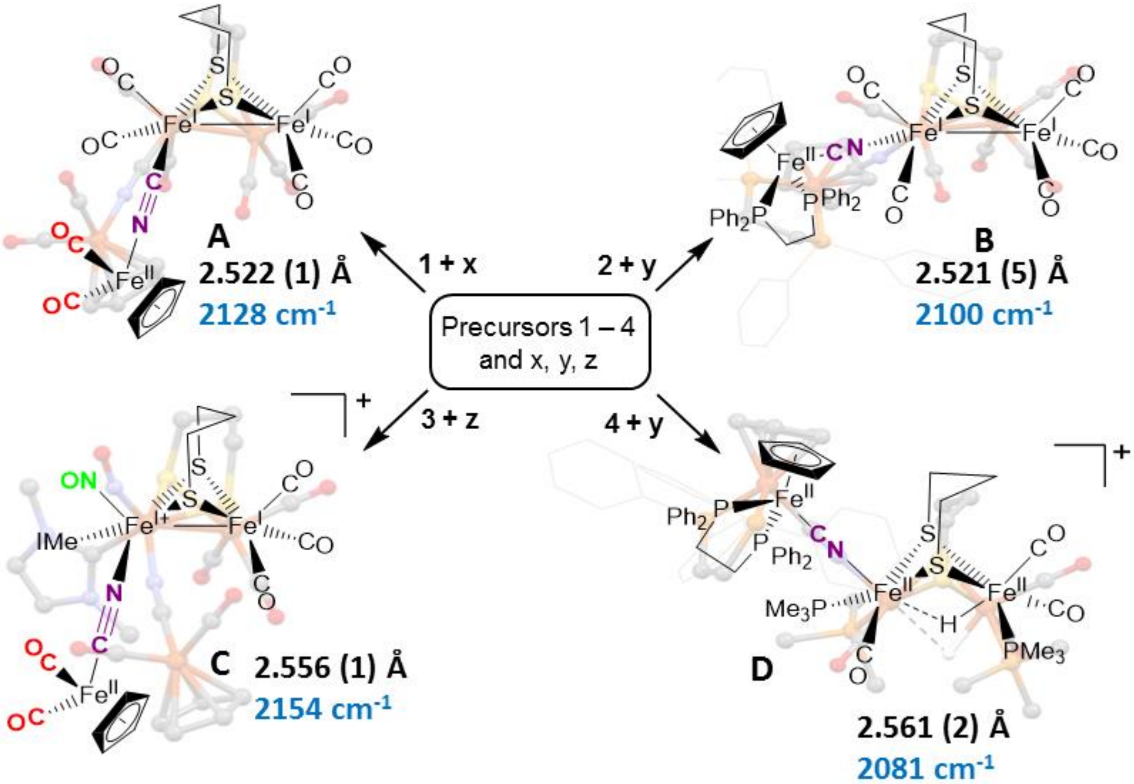

Figure III-2. Combinations of [FeFe] and [Fe] precursors (from Figure III-1) and products. Structures from XRD analysis are shown in relief. Fe-Fe distances (Å) and ν(CN) values, cm^{-1}, are listed with each structure.

From purified product, X-ray quality crystals were obtained and the corresponding diffraction data was refined as noted. With the cyanide C-bound to the diiron precursor and N-bound to the mono-Fe^{II}, an R_f of 3.17 was obtained. The opposite assignment led to elongated N ellipsoids and an R_f of 3.43. Such assignments of linkage isomers based on XRD refinements of both possibilities, M-CN-M' or M-NC-M' arrangements, are typical for the 22 organometallic complexes in the Vahrenkamp study, and commonly used in other cases.[124-127] This approach is the basis for all CN linker assignments in our study as well.

As noted in Figure III-1 and Figure III-2, there is a *ca*. 40 cm^{-1} shift to higher values of the ν(CN) in the product **A** in contrast to the precursor **1**, ascribed to the kinematic effect operative in bridging cyanides.[128,129] There is also a gain of intensity in the ν(CN) over the precursor consistent with the increased delocalization of π electron density in the Fe^{I}-CN-Fe^{II} product. Minor positive shifts in ν(CO) values of carbonyls on the diiron moiety are indicative of a drain of the electron density on the diiron unit via the interaction of the cyanide with the Fe(II); consistently, the ν(CO) values of the $(\eta^5\text{-}C_5H_5)Fe(CO)_2$ appendage shift negatively. The diatomic ligand spectral changes resulting from the Lewis acid/base interaction of $[Fe^{I}Fe^{I}]CN^{-}$, and the enhanced stability of **A** over **1,** are consistent with the properties of cyanide adducts of $(\mu\text{-pdt})[Fe(CO)_2CN]_2^{2-}$ with BAr^{F}_3.[130-132]

Attempts to prepare the linkage isomer of **A** by the addition of the $(\eta^5\text{-}C_5H_5)Fe(CO)_2CN$ complex (**z**) to the labile solvent bound diiron derivative **2** were unsuccessful. However, with increased basicity of the cyanide on precursor **y**, the (η^5-

C_5H_5)Fe(dppe)CN complex reacted with **2** generating **B,** whose characterization by spectroscopies and XRD indicated the $Fe^{I}Fe^{I}$-NC-Fe^{II} arrangement shown in Figure III-2. Specifically, the IR spectrum in the diatomic region found the ν(CN) value again shifted positively by 40 cm^{-1} as compared to **y**; and the pattern complexity and slightly negative shifts of the ν(CO) indicated the effect of the electron donating cyanometallate ligand on the diiron moiety. In contrast to **A**, complex **B** is much less stable to air and moisture.

An alternate strategy for obtaining the Fe^{II}-CN-[FeFe] species is to enhance the electrophilicity of the diiron unit. This we have done by two methods: Complex **C** exploits the electrophilic properties of an unusual diiron complex that has carbonyls on a single iron substituted by an N-heterocyclic carbene (NHC) and NO^{+}.[77] This asymmetric substitution pattern on the precursor **3** has the effect of producing a "hot iron", on which the electrophilicity of the nitrosonium ligand overwhelms the good electron-donating character of the NHC ligand. Subsequent addition of ligands of disparate donor properties (from ^{13}CO to metallodithiolates of the MN_2S_2 class) results in replacing the remaining CO on that iron, which is of substantial Fe^{II} character.[77] Thus, the mono-iron precursor (**z**) readily reacts with **3** producing complex **C**.

The fourth member of the triiron series was generated by photolysis of **4**, (μ-pdt)(μ-H)$[Fe(CO)_2PMe_3]_2^{+}$ as its PF_6^{-} salt, in the presence of **y**.[97] As the oxidation state of irons in the diiron precursor **4** is formally +2, the precursor **z,** even without the dppe donor ligand, would likely have given a similar success. However, the photolysis route to CO loss in **4** also degrades CO-containing **z**, hence the photolysis-tolerant **y** was the better choice for the mono-iron precursor. Color changes (red-orange to dark green-brown) indicated reaction progress of **4 + y**, and the ν(CN) value of **y**, 2061 cm^{-1}, shifts to 2081 cm^{-1} in complex **D**.

As indicated in Figure III-2, the μ-H of **D** is judged to be asymmetric (from the electron density maximum determined by crystallography, *vide infra*) and more tightly bound to the less substituted Fe^{II}. Consistently, the hydride region of the ^{1}H NMR spectrum shows a doublet of doublets due to the coupling with the non-equivalent P-31 nuclei.

Electrochemistry and EPR Spectroscopy

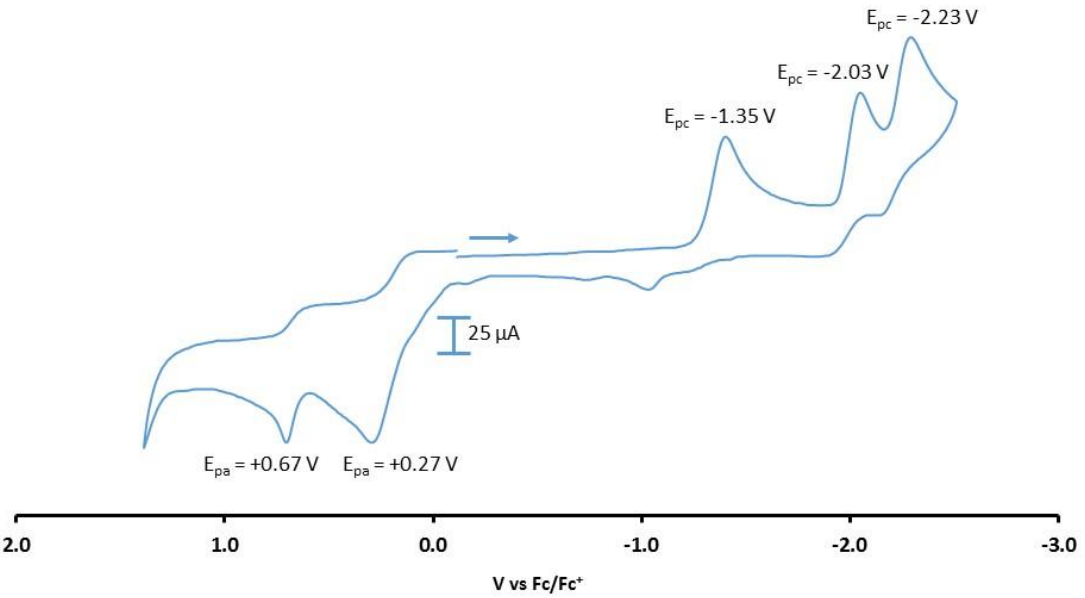

Figure III-3. Cyclic voltammograms of 2 mM Complex **A** at a scan rate of 200 mV/s in MeCN, referenced to internal Fc/Fc$^+$ = 0 V.

Complex **A** in CH_3CN exhibits three irreversible reduction events and two irreversible oxidation events within the range of +1.2 to -2.5 V, see Figure III-3. Another oxidation at 0.1 V results from degradation subsequent to reduction, even at the mildest -1.35 V potential. Assignment of the redox events relies on earlier definitive electrochemical studies of $CpFe(CO)_2X$ species.[133] Upon reduction, X^- is typically released and the resultant $CpFe(CO)_2$• radical couples, yielding the $[CpFe(CO)_2]_2$ dimer, whose one electron reduction is at -2.03 V. Whether the most negative response at -2.23 V is from the adduct **A** or from the precursor to **A**, the monocyanide (**x**), is uncertain. The CV's of adducts **B** and **C** can similarly be described, however, assignments are uncertain and redox-induced degradation is likely. Adduct **D** displays a reversible oxidation at 0.27 V that is more distinct when initially scanned in the positive direction and is assigned to the iron of the CpFe unit; the two irreversible reductive events are assigned to the diiron unit.

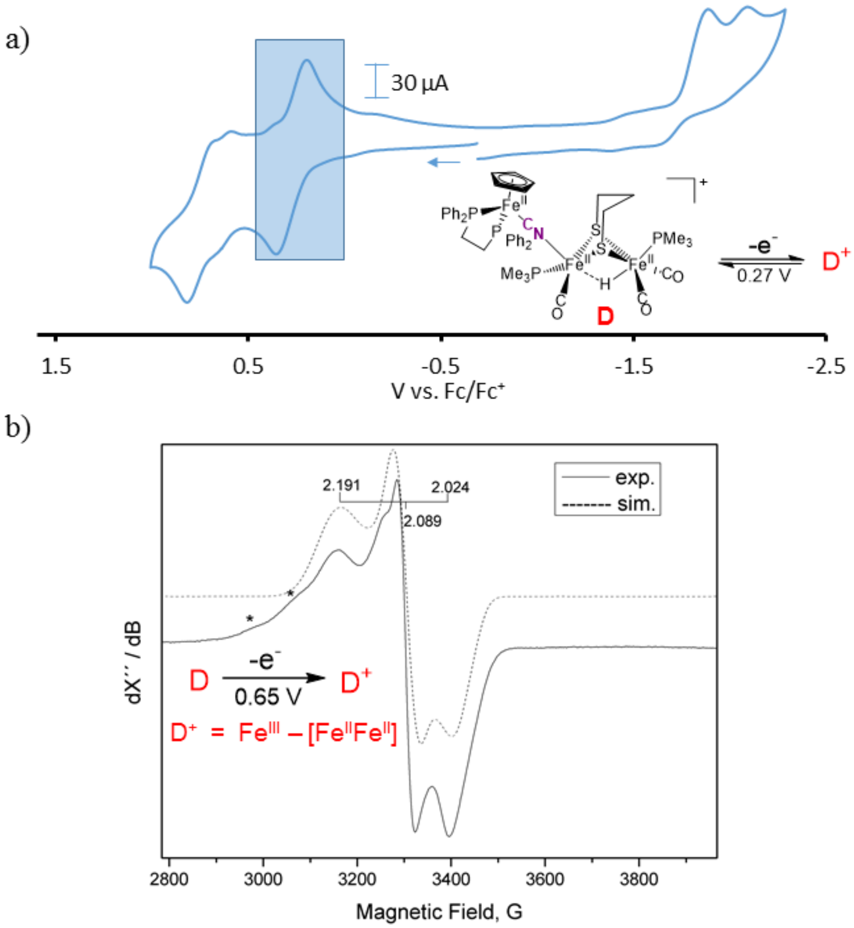

Figure III-4. a) Cyclic voltammogram of compound **D** in DCM at 200 mV/s referenced to $Fc^0/Fc^+ = 0$ V. The shaded region represents the oxidation event of the CpFe(dppe) unit at $E_{1/2} = 0.27$ V. b) Coulometric oxidation at 0.65 V generates a stable radical species with the representative X-band EPR spectrum shown. (*) denotes possible decomposition products.

Adduct **D** is the most stable of the four bridging cyanide complexes and its reversible oxidation suggests the possibility of generating an intact triiron radical observable by EPR spectroscopy. Coulometric oxidation of **D** at 0.65 V yielded an EPR-active species presumed to be **D**$^+$. Its X-band EPR spectrum at 10 K displays as a rhombic g-tensor, consistent with a low spin Fe^{III} center, with g (1, 2, 3) = (2.191, 2.089, 2.024).

Additional minor signals at g = 2.254 and 2.312, are presumed to be decomposition products in the sample which are marked by asterisks in Figure III-4.

Computations (DFT) found the majority of the unpaired spin to be on the iron of the mono-iron moiety, the CpFe(dppe) unit; anisotropic hyperfine coupling constants of A_{iso} = -98.65 and A_{iso} = -97.11 MHz for the two adjacent phosphorus atoms were similar to the qualitative spectral simulation (with Easyspin[134]) of A_{iso} $(^{31}P)_1$ = -85 and A_{iso} $(^{31}P)_2$ = -77 MHz. The spin density contour plot from DFT calculations showed 1.163 e^- on the mono-iron, of Fe^{III} character, while minor excess spins are on the two other irons, bridging cyanide and cyclopentadienyl unit. A hyperfine coupling pattern due to the ^{14}N of the cyanide could not be observed in the EPR spectrum indicating a small coupling constant. From ^{14}N HYSCORE data obtained at 343.8 mT (corresponding to g_2 = 2.089), this weak coupling to the nitrogen was found to be A_{iso} = 3 MHz, Figure III-5. DFT calculations showed that if the nitrogen atom of the cyanide is two atoms away from the spin center, as expected for **D** and **D**$^+$, the calculated isotropic coupling constant is 1.4 MHz. If the cyanide nitrogen was bound directly to the spin center the isotropic coupling of the nitrogen atom would increase to 9.5 MHz. This evidence suggests that the orientation of the cyanide in **D**$^+$ is the same as shown in Figure III-2 for its neutral **D** precursor.

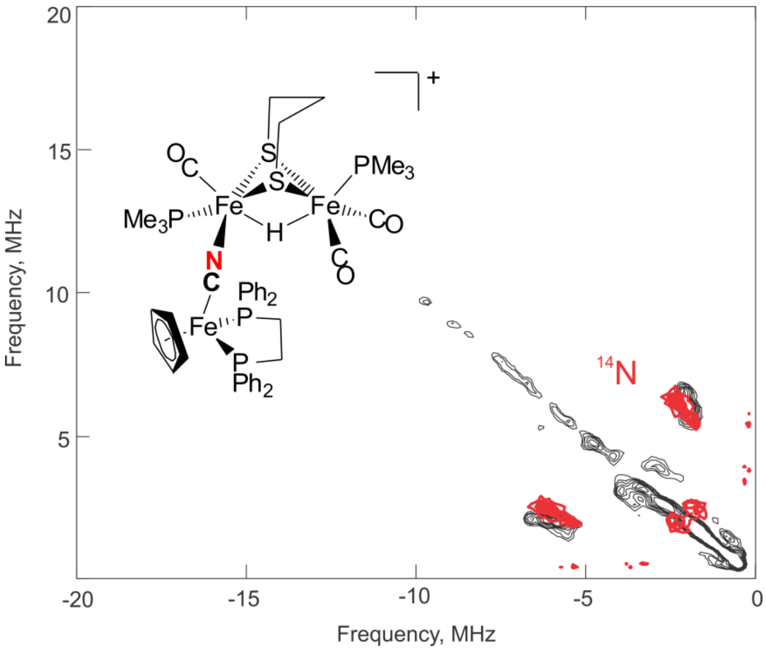

Figure III-5. X-band HYSCORE spectrum of electrochemically oxidized (at 0.65 V) Complex **D**$^+$, in DCM at 10 K. Simulation (in red) parameters (with Easyspin): g (1, 2, 3) = (2.191, 2.089, 2.024); ^{14}N HFC, A_{iso} = 3 MHz, K = 0.5; eta = 0.1; tau = 200 ns: Field position = 343.8 mT (corresponding to g_2); Microwave frequency = 9.78651 GHz.

Computational Protocols

Density functional theory computations were applied to evaluate the energetics of the possible linkage isomerization during the formation of M-CN-M' bridges from precursors M-CN and M'. Crystal structures of complexes **A-D** were imported as the initial geometries of the experimentally observed isomers. Computational IR frequencies matched with experimental values supporting the validity of the computational methodology. The initial geometries of their cyanide-flipped isomers were created by computationally exchanging the positions of C and N in the crystallographic structures. Geometric optimizations were done with Gaussian 09, as well as thermal and solvation corrections. Transition states were initially generated through relaxed scans with educated guesses and successively optimized. The Intrinsic Reaction Coordinate (IRC) calculations were applied to certain transition states, to trace the reaction paths following the imaginary vibrational frequency, until a local minimum on the potential energy surface was achieved. A detailed methodology description and the coordinates of optimized structures are provided in the experimental section of Chapter II; calculated metric data compares with experimental values with an approximately 1-2% error, lending confidence to the validity of the computations.

Despite the fact that the orientation of cyanide in these synthesized complexes is predetermined by the precursors, the calculations showed that it is always energetically advantageous for the carbon to coordinate to the mono-iron moiety in the four complexes. The Gibbs free energy differences between two isomers of complexes **A-D** were determined to be 1.0, 2.0, 3.2 and 4.4 kcal/mol, respectively.

Complex **A**, the simplest structure, was investigated as a representative example to search for a cyanide-flipping mechanism. The C-Fe and N-Fe bond energies of the linkage isomers were calculated (Figure III-6a) finding that the carbon, rather than nitrogen, end of CN forms the stronger bond to either Fe^{II} or $Fe^{I}Fe^{I}$, see **A’** and **A** of Figure III-6a. The imaginary vibrational frequency of **A-TS**, located as the likely transition state connecting the isomers (see Figure III-7a), is associated with a wagging motion that initiates the asymmetric concomitant slide from one CN end to the other. The motion is indicative of an intramolecular transfer mechanism rather than a dissociation-association mechanism. The Gibbs free energy of **A-TS** was calculated to be 38.7 kcal/mol above the more stable isomer **A’**, a barrier unlikely to overcome at room temperature, and thus consistent with the experimental observation of only one isomer.

While many features of the enzyme active site are mimicked in our model complexes, an obvious difference is the lack of an aza-dithiolate linker connecting the two iron atoms. Erdem, et al., have shown that when the central atom of this linker is NH, it may be electronically influenced by the ligands attached to the iron.[135] Presumably, the reverse would be true, i.e., changing the atom from NH to CH_2 may be expected to alter the electronics of the Fe-CN unit to some extent, and consequently the energy of cyanide isomerization. However, the replacement of the dithiolate linker in **A**, **A'** and **A-TS** by azadithiolate (adt, $-SCH_2NHCH_2S-$), i.e., having the N bridgehead as in [FeFe]-hydrogenase, does not significantly change the DFT computed energetics. The **adt-A’** with an Fe-CN-FeFe sequence is still more stable, by 1.2 kcal/mol, than **adt-A** with an Fe-NC-FeFe sequence. The corresponding transition state **adt-A-TS**, is 38.6 kcal/mol less stable than **adt-A’** similar to the 38.7 kcal/mol for the pdt analogue.

The reaction trajectory involving **A-TS** was obtained by intrinsic reaction coordinate (IRC) calculations and is presented in Figure III-7. The reaction coordinate is explained in the following sentences, taking the path from **A-TS** to **A’** as an example. **A-TS** follows the wagging imaginary vibrational motion first until the FeFe moiety approaches the nitrogen (Pts #5-15). In this manner, the FeFe moiety gradually shifts from C to N and ultimately the N-C-Fe angle continues to increase until it is completely linear (Pt #28). After that, the bridging cyanide continues to rotate to align the C-N-FeFe angle and the N-C-Fe re-bends slightly as a side effect until it reaches Pt #50. Finally both N-

C-Fe and C-N-FeFe angles adjust to completely linear as the energy ultimately drops to the local minimum **A’**. As the reaction coordinate is traced downhill, the C-N-FeFe angle increases monotonically. The other branch of the reaction coordinate, i.e. from **TS-A** to **A**, has exactly the same features and the validity of the transition state is confirmed. Such a route is partially related to the mechanism developed for HCN ⇆ CNH isomerization with spectroscopic evidence of the transition state.[136] A similar transition state **D-TS** for complex **D**, which features more bulky substituents on both iron moieties, was estimated to have an even higher barrier of 51.0 kcal/mol**.**

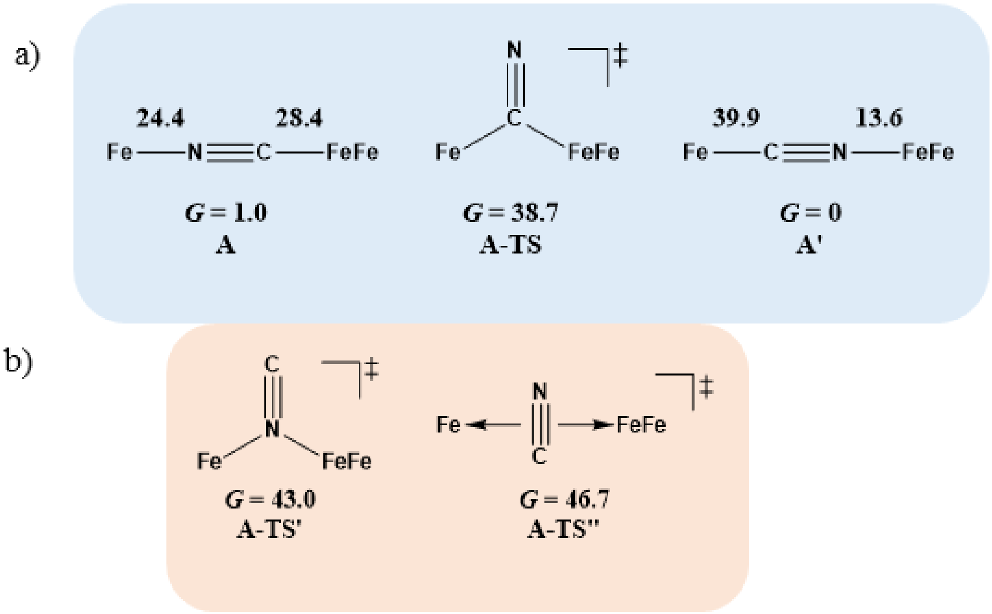

Figure III-6. a) Cyanide-flipped isomers of complex **A** and a possible transition state connecting them. Gibbs free energies Δ*G* of bond rupture of these species are given in kcal/mol with thermal and solvation corrections (solvent: acetonitrile). b) Other transition states that were optimized.

In **D-TS,** both iron moieties are dragged together by the bridging carbon and severe steric repulsion develops. Other trials to locate transition states, including a N-bridged **A-TS'** or a side-on / η^2-bridged **A-TS''** of complex **A**, were attempted but yielded higher barriers, G = 43.0 and 46.7 kcal/mol, respectively (Figure III-6b).

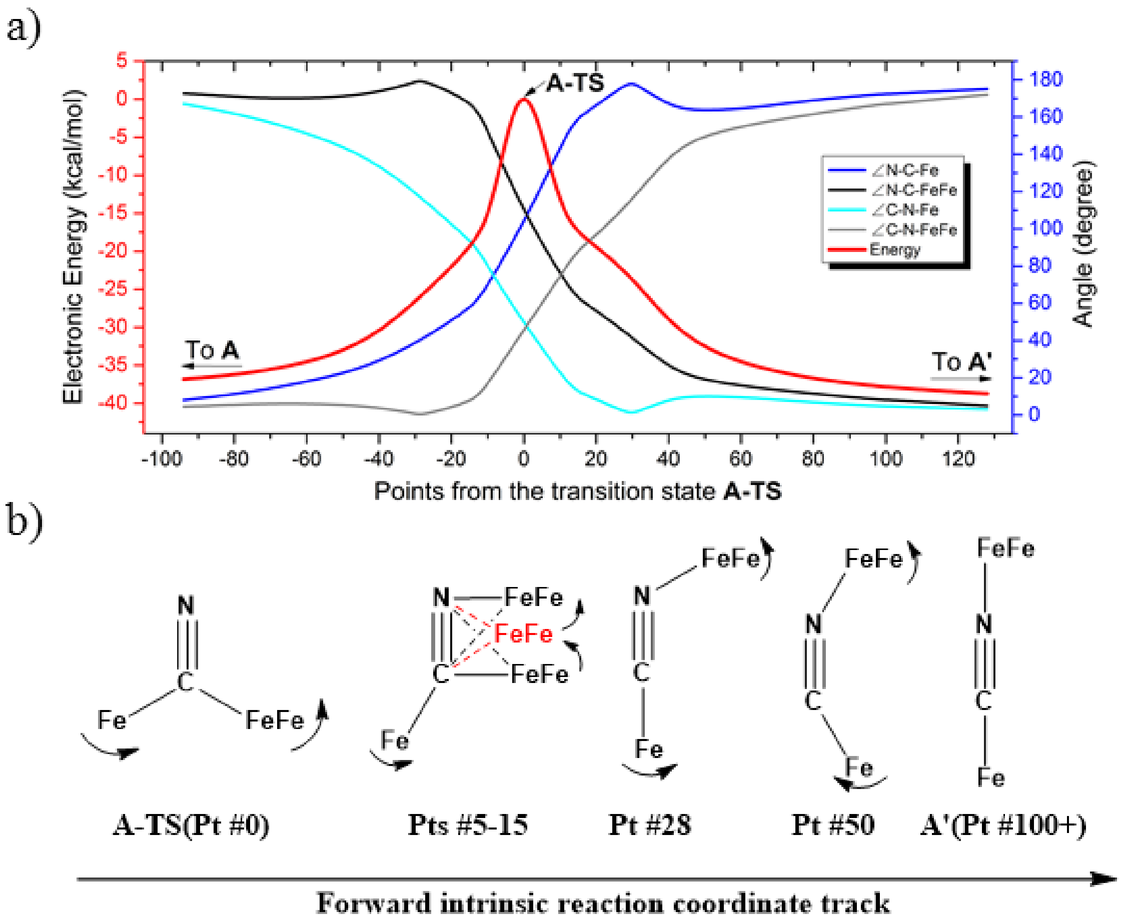

Figure III-7. a) Electronic energy and selected metric data plot of the intrinsic reaction coordinate (IRC) connecting **A** and **A'** through **A-TS**. (The left (red) *y*-axis is for energy, and the right (blue) *y*-axis is for bond angles.) b) The geometries of selected points on the IRC; the motions are indicated by arrows. The shifting of the FeFe moiety on CN is reflected by the sketches of Pts # 5-15.

A recent paper[137] expounded on the fact that the nitrogen end of the cyanide anion has stronger affinity to H-bond than the carbon end. Thus an interesting question is whether properly arranged H-bond providers can compensate the loss of N-M bond and facilitate the flipping. Thus, we tested the effects of one or two waters, one urea and one protonated pyridine as H-bond providers. However, none of them significantly stabilize the transition state.

To assess the possibilities of intermolecular mechanisms, the isomerization of fragment **1** (Figure III-1) in complex **A** was first evaluated computationally. The isomerized species **1'**, with a N-bound terminal cyanide, is 14.6 kcal/mol less stable than **1**. The barrier is 28.2 kcal/mol and the transition state **1-TS** features a side-on cyanide. On top of that, it takes 24.4 kcal/mol to dissociate fragment **1** from **A** (Figure III-6). Alternatively, a $(CO)_2Fe(NC)$ fragment (**z'**) may be cleaved from complex **A**. The barrier is 14.1 kcal/mol for **z'** to isomerize into fragment **z** (Chart 1), which is further stabilized by 15.9 kcal/mol compared to **z'**. Such an isomerization is also overwhelmed by the bond rupture energy of 28.4 kcal/mol (Figure III-6). Therefore the intermolecular mechanisms are actually more difficult to access than the intramolecular one presented above.

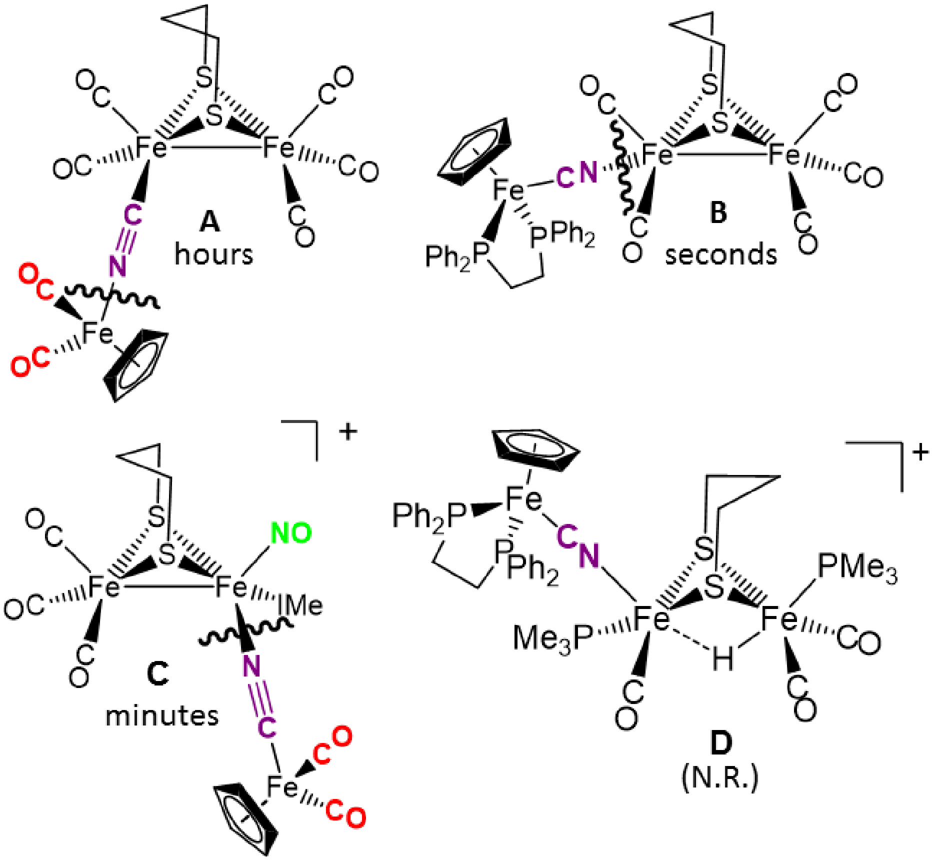

Figure III-8. Depiction of the cleavage site of the four bridging cyanide complexes with one equivalent of a strong nucleophile (such as PMe_3) and the relative time to completion.

Disruption of the Cyanide-bridged Adducts

Figure III-8 summarizes results of exposure of the four µ-CN triiron complexes to PMe_3, in possible mimicry of the release or transfer of the diiron unit from the [4Fe4S] cluster of the “loaded” HydF, see Figure I-7. All reactions were carried out with 1:1 ratios of phosphine ligand in THF at 22 °C; the time required for complete reaction correlates with expectations for the strength of the CN-Fe interaction. No reaction was observed for what is expected to be the tightest adduct, **D**. In the cases of adducts **A**, **B** and **C**, cleavage of the cyanide bridge occurred at the CN-Fe dative bond.

Comments

Examples of the two possible orientations Fe^{II}-NC-[$Fe^{I}Fe^{I}$] vs. Fe^{II}-CN-[$Fe^{I}Fe^{I}$] are readily obtained by judicious choice of metallocyanide donor “ligand” with an electrostatically-matched iron receiver. In no case did the orientation of the Fe-CN-Fe’ unit differ from the original components; i.e., as described by Vahrenkamp, the specific linkage isomer is a kinetic isomer, predetermined by the precursors.[127] Thus, the application of these results to the synthesis of the bio-hybrid via HydF[28] and other CN-bridged polymetallics[124-126] where such cyanide flipping has been observed raises questions. For example, how do successive isomerizations take place in the molecular analogues of Prussian Blues, where three CN^- are flipped per M···M’ interaction in the arrangement of $M_2M'_3$ systems[126]?

The MCN···M’ interactions that are readily derived in the organometallic cyanides in our study and in that of Zhu and Vahrenkamp[127] show strength and stability that relate to the electrostatic differences in the donor/acceptor precursors. Neither cyanide transfer nor flipping was observed in our biomimetic studies of M-CN···M’ adduct formation. Obviously, our studies were carried out in organic solvents wherein the specific H-bonding capabilities and complexity of a protein matrix are missing. The recent description of rigidity of the 2Fe subsite cavity in apo-HydA that is preserved after the enclosure of the synthetic 2Fe model corroborates the need for a specific matrix that adapts the symmetrical synthetic diiron complex into a structure that is efficient for catalysis.[63]

Such outer sphere effects on the inner coordination sphere structure of a diiron complex has yet to be imitated.

Based on the biomimetic study results, the energetic preference for the linkage isomers in the protein cavity-enclosed cases and the reported cyanide flipping is still perplexing. Might there be an alternative interpretation of the link between the [4Fe4S] cluster and the 2Fe synthetic unit in the hybrid form of HydF? As there has been no crystal structure of this assembly (reported as of now) more detailed EPR experiments are needed both on the biohybrids and on faithful, well characterized models.

While such questions persist, it is clear that the qualities that cyanide offers as a bridging ligand well suit them as docking agents for broad applications in bioinorganic chemistry as has been found in materials synthesis. The results above demonstrate the feasibility of stable small molecule paradigms expected for the docking of synthetic diiron cyano complexes into a protein cavity containing an Fe receiver group. Potential roles of the cyanide ligand in the H-cluster of [FeFe]-H_2ase now include not only the stabilization of multiple redox levels, and tuning the basicity of the pendant amine, but additionally CN^- is a group for directing pre-formed metal fragments into proteins.

CHAPTER IV

CATALYSIS AND MECHANISM OF H_2 RELEASE FROM AMINE-BORANES BY DIIRON COMPLEXES[*]

Introduction

The storage and transportation of H_2 is an essential component of any future economy based on this high energy, highly volatile fuel. Amongst various materials and compounds suggested for the storage challenge of this lightest of gases are amine boranes, [$H_3B \leftarrow NH_nR_{3-n}$ (n = 0-3)], as they have a high gravimetric H_2 content and are relatively stable.[138-141] In fact, the controlled H_2 release, dehydrogenation, of these compounds typically uses transition metals as catalysts.[142-147] As most such complexes are based on precious metals, there is interest in developing first row transition metals as more sustainable catalysts.[148-151] A mechanistic understanding of such catalysis and likely intermediates is key not only to optimizing the dehydrogenation process, but might also offer insight into the even greater specific challenge of the reverse reaction, i.e., the hydrogenation of the boron-nitrogen product.[152-157]

---

[*] Reprinted with permission from Lunsford, A. M.; Blank, J. H.; Moncho, S.; Haas, S. C.; Muhammad, S.; Brothers, E. N.; Darensbourg, M. Y.; Bengali, A. A. *Inorg. Chem.* **2016**, *55*, 964. Copyright **2016** American Chemical Society.[158]
The computational results and their description presented in this chapter were performed by Salvador Moncho at Texas A&M University at Qatar.

It is therefore important to quantify the extent of amine-borane dehydrogenation by such catalysts, and to also identify and study the reactivity of the intermediates that are formed during H_2 release. The reaction is expected to proceed by way of an initially formed M-H-B complex which, due to the hydridic nature of the B-H bond, is characterized to be dominated by the sigma donation from borohydride as ligand to the metal with a low back-donating component.[159-162] Although there is spectroscopic and crystallographic evidence for several such complexes, few studies have investigated the reactivity of such species.[163-165]

The potential utility of amine-boranes as H_2 storage materials together with the quest for greener and lower cost catalysts has led to the application of molecular Fe compounds for the dehydrogenation process. Vance, *et al*. have explored Fe(II) complexes of the type $[(\eta^5\text{-}C_5H_5)Fe(CO)_2X]$ and $[(\eta^5\text{-}C_5H_5)Fe(CO)_2solv]^+$ as catalysts for H_2 release from the secondary amine borane, $B{:}A^S$, concluding that the binding of boron-hydride to an open site on the iron center was a key step in the reaction mechanism that led to heterolytic coupling of H^+/H^- and H_2 release with formation of $H_2B{=}NR_2$ followed by dimerization.[160] Experimental evidence supported by DFT calculations supported the initial formation of a Fe-(μ-H)-B species as a key reaction intermediate.[166]

As mimics for the active site of hydrogenase enzymes which catalyze the reversible oxidation of H_2, diiron model complexes with key features of the diiron catalytic site, $(\mu\text{-}SCH_2XCH_2S)[Fe(CO)_3]_2$, have been extensively characterized. Figure IV-1 presents the complexes chosen for our current study, differing from each other by the nature of X (X = CH_2, CMe_2, CEt_2, NMe, NtBu, and NPh; **1**-CO through **6**-CO, respectively).[72,75,76,92] Here structures from X-ray diffraction data are reproduced in order to emphasize the steric properties of the bridgehead substituent. Earlier photochemical experiments demonstrated efficient loss of a single CO from complex **1**-CO upon exposure to UV light and established the propensity of the coordinatively unsaturated diiron unit to scavenge and bind substrates such as olefins or alkynes.[120] The (μ-SRS)$[Fe(CO)_3]_2$ complexes therefore appear to be ideally formulated for the binding of substrates including hydrides (in the form of amine-boranes) and H_2 upon photochemical activation.

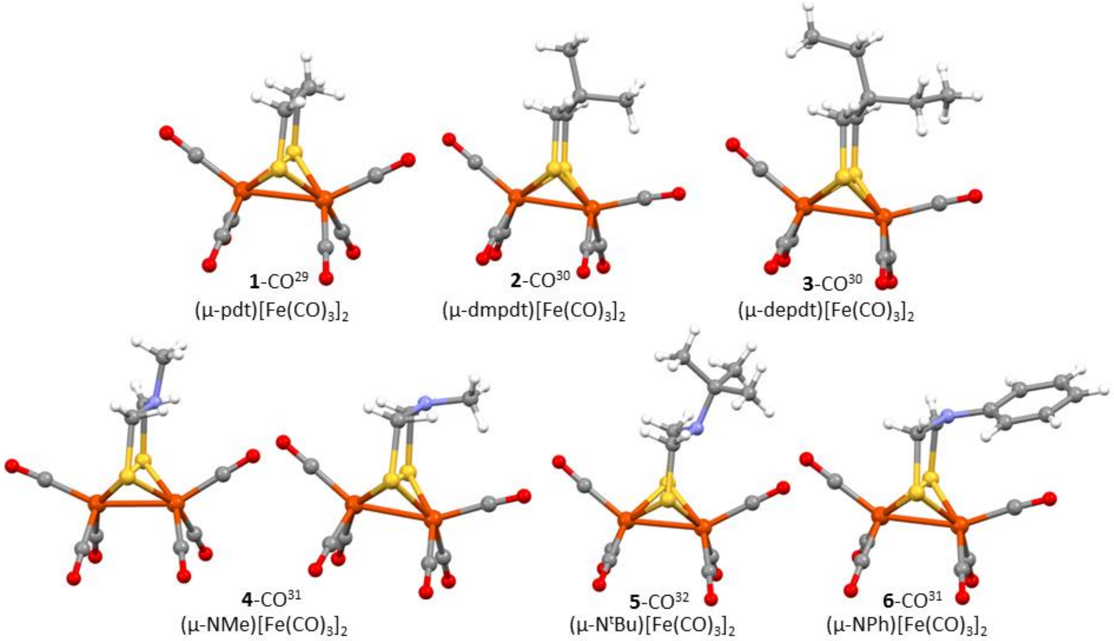

1-CO[29]
(μ-pdt)$[Fe(CO)_3]_2$

2-CO[30]
(μ-dmpdt)$[Fe(CO)_3]_2$

3-CO[30]
(μ-depdt)$[Fe(CO)_3]_2$

4-CO[31]
(μ-NMe)$[Fe(CO)_3]_2$

5-CO[32]
(μ-N^{t}Bu)$[Fe(CO)_3]_2$

6-CO[31]
(μ-NPh)$[Fe(CO)_3]_2$

Figure IV-1. Molecular crystal structures from XRD of diiron complexes used as dehydrogenation catalysts. The structures of 4-CO depict the two different orientations of the lone pair of electrons on the nitrogen i.e., pointed towards the iron center (left) or away (right). Both isomers are present in the crystal structure. Abbreviations: pdt = propane dithiolate; dmpdt = dimethylpropane dithiolate; depdt = diethylpropane dithiolate. See Figure IV-2 for a chemdraw representation of the structures.

The six complexes in our study are well characterized in the solid state and in solution. Dynamic NMR studies noted effects of bridgehead steric bulk (comparing complexes **1**-CO, **2**-CO and **3**-CO) on the $Fe(CO)_3$ rotor mobility; experimental activation barriers were supported by DFT-calculated $Fe(CO)_3$ rotational barriers.[75,76] The interconversion of the boat/chair confirmation allows the central atom of the dithiolate linker to flip back and forth between the two metals and access the catalytically relevant iron assuming there is an open site as in the enzyme. Exchange of the apical/basal COs through Fe-CO rotation results in equivalent CO ligands as is evident by a single CO resonance in the 13-C NMR. This rotational barrier is influenced by the identity of the central atom of the S-S linker and the steric hindrance placed on the apical CO. Increased steric bulk results in a decreased barrier to rotation and the proposed transition state can be seen in Figure I-10. Both of these processes are not present in the natural enzyme due to hydrogen bonding to the diatomic ligands and the NH bridgehead described above. By immobilizing these features, the active site, with an open site on the iron, is locked in a confirmation for optimum catalytic efficiency. As the $(\mu\text{-SRS})[Fe(CO)_3]_2$ complexes are known to be electrocatalysts for H^+ reduction to H_2, the series was also explored for bridgehead effects of the μ-SRS dithiolate linker.[76] Cyclic voltammetry experiments found the pendent base (as in **4-**CO, **5-**CO, **6-**CO) to have a small but positive effect on proton uptake in reduced species.

An increase in activity upon introduction of the nitrogen atom in the dithiolate linker is consistent with the established pendent base/proton shuttling effect in the well-known DuBois nickel catalyst.[30] A similar heterolytic oxidation of H_2 was studied in a series of diphosphine substituted [FeFe]-hydrogenase complexes featuring the PNP ligand similar to the one used by DuBois, *et al.*[167] If the PNP ligand is substituted with an all-carbon diphosphine the activity of H_2 oxidation is completely lost, an observation that highlights the essential role played by the pendent base.

(**a**) The Catalysis

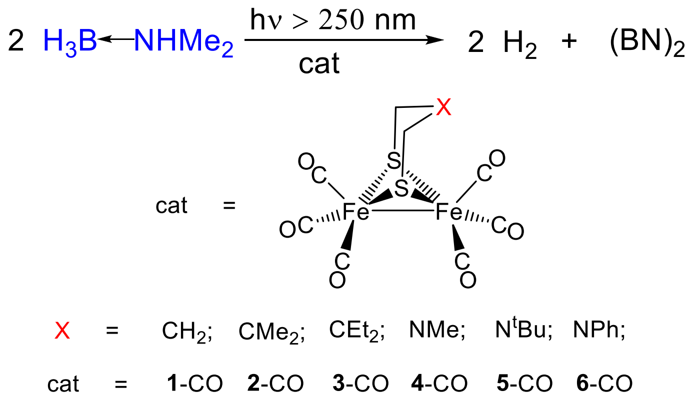

(**b**) Binding ability of B:A^t

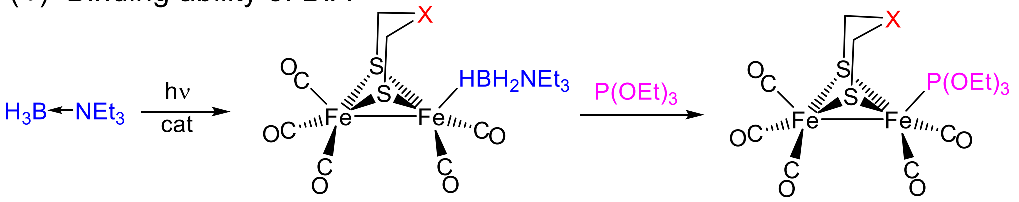

1-B:A^t through **6**-B:A^t **1**-P(OEt)$_3$ through **6**-P(OEt)$_3$

Figure IV-2. (a) Catalysts used in the dehydrogenation of B:A^s. (b) Comparative kinetic study of the lability of the 1-B:A^t through 6-B:A^t adducts.

Herein we report the use of such complexes as photocatalysts for H_2 release from $H_3B{\leftarrow}NHMe_2$, B:A^s, Figure IV-2a. Photolysis is required to remove a CO and open a site for substrate binding; the quantity of hydrogen released is monitored with time. As H_2

release does not occur in the tertiary amine analogue, $H_3B \leftarrow NEt_3$ B:A^t, a unique opportunity exists for exploration of a likely intermediate involving the binding of the borohydride. Hence we describe a mechanistic study focused on the reactivity of the initial species formed upon photolysis of several diiron complexes in the presence of the tertiary amine-borane, B:A^t, Figure IV-2b. A prominent feature of the selection of diiron complexes is the potential for a pendent base effect on the progress of the reaction. We relate the lability of the initially formed, complexes 1-B:A^t through 6-B:A^t, as affected by steric constraints at the binding site, to the overall H_2 release efficiency when a secondary amine-borane, B:A^s, is used as the substrate.

H_2 Release from B:A^s

We have examined the series of complexes in Figure IV-1 for their mediation of H_2 release from the secondary amine-borane, B:A^s according to Figure IV-2a. Gases which were released during continuous photolysis of the reaction mixture were collected and measured as described in the experimental section. One mol of H_2 per mol of B:A^s was evolved over the course of the reaction. A minor amount of CO was present in the measurements as expected from the known photolability of CO from these complexes. This was further confirmed by measuring the gas obtained from photolysis of the diiron complex in the absence of B:A^s . On average, 3 mols of CO were obtained per mol of diiron catalyst over the course of ca. 2h. Analysis of the final solution by FTIR finds CO absorption peaks consistent with the remaining (μ-SRS)$[Fe(CO)_3]_2$ complexes and a degradation product with an absorption pattern consistent with a monosubstituted pentacarbonyl species, presumably solvated (μ-SRS)[$Fe_2(CO)_5$-solv]. A dark brown/black decomposition solid was also deposited on the sides of the flask.

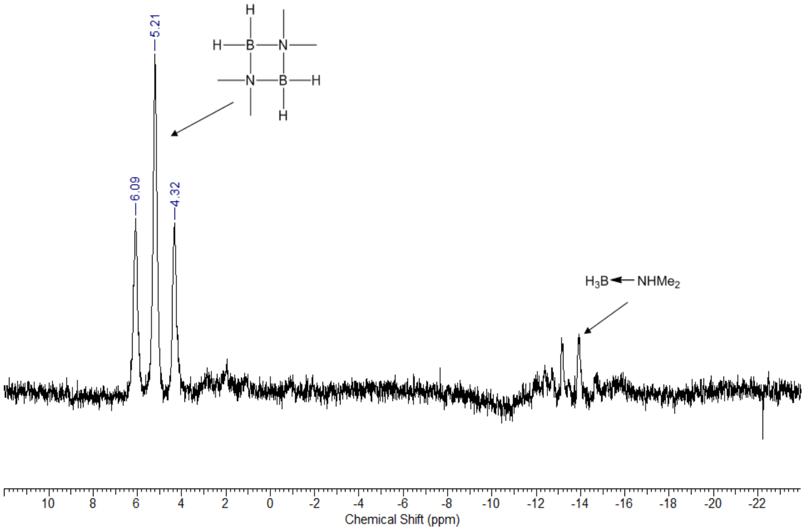

Figure IV-3. Solution ^{11}B NMR of the reaction mixture from the dehydrogenation using 1-CO as the catalyst in d_8-THF. The triplet centered at 5.21 ppm corresponds to the cyclic by-product.

The boron-containing product from an H_2 production experiment with **1**-CO as the catalyst, was investigated by ^{11}B NMR. The spent solution displays a triplet centered at 5.21 ppm, referenced to $BF_3 \cdot Et_2O$ = 0.0 ppm, Figure IV-3, corresponding to the $[H_2B\text{-}NMe_2]_2$ cyclic dimer, as characterized in analogous metal carbonyl photocatalyzed H_2 release reactions.[168] A quartet for the amine-borane starting material is still present in low abundance at -13.5 ppm.

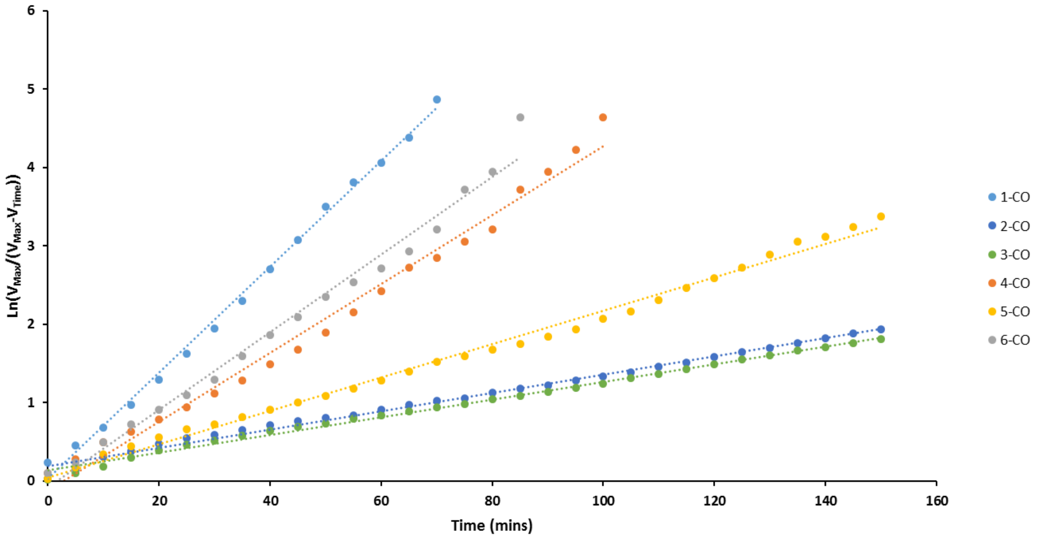

Figure IV-4. Plots of rates of H_2 released from photolysis of THF solutions of B:A^s in presence of diiron carbonyls as catalysts, 1-CO through 6-CO. Each data point is the average of three separate runs.

The natural log plots of H_2 collection from multiple experiments are presented in Figure IV-4**,** demonstrating varying rates of H_2 release. A linear correlation indicates 1st order release of H_2 from B:A^s with the slope of the line of best fit used to rank the catalysts. The final volume of gas collected averages to 20.54 ± 0.13 mL over all the reactions. However there are significant differences in the length of time it takes to reach completion. Complex **1**-CO had the fastest rate of H_2 production with gas evolution ceasing after 85 min. Reflecting the need for an open site on the catalyst, there is an initial induction period of ca. 10 min prior to the development of the plots above that analyze for first order kinetics. Conclusions regarding the rate dependence on μ-SRS bridgehead are discussed below.

Kinetic Studies (Single Shot Laser Photolysis)

Previous studies of low valent metal carbonyls as photocatalysts for H_2 release from amine-boranes have suggested a boron-hydride-M(CO)$_X$ adduct as a key intermediate required for bond activation. This hypothesis is further supported by DFT calculations and ^{11}B NMR studies.[169] Photolability of CO in complexes **1**-CO through **6-**CO produces a key species which may be scavenged by the amine-borane as expressed in Figure IV-2b. We have also characterized the reactivity of the **1-**B:A^t through **6**-B:A^t adducts, the second step of the reaction in Figure IV-2b, which unlike the **1-**B:A^s through **6**-B:A^s complexes, do not proceed towards dehydrogenation. The aim was to correlate the lability of these adducts with the rate of H_2 release from the analogous **1-**B:A^s through **6**-B:A^s complexes described above. Previously, a similar kinetic method was successfully used to investigate the reactivity and binding enthalpy of weakly coordinated substrates such as alkenes, alkynes, and furans to the iron center in **1**-CO.[120]

Single shot photolysis of **5**-CO (2.2 mM) in methylcyclohexane solution at room temperature in the presence of 0.47 M B:A^t results in the formation of a new complex absorbing at 2042, 1985, 1965, and 1924 cm^{-1} (Figure IV-5). In the presence of the secondary amine-borane, B:A^s, a species with almost identical CO stretching frequencies (2043, 1988, 1971, 1939 cm^{-1}) and pattern is observed suggesting that the structures of the initial complexes in both cases are very similar. Hydrogen gas generated upon photolysis in the IR cell precluded further investigation of the reactivity of the FeFe-B:A^s adduct.[140,146,162,163,169]

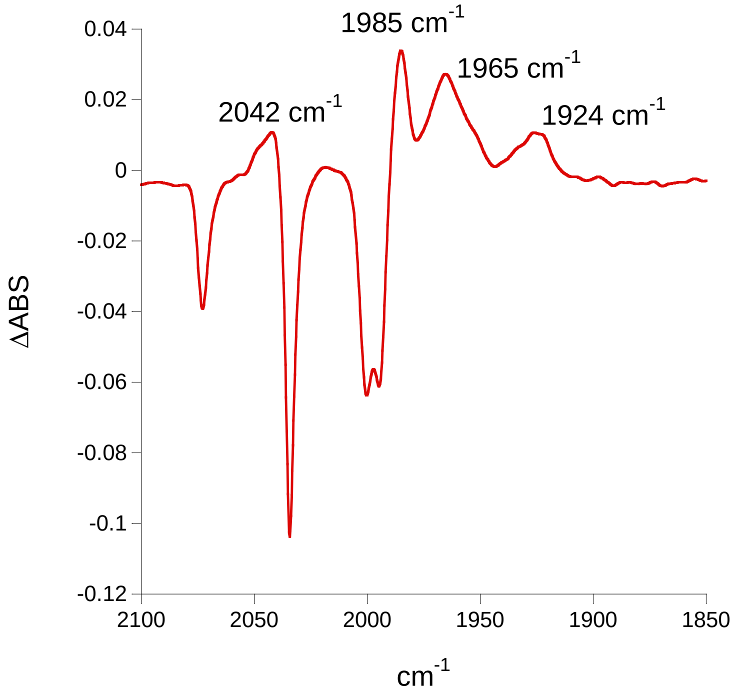

Figure IV-5. Difference IR spectra obtained upon photolysis of 5-CO in the presence of 0.47 M B:At at 298 K. The positive peaks are due to the formation of an intermediate, assigned to 5-B:A^t (see Figure IV-6) and the negative peaks are due to the loss of 5-CO.

Since UV photolysis of metal carbonyls such as **1**-CO in the presence of classical coordinating ligands such as PR_3 or $P(OEt)_3$ results in CO loss and formation of the corresponding ligated product,[120] we assign this species to the **5**-B:A^t complex. Similar species are known to form upon photolysis of other metal carbonyls in the presence of tertiary amine-boranes and some have been isolated and fully characterized.[170-173] The geometry of the B-H-M interaction, with a relatively large angle (135.2°) supports our supposition that this interaction derives from sigma donation of electron density on the hydride (Figure IV-6) with scaled computed ν_{CO} bands which are in good agreement with the experimental values.

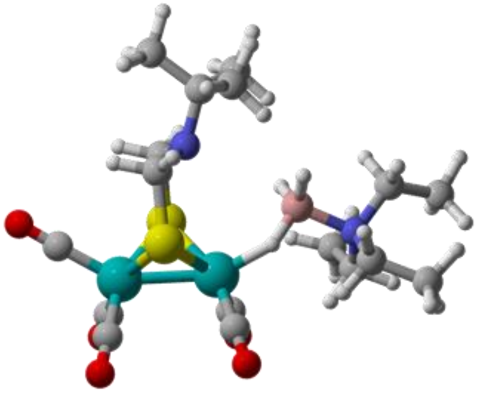

Figure IV-6. Calculated structure of **5-B:A^t**

In the absence of other coordinating ligands, **5**-B:A^t is relatively stable with a $t_{1/2}$= 51 s at 298 K. However, addition of $P(OEt)_3$ to the photolysis solution results in the conversion of **5**-B:A^t to a new complex absorbing at 2049, 1990, 1969 and 1940 cm^{-1} which grows in at the same rate (Figure IV-7). Since photolysis of **5**-CO in the presence of only $P(OEt)_3$ also yields the same product, this species is assigned to the **5**-$P(OEt)_3$ complex. The displacement of B:A^t from the iron center was studied over a wide range of [$P(OEt)_3$] and temperatures.

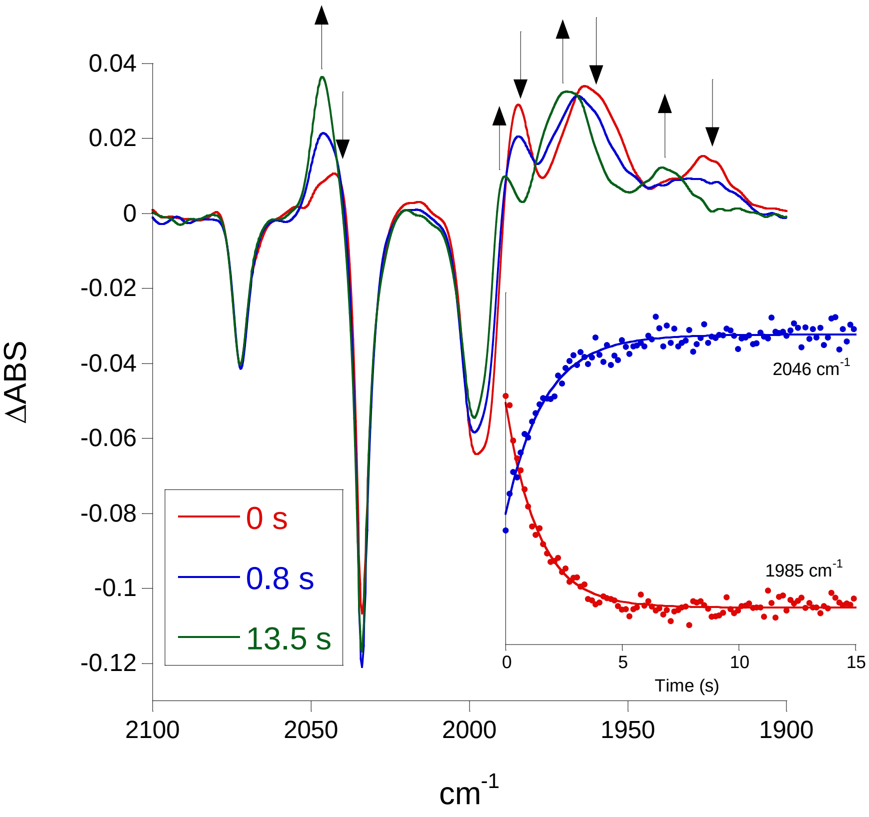

Figure IV-7. Spectral changes observed upon photolysis of 5-CO in the presence of 1.35 M B:A^t and 0.117 M P(OEt)$_3$ at 283 K in methylcyclohexane. Peaks due to 5-B:A^t and 5-P(OEt)$_3$ decay and grow, respectively, at the same rate.

As shown in Figure IV-8, when the concentration of B:A^t is held constant, k_{obs} exhibits a non-linear dependence on [P(OEt)$_3$], approaching a limiting value at high ligand concentration. The observed saturation behavior is consistent with the dissociative mechanism shown in Figure IV-9. Application of the steady state assumption to the intermediate complex, [**I**], results in the k_{obs} concentration dependence shown in Eq. IV-1. The limiting value of k_{obs} yields k_1, the rate constant for the dissociation of the **5**-B:A^t adduct.

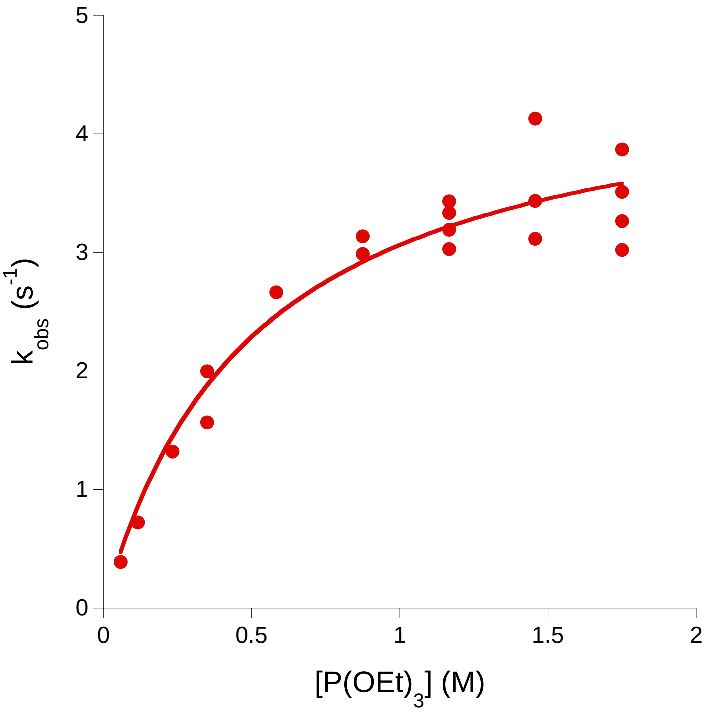

Figure IV-8. k_{obs} dependence on [P(OEt)$_3$] at 283 K with [B:A^t] = 1.35 M.

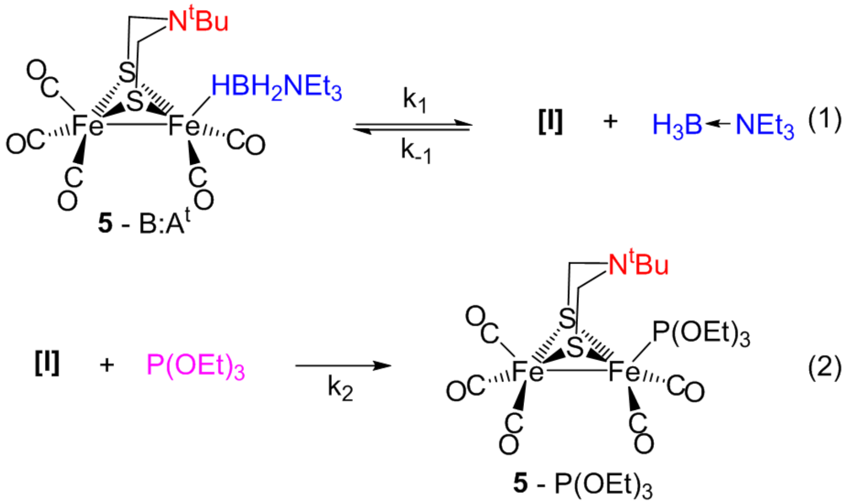

Figure IV-9. Dissociative mechanism of amine-borane substitution from the iron center.

$$k_{obs} = \frac{k_1 k_2[P(OEt)_3]}{k_{-1}[B^tA] + k_2[P(OEt)_3]} \qquad \text{(Eq. IV-1)}$$

As discussed below, with the assistance of DFT calculations, **[I]** in Figure IV-9 is identified as a species in which the vacant site generated by loss of B:A^t is stabilized by an agostic interaction between the C-H bond of an alkyl group from the N^{t}Bu bridgehead and the iron center (Figure IV-10). The bent geometry of the M-H-C interaction, of angle 115.7°, contrasts to the B-H-M interaction, as expected for the greater covalency C-H bond relative to the polar-covalent B-H bond. While the barrier to N-inversion in (μ-SCH$_2$N(^{t}Bu)CH$_2$S) of coordinatively saturated **5**-CO prohibits such agostic interaction, it is expected to be much less in the coordinatively unsaturated species.

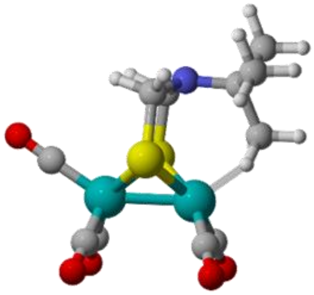

Figure IV-10. DFT calculated structure for the intermediate complex, **[I]** generated from 5-B:A^t.

Unfortunately, the displacement reaction could not be probed at high concentrations of [P(OEt)$_3$] at temperatures > 283K because of the rapid reaction rate and a reduction in the signal of **5**-B:A^t due to competitive binding of P(OEt)$_3$ with **5**. Therefore, the reaction was studied at relatively low [P(OEt)$_3$] concentrations and higher temperatures in order to obtain the relevant activation parameters. The results are shown in Figure IV-11.

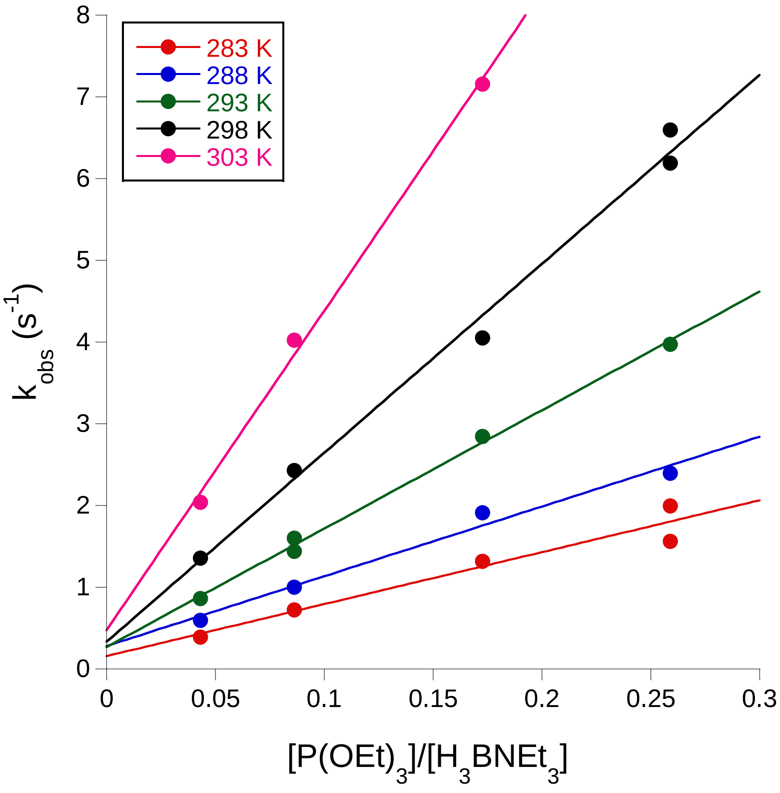

Figure IV-11. A plot of the k_{obs} versus [P(OEt)$_3$]/[B:A^t] at several temperatures. The non-zero intercepts are similar in magnitude to the background decay rate constant of 5-B:A^t in the absence of P(OEt)$_3$.

Under these reaction conditions (k_{-1}[B:A^t] >> k_2[P(OEt)$_3$]), a linear relationship between k_{obs} and reactant concentrations is expected since Eq. 1 simplifies to that shown in Eq. VI-2.

$$k_{obs} = k' \frac{[P(OEt_3)]}{[B^tA]} \left[k' = \frac{k_1 k_2}{k_{-1}}\right] \qquad (Eq. VI - 2)$$

A plot of k_{obs} vs. [P(OEt)$_3$]/[B:A^t] is linear and yields a slope of k' = k_1k_2/k_{-1}. As shown in Figure IV-12, an Eyring plot obtained from the temperature dependence of k' yields $\Delta H^{\ddagger}_{total}$= 15.1 ± 1.0 kcal/mol and $\Delta S^{\ddagger}_{total}$ = -1 ± 3 e.u. for the ligand exchange reaction where $\Delta H^{\ddagger}_{total} = \Delta H^{\ddagger}_{k_1} + (\Delta H^{\ddagger}_{k_2} - \Delta H^{\ddagger}_{k_{-1}})$ and $\Delta S^{\ddagger}_{total} = \Delta S^{\ddagger}_{k_1} + (\Delta S^{\ddagger}_{k_2} - \Delta S^{\ddagger}_{k_{-1}})$.

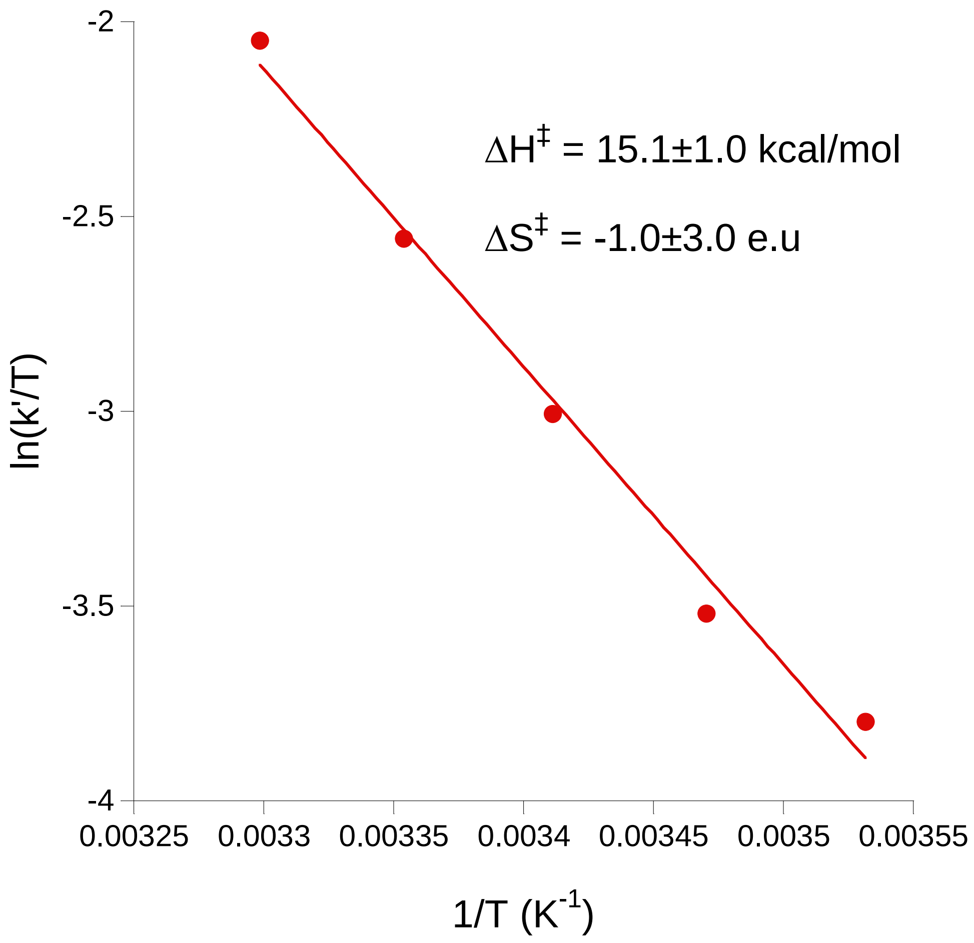

Figure IV-12. Eyring plot obtained from the temperature dependence of k'.

The measured activation enthalpy is in good agreement with a DFT calculated value of 17.6 kcal/mol for the difference in enthalpy between **5**-B:A^t and **[I]** + H_3BNEt_3. The close agreement between the experimental and calculated values suggests that the transition state structure is similar to that of the calculated geometry of the intermediate species and that reaction of **[I]** with B:A^t or $P(OEt)_3$ proceeds with similar activation barriers (i.e., $\left(\Delta H^{\ddagger}_{k_2} - \Delta H^{\ddagger}_{k_{-1}}\right) \approx 0$).

To study the influence of the bridgehead group on the reaction rate, the displacement of B:A^t by P(OEt)$_3$ from the respective diiron species was investigated under identical reaction conditions. As shown in Table 1, the reaction rate constants are largest for systems that have an alkyl group present on the bridgehead atom, regardless of whether it is carbon or nitrogen. The absence of alkyl groups as in **1**-B:A^t results in a k_{obs} for the displacement reaction that is a factor of 25-130 less than the other complexes studied. This observation suggests an important role for the alkyl groups in stabilizing the transition state accessed in the reaction.

Table IV-1. Observed rate constants (k_{obs} in s^{-1}) for the substitution reaction. All experiments were conducted under identical conditions of [B:A^t] (1.35 M) and [P(OEt)$_3$] (0.117 M).

T (K)	**CH$_2$ (1)**	**CMe$_2$ (2)**	**CEt$_2$ (3)**	**NMe (4)**	**NtBu (5)**	**NPh (6)**
283.15	-	3.2	5.85	1.64	0.72	1.52
288.15	0.04	4.96	*	2.62	1	2.23
293.15	0.05	6.41	*	3.34	1.44	3.16

*too fast to reliably measure.

To further probe the origin of the large reactivity difference between the alkylated bridgehead and X = CH$_2$ complexes, the complete kinetics of B:A^t substitution from **1**-B:A^t was studied. As shown in Figure IV-13, in contrast to the **5**-B:A^t system, the observed rate of B:A^t displacement from **1**-B:A^t exhibits a linear dependence on [P(OEt)$_3$] even at the highest concentrations used and at all temperatures studied. An Eyring plot yields activation parameters of $\Delta H^\ddagger = 7.1 \pm 0.6$ kcal/mol and $\Delta S^\ddagger = -36 \pm 7$ e.u which, in dramatic contrast to the **5**-B:A^t system, are strongly indicative of a substitution mechanism with a bimolecular rate determining step. These results can be explained with the support of precedence (*vide infra*) and with the assistance of DFT calculations which predict a **1**-B:A^t bond dissociation enthalpy (BDE) of 25-30 kcal/mol (Table IV-2), much higher than the experimental enthalpy of activation. Without the ability to access a low energy intermediate analogous to [**I**], and a relatively large barrier for the dissociative channel, it is reasonable to expect that substitution of B:A^t from **1**-B:A^t may follow an associative or interchange pathway if the transition state energy lies below the dissociative limit.

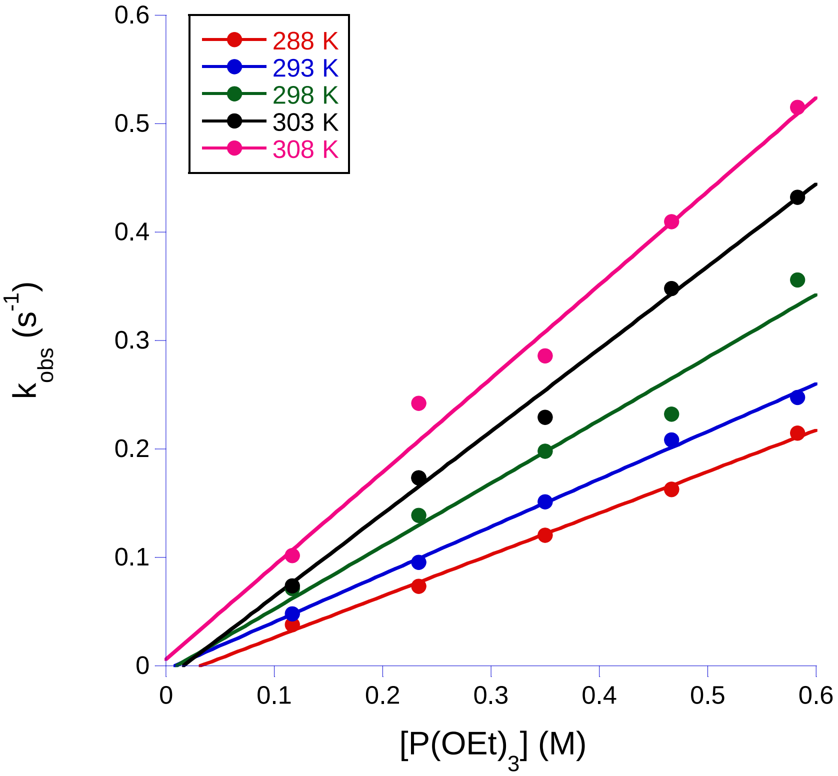

Figure IV-13. A plot of k_{obs} vs [P(OEt)$_3$] for the displacement of B:A^t from 1-B:A^t by P(OEt)$_3$.

Consistent with this analysis, the experimental activation parameters for the bimolecular reaction yield a $\Delta G_{298}^{\ddagger}$ of 18 ± 2 kcal/mol which is on the order of, or lower than, a calculated value of $\Delta G_{298}^{\ddagger}$ = 19-23 kcal/mol for the dissociative step (the energy range is due to the presence of different structural isomers).[174] A bimolecular pathway for B:A^t displacement from the **1**-B:A^t complex is not without precedence. Previous studies have demonstrated convincingly that thermal displacement of CO from **1**-CO by CN$^-$ proceeds in a S_N2 manner.[69,78] By analogy with this earlier study, it is expected that nucleophilic attack of the $P(OEt)_3$ ligand results in the displacement of the Fe-Fe bond density with concomitant rotation of the $Fe(CO)_2$(B:A^t) group placing a CO below the Fe-Fe vector in position to interact with the increased electron density of the unrotated Fe. Reformation of the Fe-Fe bond results in ejection of B:A^t to form the product complex (Figure IV-14).

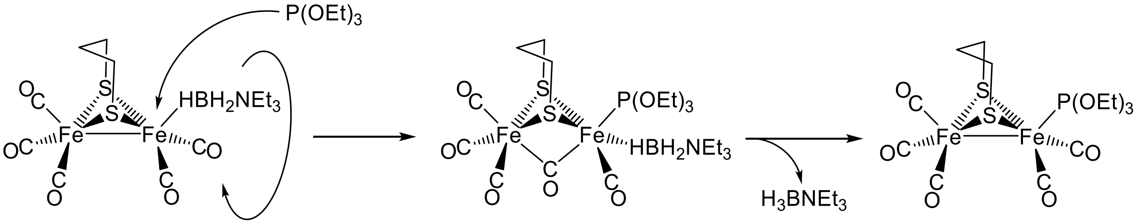

Figure IV-14. Proposed bimolecular mechanism for the substitution reaction in Figure IV-2b of 1-B:A^t (i.e., the (μ-pdt) diiron complex).

Computational Studies for the Intermediates

Computational methods evaluated the energetics of the possible products of H-B coordination of B:A^t in complexes **1-**B:A^t through **6-**B:A^t, as well as the related unsaturated complexes. For each complex, all possible coordination geometries were analyzed. Geometry optimizations were done using the ωB97XD/Def2TZVPP level of theory; detailed methodology description is provided in the methods section.

The experimental findings are consistent with DFT calculations which indicate that for all complexes except **1**-B:A^t, the vacant coordination site generated upon borane dissociation is stabilized by an agostic interaction between the Fe center and the C-H bond of an alkyl group on the bridgehead atom. For complex **5**, this intermediate is calculated to be 9.5 kcal/mol more stable than the uncoordinated species. An alternate structure for [**I**] would involve solvent coordination to the vacant site to form the solvated species. Indeed, DFT calculations predict a solvation enthalpy of 8.8 kcal/mol for such a complex. While the stabilization enthalpies are similar for the agostic and methylcyclohexane solvated structures, the generation of the former complex by an intramolecular interaction would make it kinetically favored over the latter species.

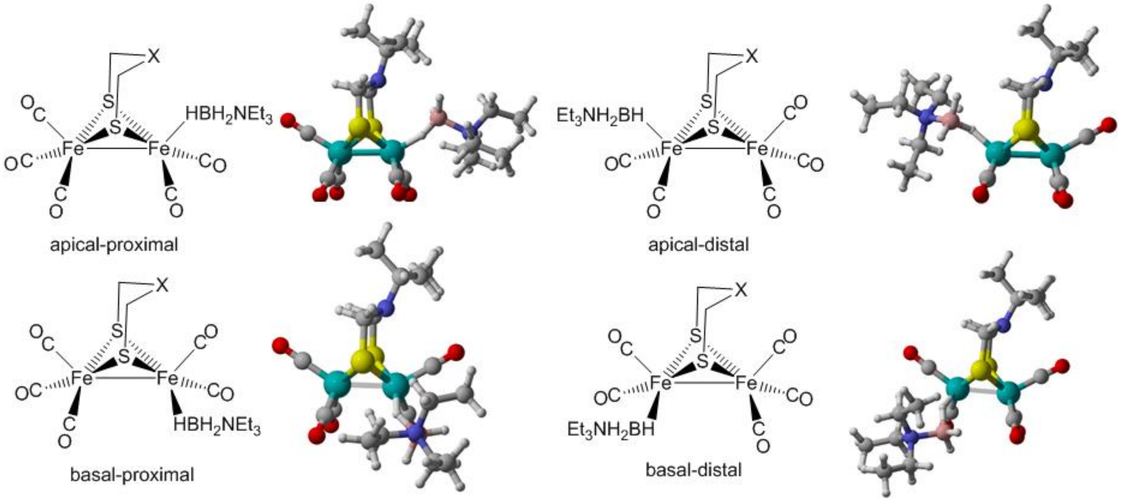

Figure IV-15. All possible geometries adopted by 1-B:A^t through 6-B:A^t. DFT calculated geometries for 5-B:A^t are in color.

The structures of **1-**B:A^t through **6-**B:A^t were calculated using DFT. Due to the symmetry of the complex, four isomers are possible (Figure IV-15). The geometry of the M-H-C interactions for the complexes with different bridgeheads are in agreement with the analysis for 5-B:A^t. A description of the fluxionality of the bridgeheads and the $Fe(CO)_3$ rotor activity in complexes (**1-**CO through **6-**CO) can be found in ref [76]. The amine-borane ligand can be either directly coordinated under the bridgehead (proximal) or on the other metal center (distal) and it can occupy either an apical or basal site. The modeling results rule out the possibility of an electronic influence of the bridgehead atom, N or C, upon the Fe-B:A^t bond dissociation enthalpy (BDE). For similar isomers of the respective complexes without agostic stabilization of the vacant site (e.g., the open site generated from the basal-distal isomer, Figure IV-15), the Fe-B:A^t BDE's remain essentially unchanged for **1-**B:A^t (24.8 kcal/mol), **4-**B:A^t (25.3 kcal/mol), and **5-**B:A^t (24.9

kcal/mol). The distinguishing feature between **1**-B:A^t and all other complexes is the absence of alkyl groups on the bridge. The presence of a nitrogen heteroatom does not appear to play a major role in the rate of substitution nor in determining the Fe-B:A^t BDE, however the alkyl substituent on the N is influential.

When referenced to the same state (i.e., unstabilized vacant Fe coordination site upon B:A^t dissociation), the calculated **5**-B:A^t BDE's are within 3 kcal/mol for the four possible structures with the apical-distal geometry resulting in the most stable arrangement (Table 2). The similar stabilities together with the fact that interconversion of these isomers is expected to be rapid at the temperatures used, suggests that the substitution reactions will originate from the isomer that has the lowest barrier to B:A^t dissociation. For the alkylated bridgehead complexes, this isomer is the apical-proximal structure since it places the alkyl group in the correct position to stabilize the vacant coordination site through a Fe-H-C agostic interaction. In cases where an alkyl group is present on the bridgehead, this agostic stabilization is calculated to be ≈ 3-10 kcal/mol and the lower energy of the resulting transition state yields a faster substitution rate relative to **1**-CO which lacks this bonding possibility. As mentioned earlier, the calculated 17.6 kcal/mol **5-**B:A^t BDE is in good agreement with the experimental activation barrier of 15.1 kcal/mol suggesting that the substitution reaction proceeds by way of the alkyl stabilized intermediate and that this agostic bond is mostly formed in the transition state.

Table IV-2. DFT calculated 1-CO through 6-CO bond dissociation enthalpies for the complexes studied. The bolded numbers refer to species in which the vacant site generated upon loss of borane is stabilized by an alkyl C-H agostic interaction with the metal center Figure IV-9.

	CH_2 (1)	**CMe_2 (2)**	**CEt_2 (3)**	**NMe (4)**	**NtBu (5)**	**NPh (6)**
apical-proximal	27.6	**21.8**	**18**	**20.1**	**17.6**	**16.7**
apical distal	29.5	30.1	30.8	29.2	29.2	30.1
basal-distal	24.8	24.8	24.3	25.3	24.9	25
basal proximal	27.6	26	25.9	25.8	27.4	29.8

Correlation between Borane Substitution Rates and the Rate of H_2 Formation

It is assumed in the following analysis that the trend in the kinetic stabilities of **1-**B:A^t through **6-**B:A^t are similar to those of the **1-**B:A^s through **6-**B:A^s adducts which yield H_2. The correlations for k_{obs} (i.e., the rate constant for the displacement of amine-borane by $P(OEt)_3$) and the rate of H_2 release are then based on two assumptions a) the major B-H to Fe bond in the two adducts that precede bond activation, i.e., the Fe-Fe-(μ-H)-BH_2NEt_3 and the Fe-Fe-(μ-H)-BH_2NHMe_2, are largely the same; and b) only in the N-containing complexes **4-**CO, **5-**CO, and **6-**CO are there possible interactions of the amine-boranes with the N-bridgehead atoms when switching from the tertiary amine-borane (B:A^t) in the $P(OEt)_3$ kinetic studies to the secondary amine-borane (B:A^s) in the H_2 release studies.

Borohydride displacement, k_{obs} : **3-B:A**^{t} > **2-B:A**^{t} > **4-B:A**^{t} > **6-B:A**^{t} > **5-B**^{t}**A** >> **1-B:A**^{t}

H_2 Release : **1-B:A**^{s} > **6-B:A**^{s} > **4-B:A**^{s} > **5-B:A**^{s} > **2-B:A**^{s} ≅ **3-B:A**^{s}

Figure IV-16. Correlation of rates of B:A^{t} substitution from **1-B:A**^{t} through **6-B:A**^{t}, at room temperature, and relative rates of H_2 release from B:A^{s}. Complexes in red represent all carbon bridgeheads and complexes in blue feature a pendent amine.

As indicated in Figure IV-16, the H_2 release ranking is largely opposite that of the k_{obs} obtained for borohydride displacement ranking. We interpret this to mean that the stabilization of the intermediate **[I]**, the agostic interaction, correlates with slower H_2 release from the B:A^{s} substrate, indicating that the longer the lifetime of the later secondary amine-borane adduct, the more facile is the H_2 release process. Thus, complex **1**-B:A^{t}, the non-alkylated (pdt) complex, displays the slowest rate for B:A^{t} displacement, yet the fastest rates of H_2 release as compared to the dimethyl and diethyl derivatives. That is, the agostic C-H interaction with the open site from the dmpdt and depdt diminishes the residence time of the substrate. The only complex that does not follow an inverse order of H_2 production as compared to the k_{obs} for B:A^{t} displacement is **5**-B:A^{t}. This complex, which features the largest steric bulk compared to the other two nitrogen bridgehead derivatives, places an alkyl group close to the iron center similar to the carbon bridgehead species complexes **2**-CO and **3**-CO. A complexity of the **5**-B:A^{t} involves an inversion barrier at the nitrogen which could account for this discrepancy; as yet undefined features might be at play.

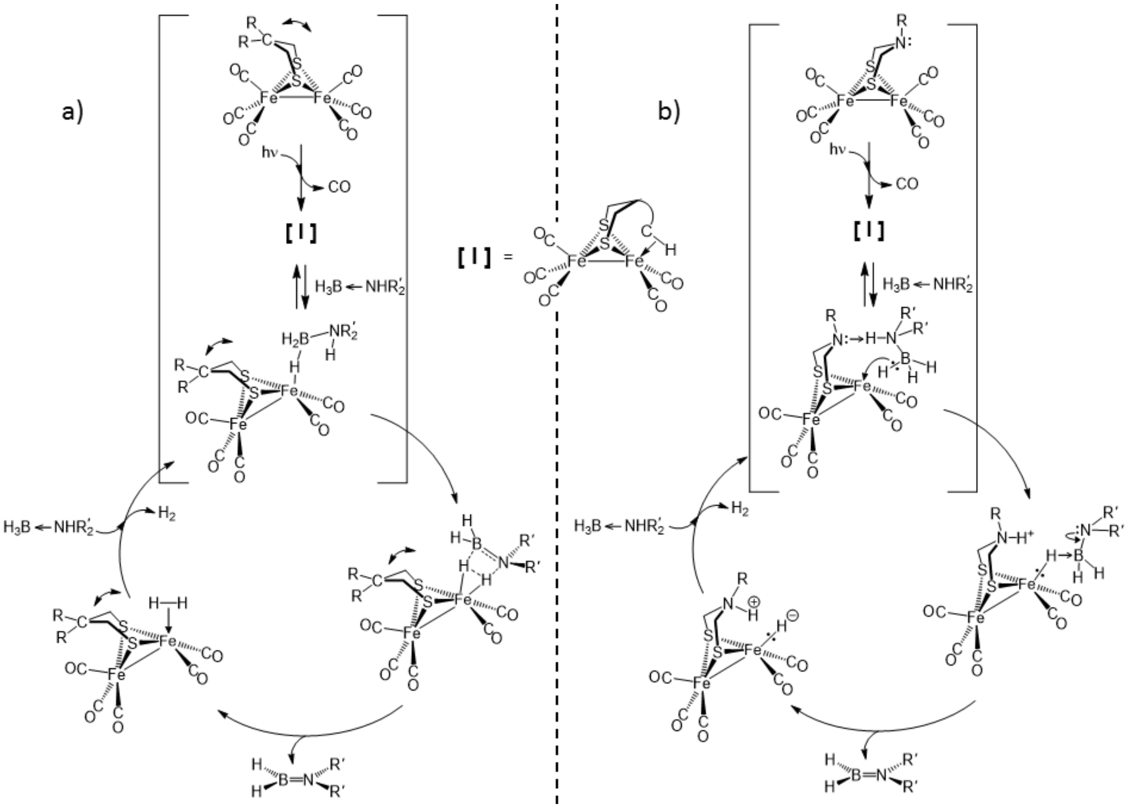

Figure IV-17. Minimal proposed mechanisms for dehydrogenation of amine-borane by a) C-bridgehead and b) N-bridgehead diiron complexes. Note, **[I]** is as defined in Figure IV-10 and the curved arrow at the bridgehead represents the flipping process available to the dithiolate linker. Experimental support is for the bracketed portion.

The mechanisms offered in Figure IV-17 add to the myriad possibilities already expressed for metal-catalyzed dehydrocoupling of amineboranes. In particular the computational study by Hall and Weller that explored the mechanism of dihydrogen release from a Rh(I) diphosphine complex was used to develop the mechanism displayed in Figure IV-17a.[169] In contrast, the N-bridgehead derivatives, complexes **4-**CO, **5-**CO, and **6-**CO**,** have the possibility for increased interactions due to the presence of a proton in the secondary amineborane as expressed in Figure IV-17b. Similar mechanisms were computationally and experimentally developed for two other studies, one featuring a mono Fe complex and another focusing on a Ru complex both of which contained a N-donor within a chelating ligand.[175,176] The heterolytic removal of both the proton and hydride from the amine-borane requires the N-bridgehead and bears similarity with the H^+/H^- production (or oxidation) of H_2 in the [FeFe]-H_2ase enzyme.[168]

In summary, the deceptive simplicity of this diiron complex belies a range of sophisticated maneuvers that serve to provide a path for the dehydrogenation of amineboranes. An apparent role for bridgehead hydrocarbon substituents that place C-H bonds in close proximity, agostic interactions, with an open site on iron diminishes residence time of the substrate, and hence impedes the dehydrogenation process. On the other hand the amine functionality assists in the process, implicating its positive effect on the heterolytic H_2 release

CHAPTER V

HEMILABILE BRIDGING THIOLATES AS PROTON SHUTTLES IN BIOINSPIRED H_2 PRODUCTION ELECTROCATALYSTS: A CASE STUDY FOR ELECTROCHEMICAL CHARACTERIZATIONS[*]

Introduction

This chapter focuses on the first coordination sphere of [FeFe]- and [NiFe]-H_2ase and features that are common to the active sites found in CO Dehydrogenase and Acetyl CoA Synthase. These site-differentiated catalysts that facilitate organometallic transformations clearly are related to the H_2ases and the model complexes of both have been discussed which incorporate features of all active sites.[41] In particular there is a class of complexes based on N_2S_2 nickel dithiolates that are S-bridged to a second metal center, in many cases iron. These are inspired by the enzymes shown in Figure V-1, in particular the ACS active site.[177] The question we ask is whether we can take features of this site and turn it towards a H_2 producing catalyst similar to the hydrogenases. Our promotion of the importance of metallodithiolates as ligands, particularly evident in the ACS active site, has been widely explored by ourselves and others resulting in a large group of hetero and homobimetallic complexes for H_2 production/oxidation.[178-180] A series of recent reviews gives a sampling of each.[181-183]

---

[*] Adapted with permission from Ding, S.; Ghosh, P.; Lunsford, A. M.; Wang, N.; Bhuvanesh, N.; Hall, M. B.; Darensbourg, M. Y. *J. Am. Chem. Soc.* DOI:10.1021/jacs.6b06461. Copyright **2016** American Chemical Society.[184]

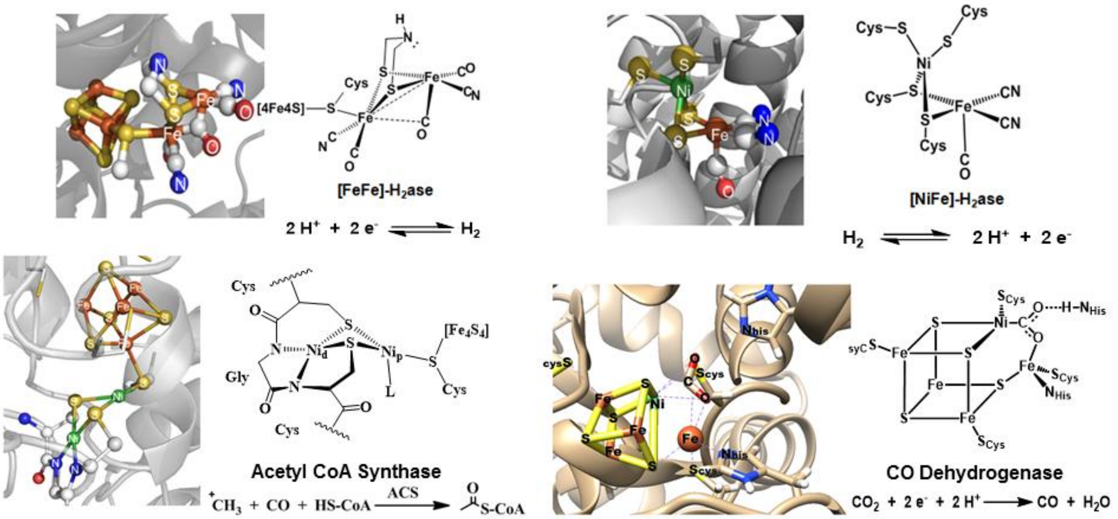

Figure V-1. Active sites of [FeFe]- and [NiFe]-H$_2$ase as well as Acetyl CoA synthase and Carbon Monoxide Dehydrogenase. The relevant catalytic reaction is also shown.

Our efforts in this field have been a combination of synthesis, electrochemical, and computational studies. My role has focused on understanding the electrochemistry of the bimetallic complexes seen in Figure V-3.[184] These biomimetic studies have afforded options to expand our knowledge in all these areas. In this chapter I will describe the electrochemical experiments used to define these systems including cyclic voltammetry and bulk electrolysis.

Overview of Cyclic Voltammetry

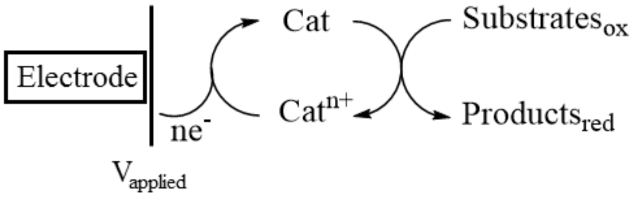

Figure V-2. Illustration of the electron transfer reactions that occur at the working electrode in an electrocatalytic process.

There are two essential requirements for an electrocatalyst to efficiently catalyze a reaction; a) the catalyst must participate in an electron transfer step with the electrode (oxidation or reduction) and b) must then react efficiently with a substrate producing a product, see Figure V-2.[185] Both processes must be fast in order to yield an effective catalyst. The electrocatalyst is optimized by either fine-tuning the coordination sphere around transition metal with ancillary ligands or tuning the ligands themselves through function aided design. The different electrocatalysts can then be screened for redox potentials, electron transfer rates, current efficiencies, and chemical kinetics which can lead to further catalysts optimization.

Cyclic voltammetry is an electrochemical technique in which the voltage applied by a working electrode is ramped linearly in a certain direction from an initial starting point.[186] At a predetermined limit, the voltage is then reversed and scanned in the opposite direction; the current generated during this sweep is plotted as a function of the applied potential. There are three different electrodes required to conduct cyclic voltammetry experiments (as well as bulk electrolysis) and these are the working, counter (or auxiliary), and reference electrode. It is at the working electrode where the electrochemical events are taking place. There are a number of conducting materials that can be used as well as many shapes but some of the most common are platinum, gold, and glassy carbon in a cylinder form. The counter or auxiliary electrode completes the circuit, in conjunction with the working electrode, so that current can either be applied or measured depending on the electrochemical reaction that is occurring. Again, the counter electrode can be made of many different materials, but the one used in these studies is platinum for cyclic voltammetry and NiCr alloy for bulk electrolysis. Finally, the reference electrode provides a means of accurately measuring the potential of a solution by comparing it to a stable, known half-cell potential. This is created by employing a redox system where each participant of the redox reaction is present, in our case a silver wire in contact with a 1 mM Ag^+ solution, and is separated from the bulk cell by a vycor glass frit.

Considerations when Preparing the Electrochemical Cell

Since cyclic voltammetry is a sensitive analytical technique, there are many factors that must be kept in mind in order to obtain the most useful and interpretable voltammograms especially when making comparisons between catalysts. Foremost, the purity of the compound, as well as the solvent used and the electrolyte, must be as high as possible. Any impurity has the possibility of causing extra peaks in the voltammograms which might lead to a misinterpretation of the electrochemical events. Solvents must be anhydrous and free of any possible stabilizers which have the potential to react with the electrochemically generated species in the cell. Water also limits the boundary of the negative potential window due to reduction events.

In order to increase the conductivity of the solution and not provide any residual resistance, an electrolyte is added to the cell which must be of highest purity. The concentration of the electrolyte must be kept constant from one catalyst to the next as well as during the course of the electrochemical experiment, i.e. solvent evaporation should be avoided. A study done by Bond et al. found that the potential at which an electrochemical event occurred ranged from -305 to -540 mV at electrolyte concentrations ranging from 100 mM to 0 mM.[187] Similarly, Pavlishchuk et al. found the concentration of the Ag^+ ion in the reference electrode also shifts the redox potentials by up to 52 mV.[188] Not only should these concentrations be kept constant from one electrochemical experiment to the next, but also a consideration when comparing redox potentials from different publications.

Initially, the electrochemical cell is set up with just the electrolyte and solvent without any added substrate or catalyst to determine if the background is free of any impurities. This allows any resulting peaks upon compound addition to be assigned to redox events of the metal complex and not some other species (unless it is an impurity in the complex itself). Typically, in the cases we have studied, a large event at between -1.0 V and -1.6 V is initially seen which corresponds to the reduction of O_2. Purging the solution for 15 minutes with argon followed by maintaining a constant blanket over the top of the cell should cause this peak to disappear. If there are any other peaks located in the potential window of the solvent, further purification of the electrolyte or the solvent itself may be required. Alternatively, it could be due to impurities on the working electrode which may require further polishing.

There are a few factors that need to be addressed when selecting a solvent to use in the electrochemical experiment, 1) the solubility of the electrocatalyst, 2) the solubility of the substrate, and 3) the potential window under investigation. Each solvent has a specific potential at which it is either oxidized or reduced resulting in a large current enhancement which will overwhelm any redox event of the added catalyst. These potential windows, or solvent windows, can be seen in Table V-1 and should be tailored to the redox potentials of the complexes being studied.[189] For instance, if the metal complex possesses a fairly negative reduction event, DMSO might not be ideal since the solvent is reduced ~-2.3 V. Alternatively, DMF may be a better choice since its reduction event does not occur until -3.2 V. If an unsuitable solvent is selected, important electrochemical events may not be observed.

Table V-1. Optimum potential window for the specified solvent during which there is no significant oxidation or reduction of the solvent.

Solvent	Potential Window
Acetone	-2.6 to +1.0
Acetonitrile	-2.4 to +1.6
Dichloromethane	-2.3 to +1.3
Dimethylformamide	-3.2 to +1.1
Dimethylsulfoxide	-2.3 to +0.6
Tetrahydrofuran	-2.7 to +1.0
Water	-1.2 to +1.0

Cyclic Voltammetry of [NiFe]- and [FeFe]-H_2ase Model Complexes

Compounds that we recently explored are deemed to be models of both [FeFe]- and [NiFe]-H_2ase and while the validity of these models is questionable, they both are redox active and both show capabilities for catalyzing proton reduction.[184] These complexes will be used as a case study. With all the considerations raised above, the cyclic voltammograms of BF_4^- salts of **Fe-Fe'**$^+$, Figure V-3a, and **Ni-Fe'**$^+$, Figure V-3b, were recorded at 22° C under Ar. All voltammograms are referenced to internal $Fc^{0/+}$ at $E_{1/2}$ = 0.0 V. Electrochemical scans should be initiated at the rest potential, i.e. not during an electrochemical event, and should start with the complex in its native state. This is typically around 0.0 V but can shift if there exists redox events at low potentials. The scans shown in Figure # were initiated at -0.5 V due to the low oxidation potential of the CpFe unit which would overlap with the beginning of the scan if it was initiated at 0.0 V.

On initiating the electrochemical scan in the cathodic direction, two reduction events, and, upon reversal, two oxidation events were observed for both complexes within the MeCN solvent window. The initial reductive event, at -1.64 V in the case of the **Ni-Fe'⁺**, is assigned to the $Ni^{II/I}$ couple; its irreversibility is addressed below. In contrast, for the **Fe-Fe'⁺** complex, the first reduction is quasi-reversible and at a more positive position, -1.19 V; it is assigned to the $\{Fe(NO)^{7/8}$ redox couple. In both cases, the first observed or more positive reduction event is anodically shifted compared to the MN_2S_2 (free metalloligand) precursors, thus illustrating the electron-withdrawing nature of the $[CpFe'(CO)]^+$ unit and its ability to modulate redox events on the MN_2S_2 unit. The second, more negative, irreversible reduction event in the **Fe-Fe'⁺** complex is assigned to the $Fe'^{II/I}$ couple in the $[CpFe'(CO)]^+$ unit, Figure V-3a. For the **Ni-Fe'⁺** complex, assignment of the more negative event is not straight-forward due to the irreversibility of the previous redox event; computational studies indicate an intramolecular Ni^I to Fe^{II} electron transfer concomitant with structural rearrangement accounts for this irreversible behavior, Figure V-3b.

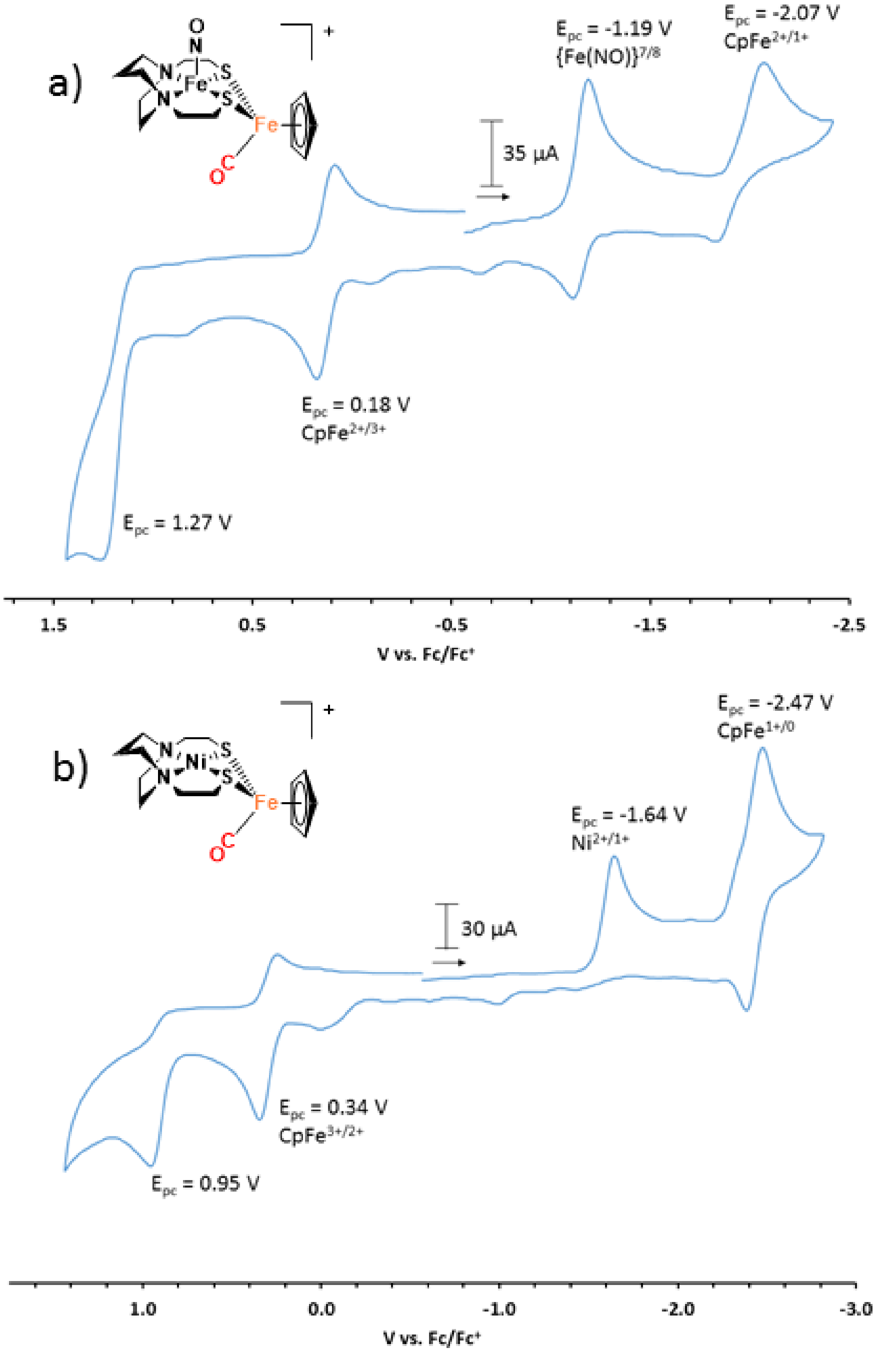

Figure V-3. Full scan of a) **Fe-Fe'$^+$** and b) **Ni-Fe'$^+$** at a scan rate of 200 mV/s initiating the scan in the negative direction in MeCN referenced to internal Fc/Fc$^+$ = 0.

The terms reversibility, quasi-reversibility, and irreversibility are determined based on the amplitude of the current response in the initial scan compared to the reverse scan, $\frac{i_{pc}}{i_{pa}}$, and relate to the stability of the electrochemically generated species.[186] If the current amplitude is equal in both directions, the generated species is stable on the time scale of the electrochemical scan and can be said to be reversible, i.e. $\frac{i_{pc}}{i_{pa}} = 1$. When the amplitude of the return wave is less than that of the initial wave, the event is said to be quasi-reversible or $0 < \frac{i_{pc}}{i_{pa}} < 1$. Finally, if there is some structural rearrangement or decomposition of the electrochemically generated species, there will typically be no return wave and is said to be irreversible or $\frac{i_{pc}}{i_{pa}} = 0$.

An important electrochemical experiment that is commonly skipped is to initiate the scan in varying directions while reversing the scan after each electrochemical event, see Figure V-4. It is then possible to probe the reversibility of each event instead of encompassing all oxidation, or all reduction events simultaneously. While the initial reduction of **Fe-Fe'**$^{+}$ at -1.19 V is described as quasi-reversible in Figure V-4a and Figure V-4d, by reversing the scan after the reduction event and not continuing the scan to the second reduction, it can be seen that the event is actually completely reversible in Figure V-4c. This is important for the proper assignment of the reversibility of each peak and the assignment of small bumps in the cyclic voltammograms which might arise from decomposition products. An example of this can be seen in Figure V-4a where a possible electrochemical event at -0.6 V which is not present in Figure V-4b when the scan is reversed after the first oxidation event. In the absence of scan reversals, this discrepancy may have resulted in an improper assignment of redox events.

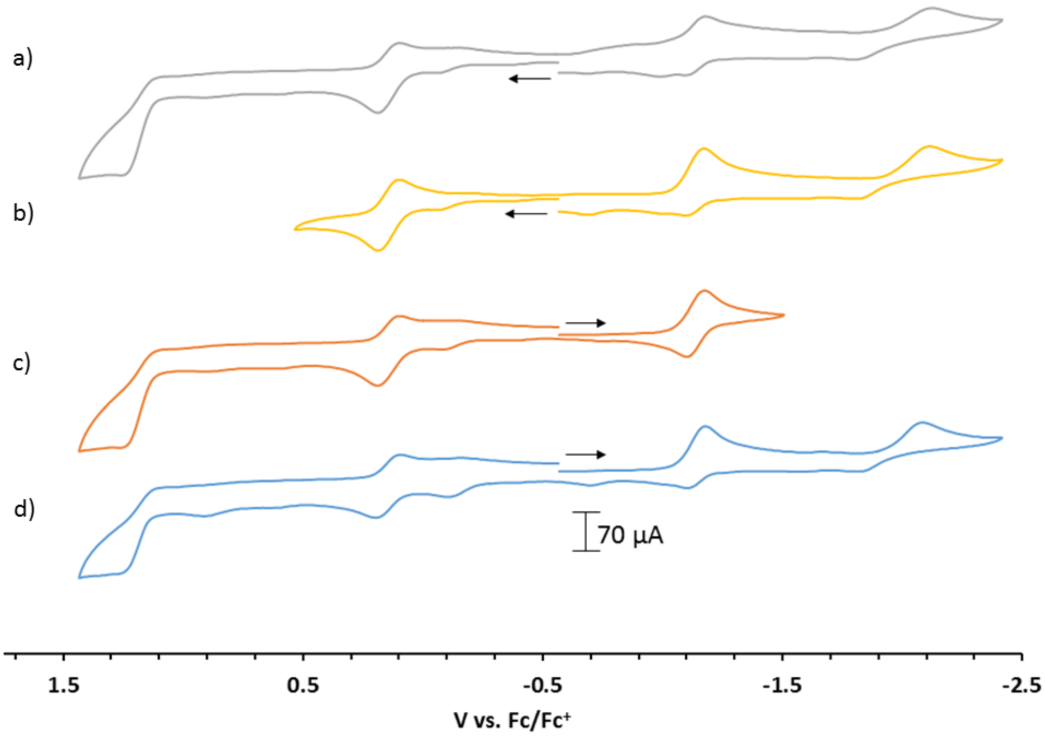

Figure V-4. Cyclic voltammograms of **Fe-Fe'**$^{+}$ isolating each redox event and initiating the scan in different directions.

Hydrogen Production Assays

Once the redox behavior of the potential catalyst is established, the hydrogen production possibilities can then be explored. This is done by adding aliquots of a substrate, in this case protons, and observing the change in the cyclic voltammograms.[32,190-192] There are a few possibilities as to how the voltammograms might change that would indicate a reaction with protons and the possible electrocatalytic production of hydrogen. Confirmation through bulk electrolysis should be done to confirm this event is in fact due to the production of H_2, vide infra.

There are two concerns to be addressed which arose in this studies; 1) electrode fouling and 2) homoconjugation of the added acid. Due to electrode fouling, the glassy carbon working electrode was polished after every scan or added equivalent of acid.[193] If the electrode was not polished, two things happened, either the current density dropped between the scans or the peak shifted to a more positive position. Therefore, to obtain reproducible results the glassy carbon working electrode was polished whenever a scan was saved. When trifluoroacetic acid is used as the substrate, effects due to homoconjugation must be taken into effect especially when calculating the overpotential.[194,195] Homoconjugation is a phenomenon in which the conjugate base is stabilized by hydrogen bonding to the acid resulting in an increasing acidity at higher concentrations. If the effects of homoconjugation are not taken into account when determining the overpotential the reported number could be off by ~60 mV when trifluoroacetic acid is used.

The first example is seen in Figure V-5A where upon adding acid, a large increase in the current response directly at a reduction event occurs. This current response reflects the dynamic processes shown in Figure V-2 where ne^- are transferred to the catalyst which are then transferred to the substrate allowing more e^- to be transferred resulting in an increased current response. If there are multiple reduction events, current increase might occur at either one and might be dependent on the pKa of the added acid. This is the most common type of voltammogram change among proton reduction electrocatalysts.[31-33,178,190,191,196-198] Figure V-5B displays a second example of current enhancement where after a certain amount of acid is added a new peak appears which continues to increase with additional equivalents. While this type of change is less common among proton reduction catalysts, it still provides insight into the plausible mechanisms. This implies that after reduction of the initial catalyst, the new complex reacts with the proton source, followed by reduction of this newly formed species which then acts as the proton reduction catalyst. Cyclic voltammetry is a useful technique for deciphering potential reduction mechanisms especially when coupled with DFT calculations.

Addition of trifluoroacetic acid (TFA) to the electrochemical cell containing **Ni-Fe'$^+$** or **Fe-Fe'$^+$** increases the current of the initial reduction events at -1.64 V and -1.19 V, respectively. For the **Ni-Fe'$^+$** complex, this current continues to increase with additional equivalents of TFA, Figure V-5A, while for the **Fe-Fe'$^+$** complex the initial reduction event's current is saturated after addition of 12 equiv. of TFA, Figure #B. For the **Fe-Fe'$^+$** complex, greater than 6 equiv. of TFA results in a new peak at -1.66 V and its intensity increases with additional equiv. of TFA. An overlay of both complexes after addition of 50 equiv. of TFA as well as TFA in the absence of either catalyst is displayed in Figure V-5C. The large current enhancements were attributed to the catalytic production of H_2, which was quantified by bulk electrolysis studies described below.

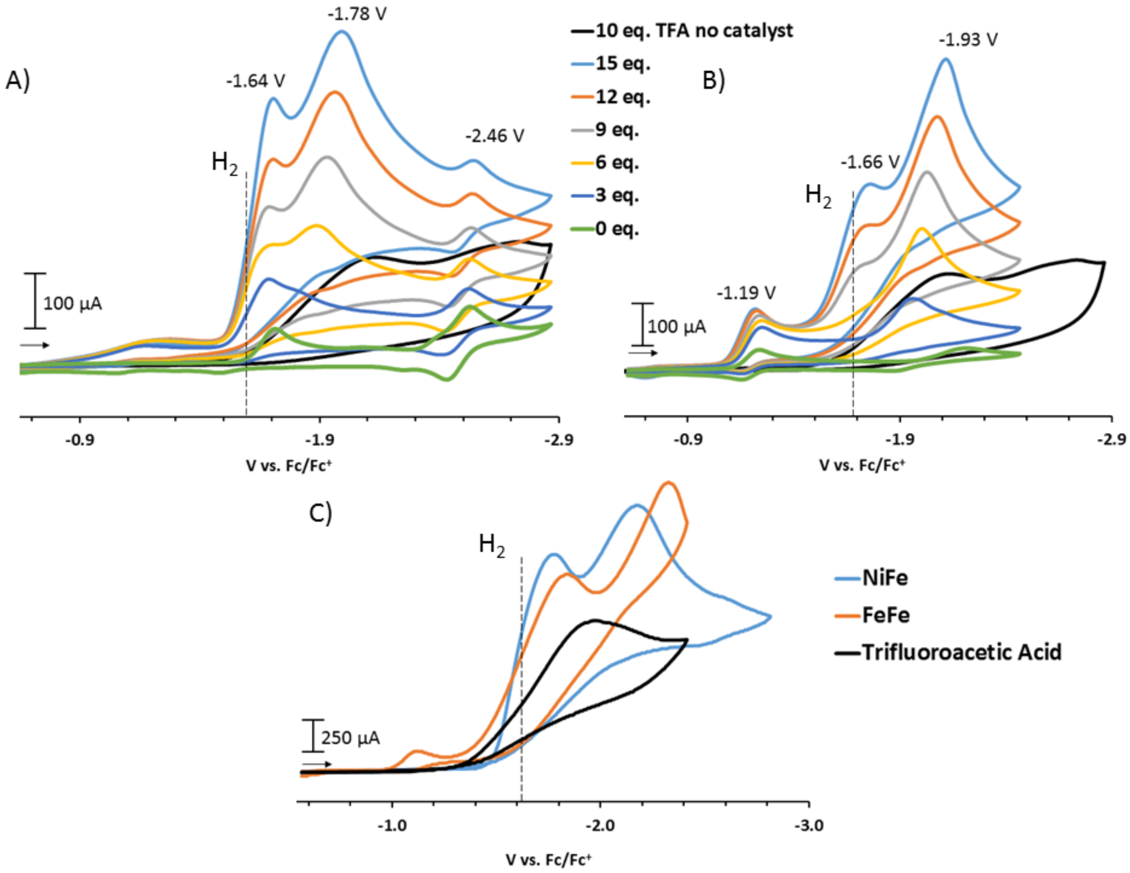

Figure V-5. CV of 2 mM A) **Ni-Fe'$^+$** and B) **Fe-Fe'$^+$** under Ar in CH_3CN solutions containing 0.1 M $[^tBu_4N][PF_6]$ as supporting electrolyte with addition of equivalents of trifluoroacetic acid. C) An overlay of **Ni-Fe'$^+$** and **Fe-Fe'$^+$** in the presence of 50 equivalents of TFA as well as 50 equivalents of TFA in the absence of either catalyst. The dotted line denotes the potential applied during bulk electrolysis, -1.56 V.

Calculation of Overpotential

There are two ways we can rank a series of catalysts and make comparisons between complexes; a) the overpotential at which catalysis occurs, and b) the speed at which the catalyst operates, i.e. the TOF. Overpotential is defined as the "additional potential (beyond the thermodynamic requirement) needed to drive a reaction at a certain rate". A lower overpotential is more desired and can be calculated using Eq. V-1.[195,199]

$$\text{overpotential} = |E_{H+} - E_{cat/2}| \qquad \text{(Eq. V-1)}$$

In our experiment, E_{H+} is equal to the thermodynamic potential for hydrogen production from trifluoroacetic acid with the effects of homoconjugation taken into account. For 0.1 M trifluoroacetic acid in MeCN referenced to Fc/Fc^+, this value is -0.65 V. $E_{cat/2}$ is the applied potential at which the catalytic current (i_{cat}) is half of its maximum value. The overpotential for both complexes was measured in the presence of 0.1 M trifluoroacetic acid (50 eq.) and was determined as described by Appel and Helm.[6] An example for **Ni-Fe'⁺** complex is shown in Figure V-6. Using this method, overpotentials of 938 mV and 942 mV for the **Fe-Fe'⁺** and **Ni-Fe'⁺** complexes respectively, were obtained. While these numbers may seem high, it is typical for first row transition metal catalysts to have overpotentials in excess of 700 mV.[190-192,196]

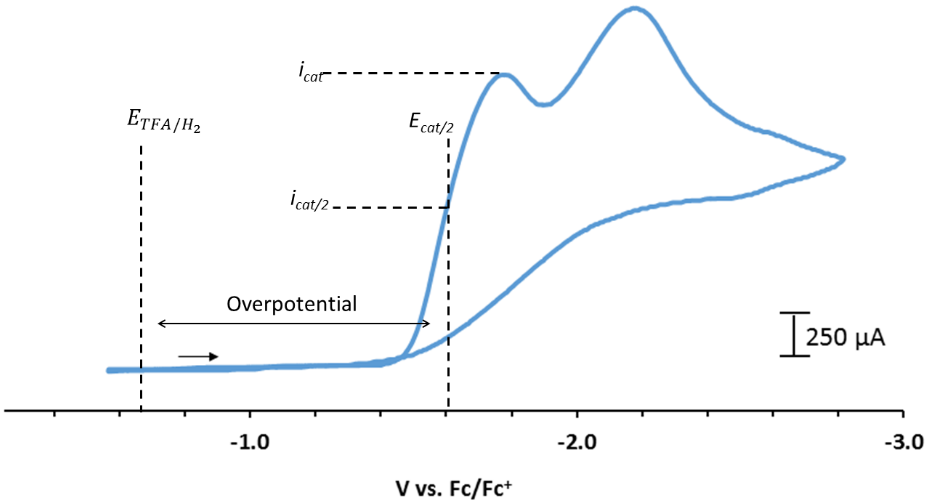

Figure V-6. Cyclic voltammogram of 2 mM **Ni-Fe’$^+$** in the presence of 0.1 M TFA in MeCN at a scan rate of 200 mV/s. This illustrates how to calculate $E_{cat/2}$ for the determination of the overpotential for electrocatalysis.

Calculation of Turnover Frequency

Turnover frequency (TOF) is the second parameter that can be used to rank catalysts and was calculated for both complexes using Eq V-2 with a correction for background acid.[190]

$$\mathrm{TOF} = 1.94 \times v \times \left(\frac{i_{cat} - i_{acid}}{i_p}\right)^2 \qquad \text{(Eq. V-2)}$$

v = Scan Rate

i_{cat} = measured current with added acid

i_{acid} = measured current of acid by itself at the potential of i_{cat}

i_p = measured current of catalyst without acid

Due to the overlap of the current density of the acid without the catalyst with the current density of the acid with the catalyst, the normally used $\frac{i_{cat}}{i_p}$ was corrected as shown in Eq. V-2 and Figure V-7. The concentration of acid was systematically increased until the calculated TOF remained constant as shown in Table V-2 and Figure V-8 for **Fe-Fe'$^+$** and Table V-3 and Figure V-9 for **Ni-Fe'$^+$**.

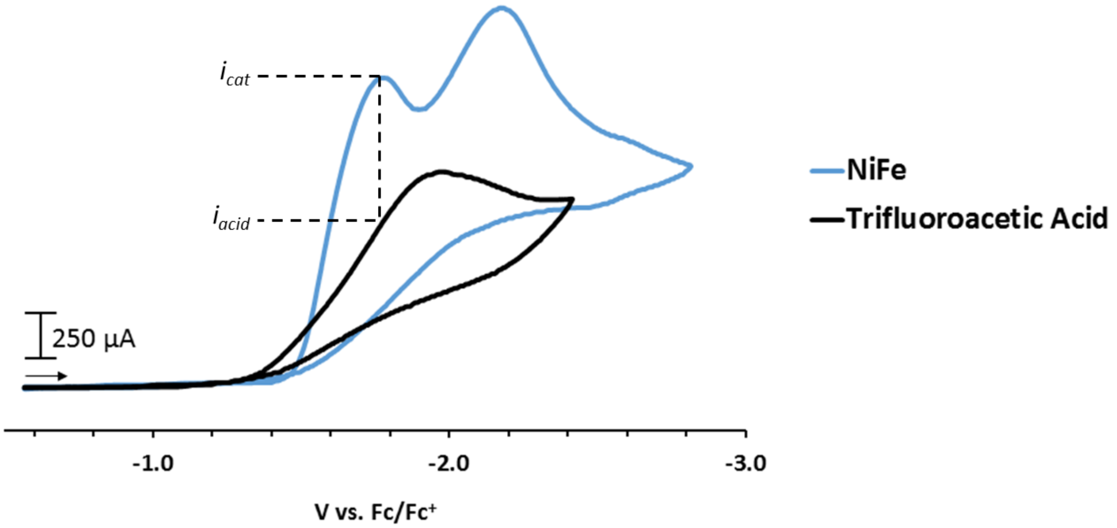

Figure V-7. Cyclic voltammograms of 2 mM **Ni-Fe'$^+$** in the presence of 0.1 M TFA in MeCN at a scan rate of 200 mV/s (blue trace) and 0.1 M TFA without the catalyst (black trace). This illustrates how to calculate $E_{cat/2}$ for the determination of the overpotential.

From the CV experiments, turnover frequencies (TOFs) of 69 s^{-1} and 52 s^{-1} (experimental barriers: 14.9 and 15.1 kcal/mol at 298.15 K by Eyring equation) were calculated for the **Fe-Fe'$^+$** and **Ni-Fe'$^+$** complexes, respectively. The H/D kinetic isotope effects on **Fe-Fe'$^+$** and **Ni-Fe'$^+$** turnover frequencies (k_H/k_D) were determined to be 1.46

and 1.56, respectively.[200,201] See Table V-2 and Table V-3 for the calculated TOFs using d_1-TFA. While k_H/k_D isotope effects are known to vary widely, these relatively low ratios are consistent with the likely involvement of metal-hydride species in the catalytic cycles.

Table V-2. Values used for the calculation of TOF for **Fe-Fe'$^+$** at various TFA concentrations in MeCN at a scan rate of 200 mV/s. Due to the appearance of the catalytic peak at -1.66 V, the value for i_p with no added acid was taken from the first reduction at -1.19 V. The kinetic isotope effect (KIE) was measured using 150 uL d_1-TFA and the TOF calculated in a similar fashion.

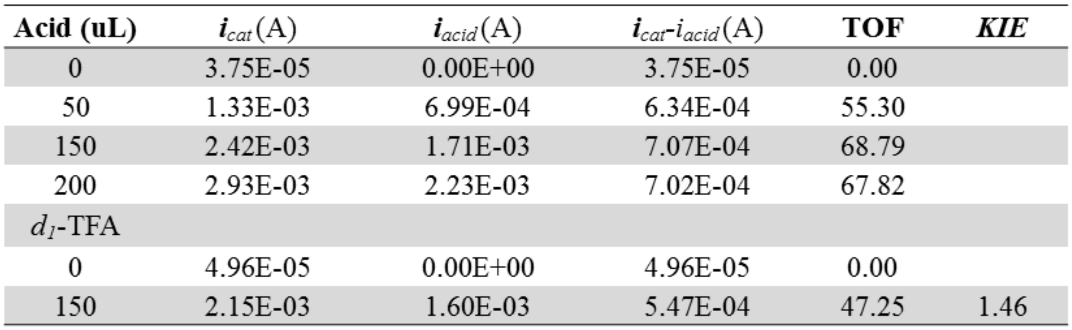

Acid (uL)	i_{cat} (A)	i_{acid} (A)	i_{cat}-i_{acid} (A)	TOF	*KIE*
0	3.75E-05	0.00E+00	3.75E-05	0.00	
50	1.33E-03	6.99E-04	6.34E-04	55.30	
150	2.42E-03	1.71E-03	7.07E-04	68.79	
200	2.93E-03	2.23E-03	7.02E-04	67.82	
d_1-TFA					
0	4.96E-05	0.00E+00	4.96E-05	0.00	
150	2.15E-03	1.60E-03	5.47E-04	47.25	1.46

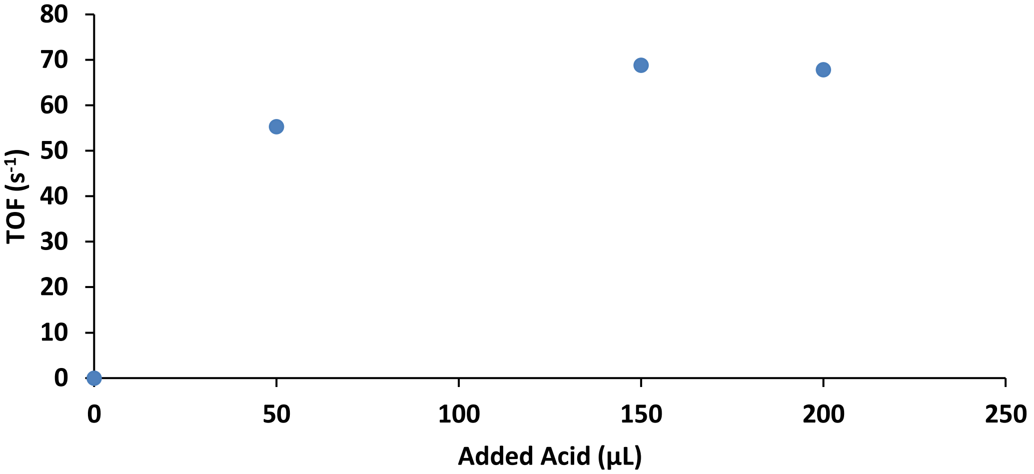

Figure V-8. Plot of added TFA vs. TOF calculated using the values in Table V-2 for **Fe-Fe'$^+$**.

Table V-3. Values used for the calculation of TOF for **Ni-Fe'$^+$** at various TFA concentrations in MeCN at a scan rate of 200 mV/s. The kinetic isotope effect (KIE) was measured using 200 ul d_1-TFA and the TOF calculated in a similar fashion.

Acid (uL)	i_{cat} (A)	i_{acid} (A)	i_{cat}-i_{acid} (A)	**TOF**	**KIE**
0	5.58E-05	0.00E+00	5.58E-05	0.00	
50	9.90E-04	4.54E-04	5.37E-04	35.85	
100	1.63E-03	1.00E-03	6.29E-04	49.35	
150	2.15E-03	1.52E-03	6.38E-04	50.70	
200	2.64E-03	1.99E-03	6.43E-04	51.43	
250	3.12E-03	2.47E-03	6.48E-04	52.24	
d_1-TFA					
0	5.94E-05	0.00E+00	5.94E-05	0.00	
200	2.48E-03	1.93E-03	5.50E-04	33.25	1.56

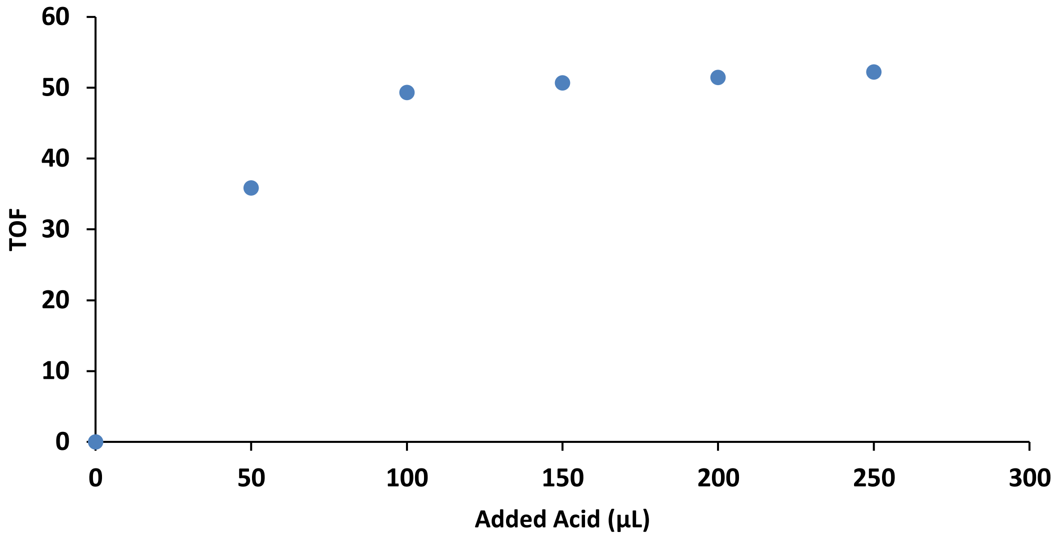

Figure V-9. Plot of added TFA vs. TOF calculated using the values in Table V-3 for **Ni-Fe'$^{+}$.**

Bulk Electrolysis

Bulk electrolysis is required in order to confirm that the current enhancements on addition of H^+ to presumed electrocatalysts, as seen in the cyclic voltammograms, corresponds to H_2 production. This experiment involves holding a constant potential, and measuring the current passed from the working electrode to the counter electrode over the course of a set time and in the presence of a large excess of substrate. After a certain time has passed, the bulk solution or headspace of the cell is analyzed and quantified for the products of the catalyzed reaction. Since the number of electrons passed through solution (charge) is known, and the products quantified, a faradaic efficiency, or the number of electrons used for the desired reaction, can be calculated. Ideally, 100% of the electrons passed through solution will be processed by the catalyst and used for H_2 production, although side reactions as well as catalyst decomposition can be competing for those electrons.

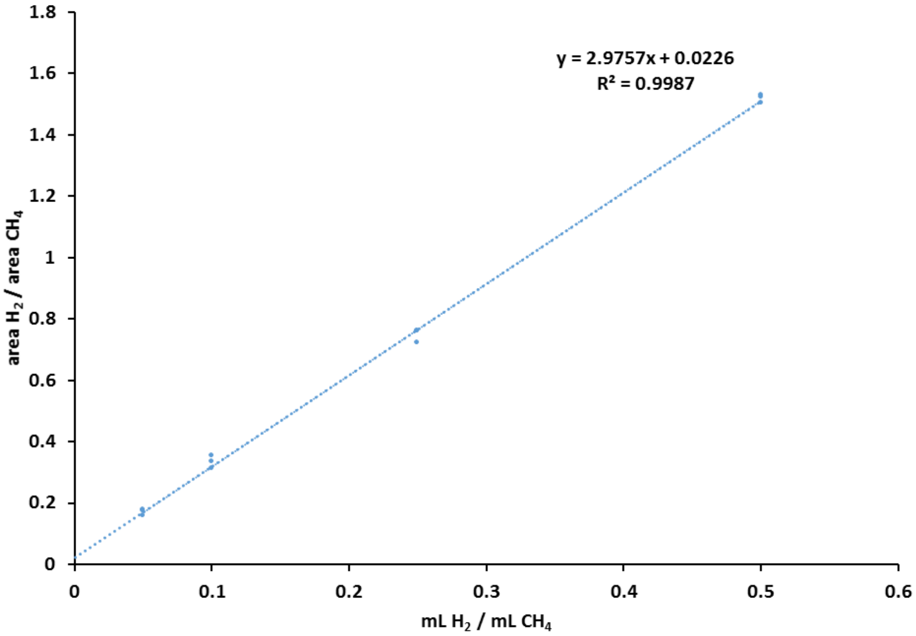

Figure V-10. Calibration curve used in the quantification of H_2 produced during electrolysis. This was generated by preparing vials containing varying amounts of H_2 with one mL of CH_4 and plotting the $\frac{area\ of\ H_2}{area\ of\ CH_4}$ vs. $\frac{mL\ of\ H_2}{mL\ of\ CH_4}$.

Before bulk electrolysis can be done, a way of quantifying the final products formed must be established. For H_2, gas identification and quantification was accomplished with an Agilent Trace 1300 GC equipped with a thermal conductivity detector and a custom-made 120 cm stainless steel column packed with Carbosieve-II from Sigma-Aldrich. The carrier gas was Ar, and throughout the entire separation, the column was kept at 200 °C, while the detector was at 250 °C. A calibration curve, Figure

#, was generated by determining the relative response factor of H_2 and the internal standard, CH_4, in a degassed vial with Ar. Various volumes of H_2 were injected as well as 1 mL of CH_4 into the vial and the chromatogram taken. A plot of $\frac{area\ of\ H_2}{area\ of\ CH_4}$ vs. $\frac{mL\ of\ H_2}{mL\ of\ CH_4}$ was generated as a calibration plot and used for the quantification of H_2 in the experiment. This was done by injecting 1 mL of CH_4 into the bulk electrolysis cell and then sampling the headspace and analyzing by gas chromatography. By using CH_4 as an internal standard, the calibration curve can be used for any volume cell.

To test the calibration curve for reproducibility and to ensure the electrolysis setup is functioning correctly and is airtight, bulk electrolysis was performed at -1.56 V on 0.1 M TFA in MeCN for 30 minutes. Three separate runs were conducted and the final charge passed over the course of the experiment as well as the faradaic efficiency can be seen in Table V-4. This has several implications: 1) the experimental setup is airtight and works properly; 2) the calibration curve is both precise and accurate; and 3) there exists background H_2 production at this potential that must be subtracted from the overall H_2 produced in the presence of catalyst.

Table V-4. Coulombs passed and Faradaic efficiency from the bulk electrolysis of 50 equivalents of trifluoroacetic acid in MeCN at -1.56 V for 30 minutes.

Run	Coulombs Passed (C)	Faradaic Efficiency
1	1.43	0.9723
2	1.41	0.9692
3	1.59	0.9847
Average	1.47 ± 0.08	97.54 ± 0.67%

The headspace of the bulk electrolysis setup was analyzed for H_2 using gas chromatography after applying a constant potential at -1.56 V (dotted line in Figure V-5) for 30 minutes in the presence of catalyst and 50 equivalents of TFA. Due to the overlap of the background TFA peak and the catalytic peaks in the cyclic voltammogram, the H_2 evolving from the acid itself must be deducted, Table V-5. An example of a plot of Coulombs passed vs. time for the **Fe-Fe'$^+$** can be seen in Figure V-11.

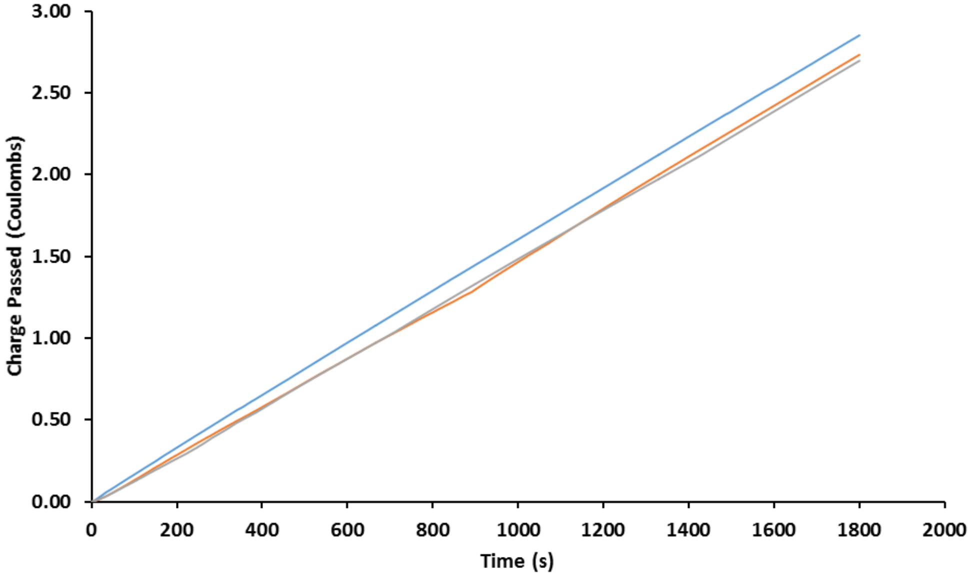

Figure V-11. Coulombs passed vs. time for the bulk electrolysis of 50 equivalents of trifluoroacetic acid in the presence of **Fe-Fe'$^+$** in MeCN at -1.56 V for 30 minutes.

All values obtained are an average of three separate bulk electrolysis experiments. After 30 min of electrolysis with the **Ni-Fe'$^+$** catalyst, 0.98 ± 0.04 Coulombs (after acid subtraction) was passed through the solution resulting in a turn-over-number (TON) of 0.26 ± 0.01 with a Faradaic efficiency of 96.0 ± 2.9 % for H_2 production, Table V-5.

Similarly in the presence of the **Fe-Fe'⁺** catalyst, passage of 1.29 ± 0.06 Coulombs through the solution gave a TON of 0.33 ± 0.02 with a Faradaic efficiency of 77.2 ± 7.9 % for H_2, Table V-5. These results confirm that the current enhancement in the cyclic voltammogram is in fact due to the reduction of protons to H_2 by the **Ni-Fe'⁺** and **Fe-Fe'⁺** catalysts in the presence of TFA.

Table V-5. Coulombs passed and faradaic efficiency from the bulk electrolysis of 50 equivalents of trifluoroacetic acid in the presence of **Ni-Fe'⁺** or **Fe-Fe'⁺** in MeCN at -1.56 V for 30 minutes.

Run	Coulombs Passed (C)	Corrected Coulombs Passed (C)	TON	Faradaic Efficiency
Ni-Fe'⁺				
1	2.5	1.03	0.27	99.34%
2	2.4	0.93	0.24	96.38%
3	2.48	1.01	0.26	92.19%
Average	2.46 ± 0.044	0.98 ± 0.044	0.26 ± 0.01	95.97 ± 2.93%
Fe-Fe'⁺				
1	2.85	1.38	0.35	66.75%
2	2.74	1.27	0.33	85.77%
3	2.7	1.23	0.31	79.25%
Average	2.76 ± 0.066	1.291 ± 0.066	0.33 ± 0.02	77.25 ± 7.89%

Conclusions and What Makes a Good Catalyst?

With all of these numbers in hand, the next step is to compare them to previously reported complexes as well as the protein itself. As discussed above there are three important factors when ranking catalysts, 1) Faradaic efficiency, 2) TOF, and 3) overpotential. Ideally, the catalyst would have a high Faradaic efficiency and TOF with an overpotential close to 0.0 V. This is seen in the [FeFe]-H_2ase enzyme which has a TOF around 9000 s^{-1} with an overpotential ~100 mV and is the gold standard for molecular catalysts.[41]

The first catalyst to surpass the TOF of the natural [FeFe]-H_2ase enzyme by an order of magnitude and the gold standard for future studies was synthesized at PNNLin development of the Dubois NiP_2N_2 system, and consisted of a Ni(II) center featuring two P_2N ligands.[196] Nitrogen bases were positioned above the open sites on the nickel and model the adt dithiolate linker in the [FeFe]-H_2ase enzyme. TOFs of 106,000 s^{-1} were reported with an overpotential of ~625 mV. While these numbers are very good, the catalyst suffered from very poor stability under the extremely acidic conditions. Nevertheless, this has provided great insight into what is required to make an efficient and fast H_2-producing catalyst even if the stability is low and the overpotential is higher.

While our catalyst is several orders of magnitude behind the rates of the natural enzyme and the Dubois paradigm for homogeneous catalysts, this is just the beginning of our development process. The first step is to understand how the catalyst operates and what are the procedures used to analyze for overpotential, Fardaic efficiency, and TOF. Now that these are known, further catalyst design will hopefully lead to better catalysts.

CHAPTER VI

A NEW CLASS OF HETEROBIMETALLIC COMPLEXES FOR ELECTROCATALYTIC CO_2 REDUCTION

Introduction

Due to the stability of CO_2, the activation of this deceptively simple molecule has presented chemists with a challenging problem. Ideally, CO_2 reduction might be connected to "solar" electrons and converted to liquid fuels, such as methanol, creating a carbon-neutral system since the ultimate byproduct of fossil fuel combustion is CO_2. The high activation energy required for CO_2 conversion arises from the large reorganizational energy associated with forming the bent radical anion upon reduction of the linear neutral species. This process becomes more favorable if proton-coupled electron transfer occurs simultaneously. Equations VI-1 through VI-6 express this point as well as possible reduction products of CO_2.[185,202] The E^0 values listed are referenced to NHE at pH 7 in aqueous solution at 25°C, 1 atm gas pressure and 1 M proton source. An alternative to the conversion of CO_2 into liquid fuels is to store electrical energy in chemical bonds similar to the H_2 systems described in the introduction.

$$CO_2 + 2H^+ + 2e^- \longrightarrow CO + H_2O \quad E^0 = -0.53\ V \tag{Eq. VI - 1}$$

$$CO_2 + 2H^+ + 2e^- \longrightarrow HCO_2H \quad E^0 = -0.61\ V \tag{Eq. VI - 2}$$

$$CO_2 + 4H^+ + 4e^- \longrightarrow HCHO + H_2O \quad E^0 = -0.48\ V \tag{Eq. VI - 3}$$

$$CO_2 + 6H^+ + 6e^- \longrightarrow CH_3OH + H_2O \quad E^0 = -0.38\ V \tag{Eq. VI - 4}$$

$$CO_2 + 8H^+ + 8e^- \longrightarrow CH_4 + 2H_2O \quad E^0 = -0.24\ V \tag{Eq. VI - 5}$$

$$CO_2 + e^- \longrightarrow CO_2^{\bullet -} \quad E^0 = -1.90\ V \tag{Eq. VI - 6}$$

There exists two transformations of CO_2 in nature relevant to the reactions shown in Eq. VI-1 through VI-6 and these are the reversible reduction of CO_2 to CO and formate. In nature these processes are catalyzed by the CO-dehydrogenase and formate-dehydrogenase enzymes, respectively.[177,203] Two different CO dehydrogenase enzymes exist, but the [NiFe]-CO dehydrogenase is more relevant to our study. Its structure was presented earlier in Figure V-1 and shows the [NiFe] form of CODH with CO_2 bound. In order to overcome the high barrier for CO_2 transformation, two metal centers are used to bind and activate CO_2 forming a Ni-C bond and an Fe-O bond. This cooperativity between the two metals is reminiscent of a frustrated Lewis acid/base pair and is similar to that seen in the hydrogenase enzymes between the pendant base and the metal center for H_2 activation/proton reduction.[41] We are also reminded that sulfurs bridging two metal centers are important design features in biology.

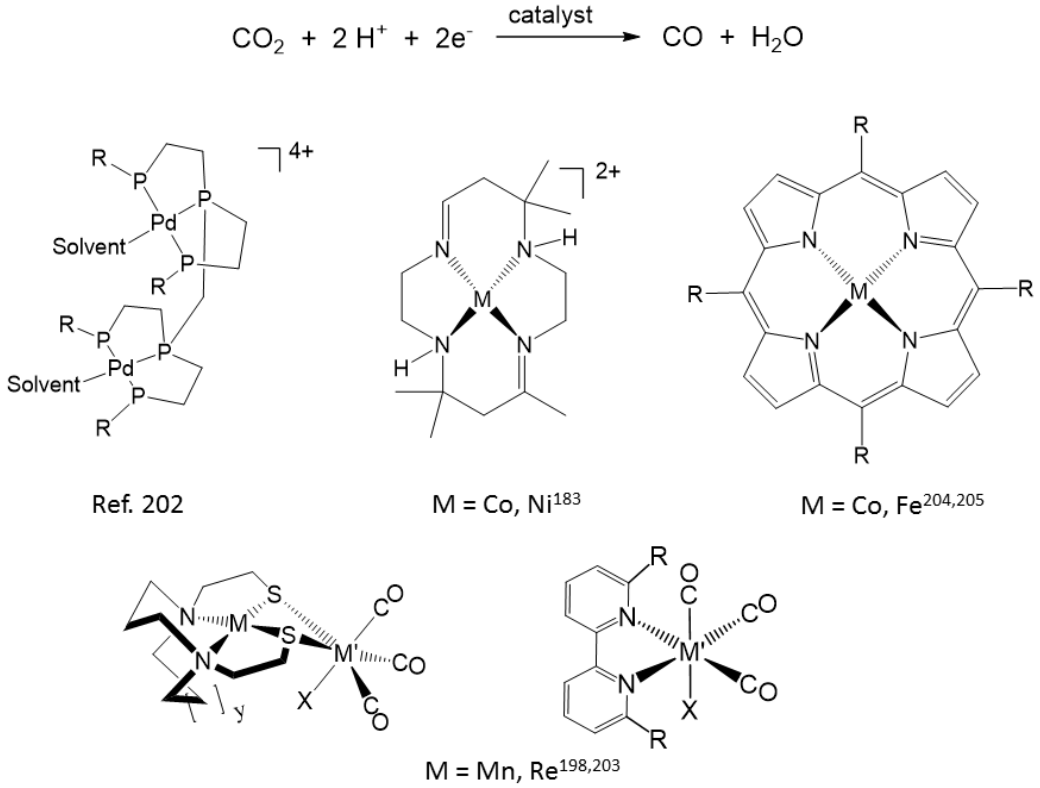

Figure VI-1. Molecular catalysts studied for the reaction shown, namely the two electron and two proton reduction of CO_2 to CO and H_2O.

Transition metal catalysts have been developed over the last four decades to facilitate the electro/photocatalytic reduction of CO_2 to CO which can be used as a C-1 feed stock or for further reduction to produce alternative liquid fuels.[185,200,204-207] Many of these examples can be seen in Figure VI-1. Much of the early work was carried out with metal complexes featuring macrocyclic ligands such as the cyclam and porphyrin units. Recently, one of the most studied systems involves the electrocatalytic reduction utilizing the M(bpy)$(CO)_3$X catalyst where M = Re, Mn and X = Cl, Br.[185] The Re(bpy)$(CO)_3$Cl was shown to be more selective for CO production over H_2, be more stable, and have higher rates than previous generation catalysts. Bourrez et al. showed in 2011 that when Re is substituted for the more abundant Mn, CO_2 can be reduced at even lower overpotentials while exhibiting similar properties to the Re systems in terms of selectivities and rates.[208] Kubiak et al. modified the bipyridine ligand in order to probe the effects of various steric and electronic factors on CO_2 reduction to CO and formate.[209,210] By introduction of sterically bulky t-butyl or mesityl groups in the bipyridine backbone, catalytically active species were stabilized. This has not only increased the stability of the transition metal catalyst and increased the catalytic rate, but also permitted the characterization of possible intermediates in the catalytic cycle using X-ray crystallography and spectroelectrochemistry.[209]

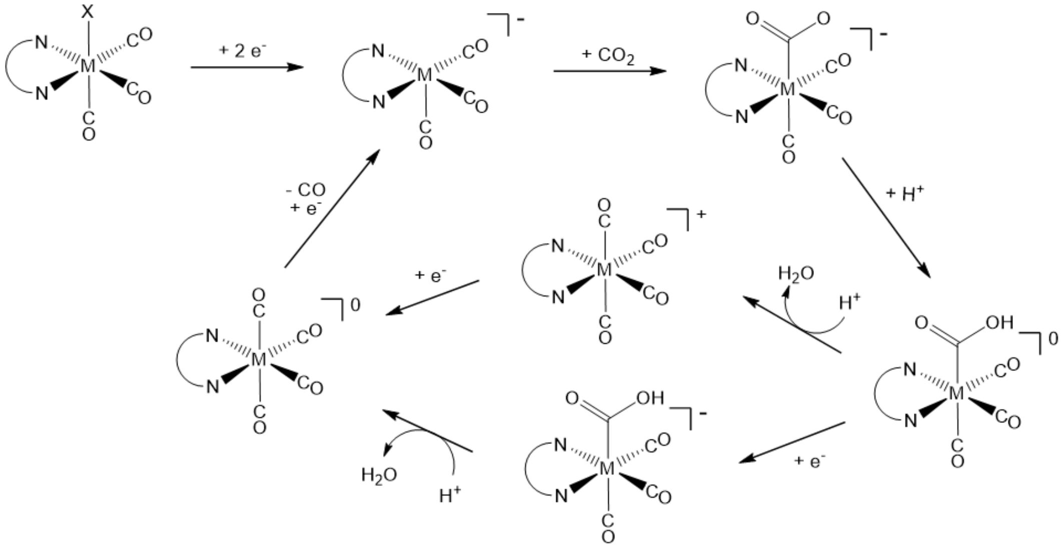

Figure VI-2. Proposed mechanism, supported by DFT calculations and spectroelectrochemistry, for the reduction of CO_2 using Mn(bipy)$(CO)_3$Br and Re(bipy)$(CO)_3$Cl as a homogenous catalyst.[211,212]

The mechanism of CO_2 reduction by the Mn/Re(bpy)$(CO)_3$X catalysts is shown in Figure VI-2 as inferred by spectroelectrochemistry and supported by DFT computations.[211-214] Halide dissociation occurs after a two-electron reduction of the initial complex to generate the catalytically active species. This highly reduced intermediate has been crystallized and fully characterized in the solid state by X-ray crystallography. The CO_2 then binds to the generated open site, followed by protonation of the M-CO_2 adduct. There are then two possibilities regarding the order of the protonation and reduction steps depending on whether the metal center is Re or Mn. Manganese actually has the ability to traverse both pathways depending on the applied electrochemical potential, whereas Re is restricted to the reduction first pathway due to the higher overpotentials needed to drive catalysis.

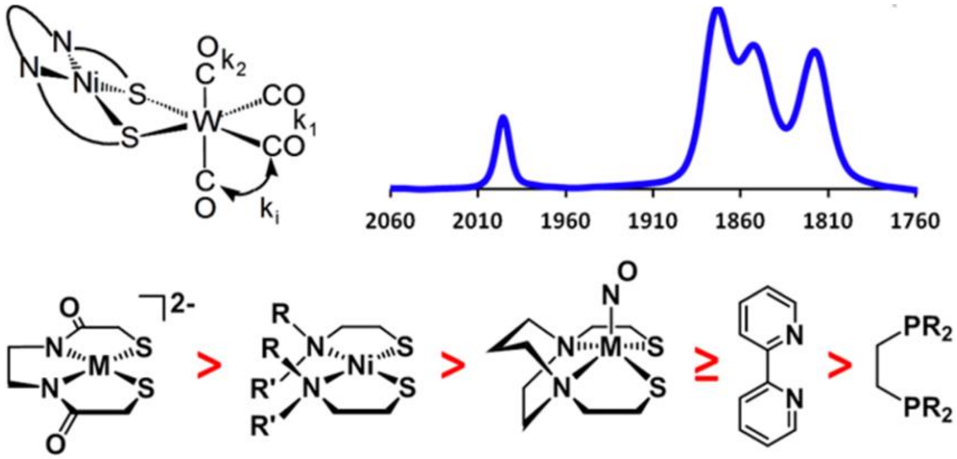

Figure VI-3. Ranking of the electron donating ability of MN_2S_2 metalloligands compared to the traditional bipyridine and diphosphine ligands. This was developed by comparing the ν(CO) absorbance of the appropriate $W(CO)_4$ adduct as shown. Reprinted with permission from Denny, J. A.; Darensbourg, M. Y. *Chem. Rev.* **2015**, *115*, 5248.[181] Copyright **2015** American Chemical Society.

Our approach to accomplishing two electron transformations of small molecules has been to utilize two metal centers which can communicate through bridging thiolates.[181,215] This type of system is modeled after both [FeFe]- and [NiFe]-H_2ase and has shown promise towards proton reduction using both iron and nickel containing bimetallic complexes.[184] Previous bimetallics synthesized using metallodithiolates has revealed the lone pairs of the sulfur atoms bind in a similar fashion to the planar bipyridine ligand, seen in the structure overlay to the right, but with a greater σ-donating ability, as is evident in Figure VI-3.[181] Specifically, we have used the d^8 Ni, $\{Fe(NO)\}^7$, and $\{Co(NO)\}^8$ metal units in MN_2S_2 complexes. There are a variety of diazacycles to which we can attach the dithiolate arms, the most popular being diazacyclooctane (daco) and diazacycloheptane (dach). In this study we will use the dach backbone with bismercaptoethyl thiolate arms resulting in S-M-S angles of 95.42° (7), 94.91° (3), and 96.4° (1) for M = Ni, Fe(NO), and Co(NO) as free metallodithiolate ligands, respectively.[101,102] Hence we have applied this MN_2S_2 methodology to metals which are known to take up CO_2, namely the $Mn/Re(CO)_3X$ unit. Over the course of this study, the six complexes were investigated for electronic communication between the metal centers using both EPR spectroscopy and cyclic voltammetry. The latter indicated an ability to reduce CO_2, similar to the parent bipy complexes.

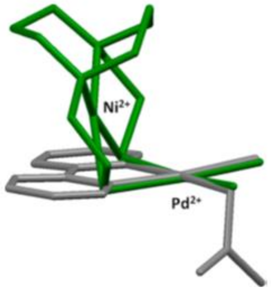

Synthesis and Characterization of Bimetallic Complexes

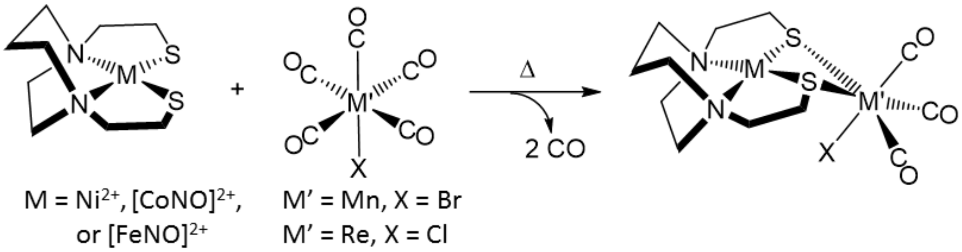

Figure VI-4. Synthetic scheme for the synthesis of the bimetallic complexes featuring the appropriate MN_2S_2 ligand bound to the Mn/Re$(CO)_3$X unit.

Figure VI-4 displays the synthetic protocol for the heterobimetallic complexes used in this study. On refluxing the metallodithiolates with the appropriate M'$(CO)_5$X compound overnight in the specified solvent, typically MeOH or DCM, two CO molecules dissociate from the Mn/Re, resulting in the binding of the dithiolate lone pairs to the metal center. Pure complexes containing Fe(NO)/Co(NO)N_2S_2 metallodithiolates were isolated after a silica gel column using CH_2Cl_2/MeOH as eluent under an inert atmosphere. The NiN_2S_2-containing complexes were purified by precipitation from a DMF solution using diethylether and are bright orange in color and air and moisture stable, but slightly light sensitive. The Fe(NO)/Co(NO)N_2S_2 analogues are dark green/brown and stable for months when stored as solids under an inert atmosphere in the dark.

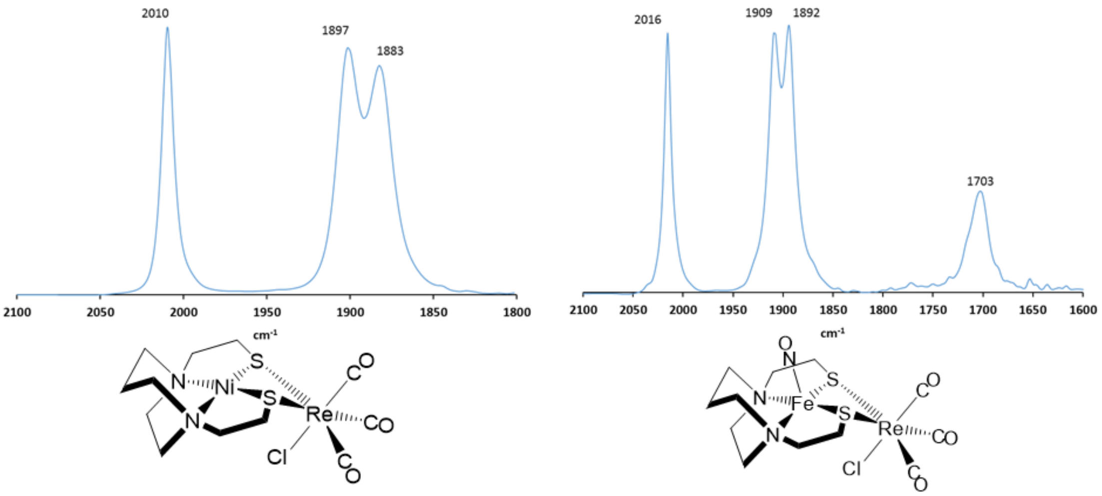

Figure VI-5. Representative IR spectra of the diatomic region of the **[Ni-Re]**, left spectrum, and **[Fe-Re]**, right spectrum, bimetallic complexes.

The ν(CO) IR spectra of the complexes feature an A_1 and a split-E stretching vibrational modes, resulting in the patter shown in Figure VI-5 for the CO stretches. All bands are shifted to lower wavenumbers compared to the $M'(bpy)(CO)_3X$ due to the greater donating ability of the metallodithiolate ligands to the Mn/Re center resulting in greater back-donation to the CO ligands.[181] Shifts are in the range of 3-17 cm^{-1} for the Re heterobimetallics and 3-15 cm^{-1} for the Mn-containing complexes. Larger shifts are observed for the NiN_2S_2 containing heterobimetallics consistent with previous studies of d^8 Ni^{II} metalloligands having a greater donating ability.[181] The ν(NO) values of the $Fe(NO)/Co(NO)N_2S_2$ containing complexes also report on the removal of electron density from the free metalloligands (ν(NO) = 1647 cm^{-1} and 1600 cm^{-1}, respectively) resulting in a NO stretch shifted to higher wavenumbers due to the depletion of electron density on the Fe/Co.[101] Two examples featuring the diatomic region of the IR spectra are seen in

Figure VI-5. The absorbance at 1703 cm^{-1}, seen in the right spectrum, is assigned to the NO stretch.

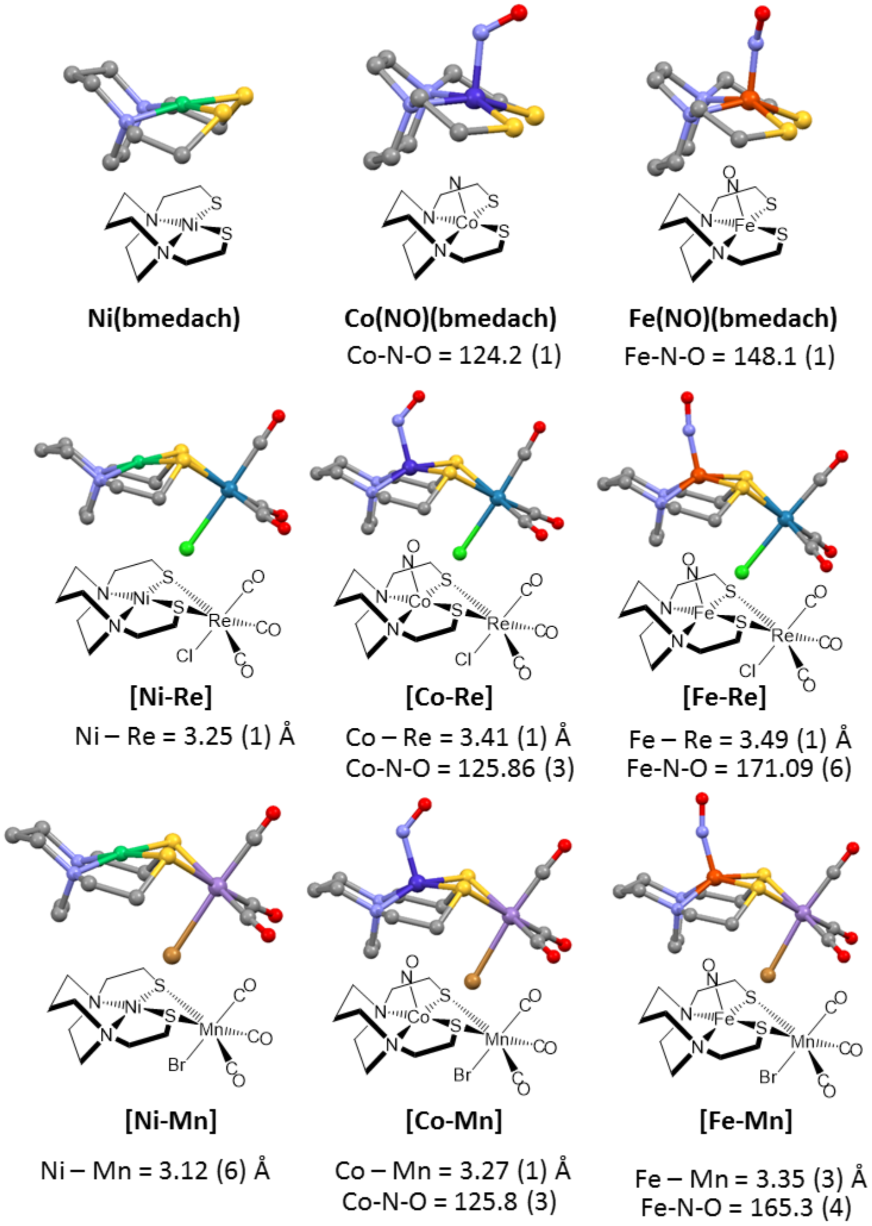

Ni(bmedach)

Co(NO)(bmedach)
Co-N-O = 124.2 (1)

Fe(NO)(bmedach)
Fe-N-O = 148.1 (1)

[Ni-Re]
Ni – Re = 3.25 (1) Å

[Co-Re]
Co – Re = 3.41 (1) Å
Co-N-O = 125.86 (3)

[Fe-Re]
Fe – Re = 3.49 (1) Å
Fe-N-O = 171.09 (6)

[Ni-Mn]
Ni – Mn = 3.12 (6) Å

[Co-Mn]
Co – Mn = 3.27 (1) Å
Co-N-O = 125.8 (3)

[Fe-Mn]
Fe – Mn = 3.35 (3) Å
Fe-N-O = 165.3 (4)

Figure VI-6. Crystal structures of the six complexes as well as the free metalloligands discussed in this study as determined by single crystal X-ray crystallography.[101,102,216]

X-ray quality crystals were grown either by slow diffusion of hexanes into a concentrated DMF solution of the Ni-containing complexes or cooling a concentrated MeCN solution to -30°C overnight for the Fe(NO)/Co(NO) derivatives, and can be seen in Figure VI-6. All structures feature an octahedral Re/Mn metal center with three linear CO ligands and an average M’-C-O angle of 177.1° to 178.6°. The halide on the group 7 metal is transoidal to the NO ligand in all cases which is nestled underneath the two metal centers in a pocket generated by the two protons directed downwards on the alpha-carbon of the N-S linker.[215] This pocket is emphasized in the space filling models displayed in Figure VI-7.

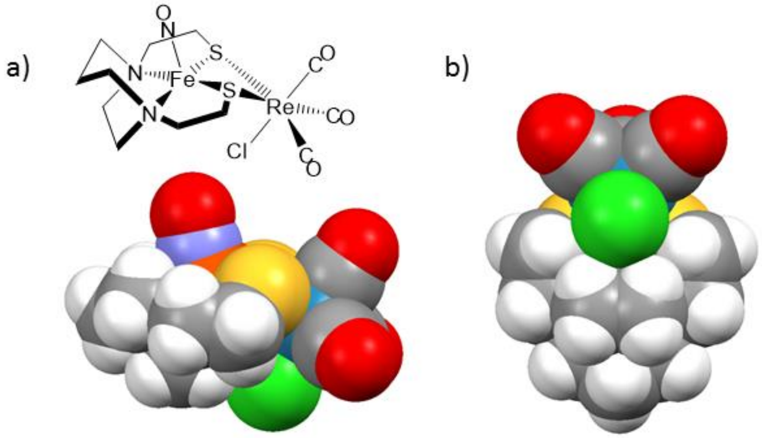

Figure VI-7. Space filling model of **[Fe-Re]** showing the pocket around the chloride which is generated by the protons on the alpha-carbon of the N-S linker.

A butterfly-like structure is present due to the orientation of the lone pairs on the sulfur atoms in the M(μ-S_2)M’ core. A hinge angle is defined as the angle of the intersection of the best N_2S_2 plane with that of the best Re/MnS_2 plane. These angles range from 127° to 131° which is similar to other MN_2S_2 bimetallics.[178,181,184,215] Alternatively, the intersection of the NiS_2/ReS_2 planes is another way of defining the hinge angle. This alternative method results in a hinge angle ranging from 135° to 148° and clearly is a factor in controlling the M-M' distance, Figure VI-8, where the distance between the two metals increase as the hinge angle increases.

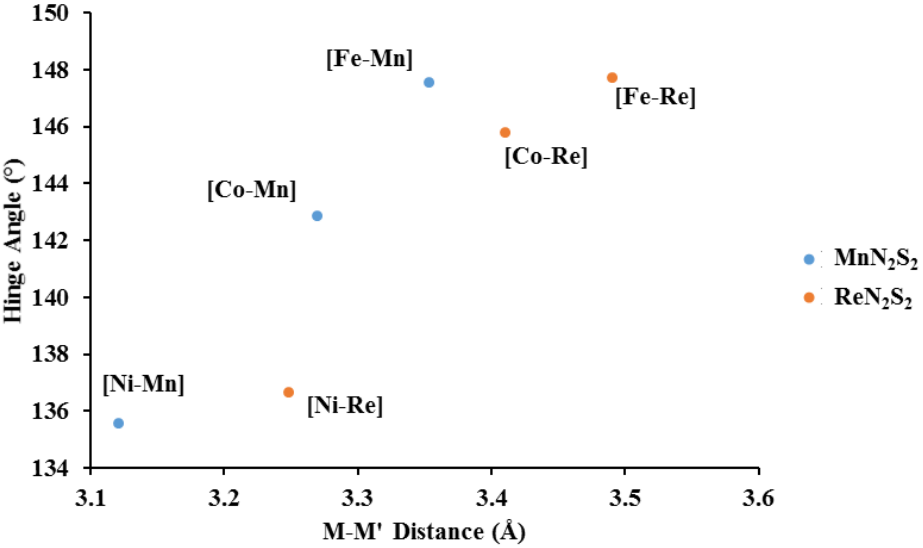

Figure VI-8. Plot of M-M' distance vs. Hinge angle determined from the intersection of the MS_2 plane with the M'S_2 plane.

M-M' distances vary based on the composition of both metal centers and correlate to the relative sizes of the Mn vs. Re and the displacement of the metal from the N_2S_2 plane. In no case is there a M-M' bond. The Ni-Re distance is ~3.27 Å and the nickel is displaced by 0.04 Å. There is an increase in the M-Re distance to 3.41 Å when the nickel is exchanged for the Co(NO) unit and is reflected in the larger displacement of the cobalt from the N_2S_2 best plane to 0.39 Å. The iron is displaced from the N_2S_2 plane by 0.57 Å but the Fe-Re distance only increases to 3.49 Å. Finally, the M-M' distance decreases by ~0.13 Å going from the rhenium complexes to the manganese complexes due to the decreased size of the manganese metal center. Upon binding the second metal center, the M-N-O angle increases 2° in the case of the Co(NO) analogues from 124° in the parent complex to 126° in the heterobimetallics.[101] The Fe-N-O angle increases more dramatically, from 148° in the parent complex to 165° in the FeMn analogue and 171° in the FeRe analogue.

EPR Spectroscopy

The Fe of the $Fe(NO)N_2S_2$ metalloligand has an ambiguous oxidation state due to the non-innocence of the NO ligand. It could be Fe^{3+}, Fe^{2+}, or Fe^{1+} depending on the assignment of the NO as NO^-, $NO\cdot$, or NO^+, respectively. This has led the scientific community to appreciate and adopt the Enemark-Feltham notation to describe the d-electron count of the M-NO.[217] Using this method the $Fe(NO)N_2S_2$ contains an $[Fe(NO)]^7$ unit with one unpaired electron making the complex paramagnetic and EPR active; the paramagnetism of this unit persists in the Re/Mn heterobimetallic complexes.[101] The Ni and Co(NO) derivatives are diamagnetic and EPR silent. All EPR spectra were recorded on a Bruker spectrometer at room temperature and simulated with SpinCount developed by Prof. M. P. Hendrich of Carnegie Mellon University.

The EPR spectrum of the parent Fe(NO)(bme-dach) complex was previously recorded but was revisited in the current study for comparison.[101] Interestingly, the published spectrum exhibited no hyperfine coupling to the ^{14}N of the nitrosyl ligand and only showed a broad, irregularly shaped isotropic signal centered at g = 2.05. Figure VI-9a displays the new spectrum which showed an isotropic triplet centered at g = 2.03 with a hyperfine coupling constant (A_{iso}) of 37 MHz arising from coupling of the unpaired electron to the I = 1 nuclear spin of the nitrosyl ligand.

Once the Fe(NO) metallodithiolate is bound to the $Re(CO)_3Cl$ center the EPR spectrum changes dramatically at room temperature, see Figure VI-9b. Now an eight-lined pattern centered at g = 2.02 is present which can be simulated with hyperfine coupling to one I = 1, ^{14}N nuclei also to the combined rhenium 185(37.4%) and 187 (62.6%) I = 5/2 nuclei. The hyperfine coupling constants are A_{iso} = 40 MHz for the 14N and A_{iso} = 38 MHz for the 185/187Re implying electronic communication between Fe(NO) unit and the Re center through the overlap of the sulfur orbitals. Notably, the **[Fe-Mn]** derivative shows no hyperfine coupling from the I = 5/2, ^{55}Mn nuclei, Figure VI-9c.

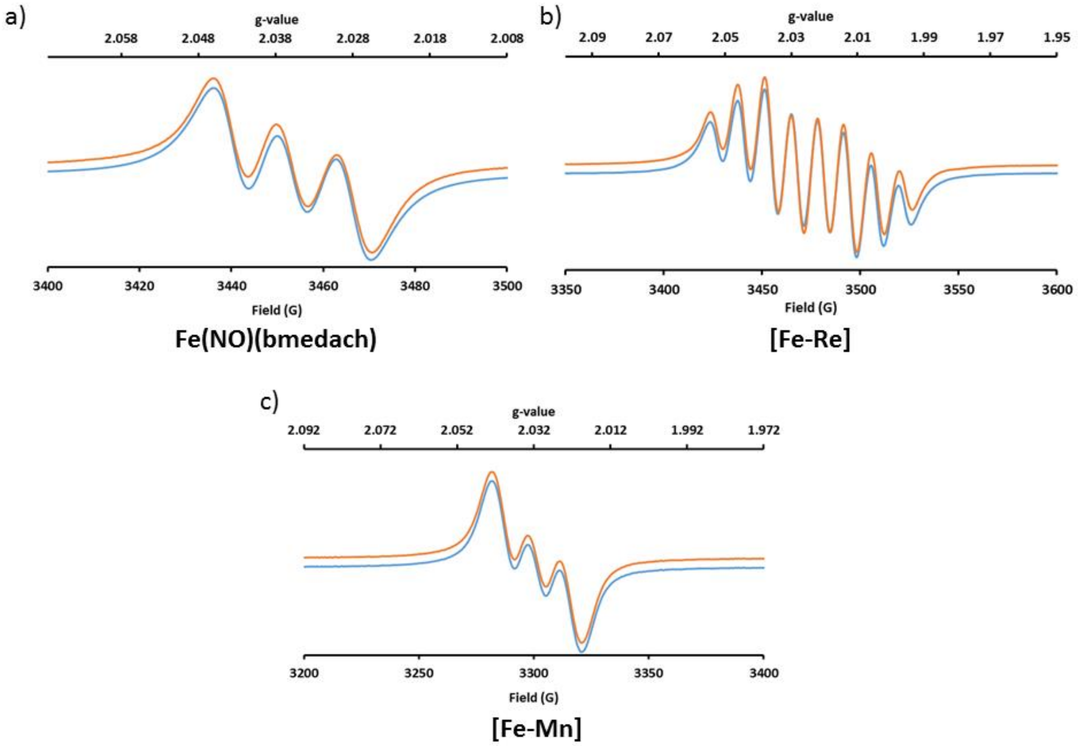

Figure VI-9. EPR spectra of a) the parent Fe(NO)(bme-dach) metalloligand, b) **[Fe-Re]**, and c) **[Fe-Mn]** recorded at room temperature in DCM. Experimental values reported in the text were obtained by simulating the spectra using SpinCount.

Electrochemistry

The cyclic voltammogram of a 2 mM solution of **[Ni-Re]** in DMF is displayed in Figure VI-10 on initiating the scan in the positive direction. The voltammogram is referenced to Fc/Fc^{+} = 0 V. Initially, the electrochemical event at $E_{1/2}$ = 0.19 V assigned to the Re$^{II/III}$ oxidation. This redox event was shown to be reversible by scan rate dependence and peak isolation as described in Chapter V. Upon scan reversal, there are three irreversible reduction events at -2.12, -2.43, and -2.67 V. Assignment of these peaks is based on the reduction potential and the difference between these redox events as compared to the Re(bipy)(CO)$_3$Cl complex. In DMF, Re(bipy)(CO)$_3$Cl shows two reduction events at -1.78 and -2.12 V which are separated by 0.34 V and both of which are irreversible.[218] A similar separation of 0.31 V is observed for the two initial reduction events of **[Ni-Re]**, so these two peaks are assigned to the Re$^{I/0}$ and Re$^{0/-I}$ reductions. These events are shifted negatively by 0.34 V and 0.31 V respectively, when compared to Re(bipy)(CO)$_3$Cl. This is ascribed to the greater donating ability of the metallodithiolate ligand compared to bipy. The most negative event at -2.67 V is assigned to the Ni$^{II/I}$ reduction.

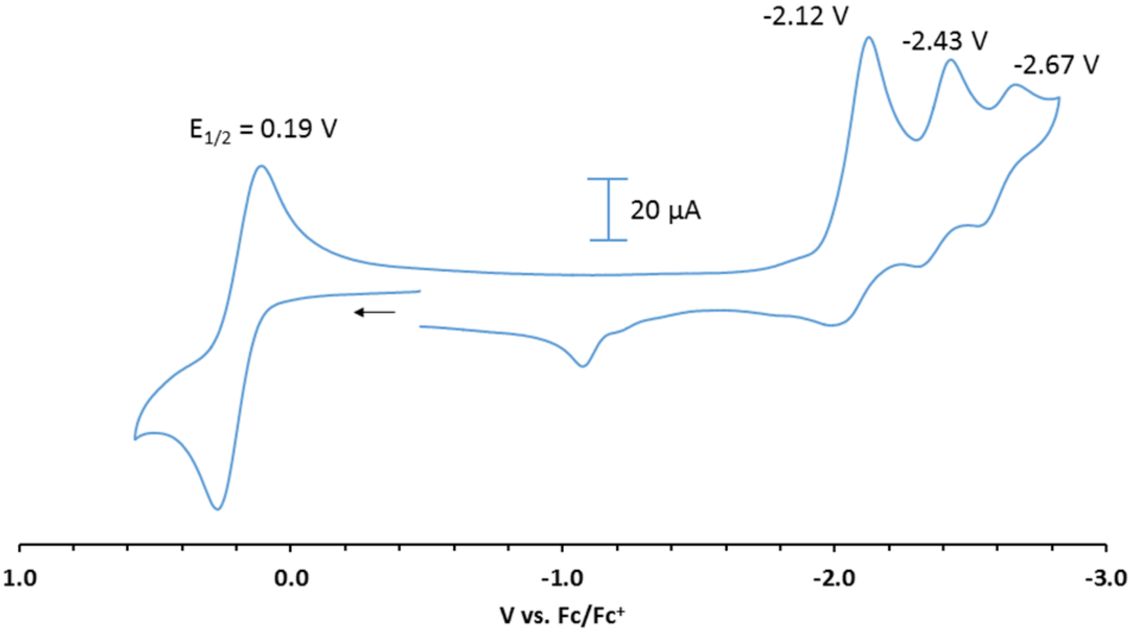

Figure VI-10. Cyclic voltammogram of 2 mM **[Ni-Re]** in DMF under an Ar atmosphere referenced to Fc/Fc$^+$ at a scan rate of 200 mV/s initiating the scan in the negative direction.

On bubbling CO_2 through the airtight cell for 15 minutes an increase in the current response at the second reduction event at -2.43 V is observed, Figure VI-11a. While Mn(bipy)$(CO)_3$Br requires an external proton source to produce a catalytic current under a CO_2 atmosphere, Re(bipy)$(CO)_3$Cl does not.[185,210-213] This has been attributed to the ability of rhenium to utilize protons from either the solvent or the electrolyte. While the **[Ni-Re]** complex displays a current enhancement with CO_2, this is further increased by the addition of a weak acid, in this case phenol. Current enhancement is attributed to the reduction of CO_2 to CO and H_2O, but further bulk electrolysis studies, sampling, and analysis are needed to confirm this observation.

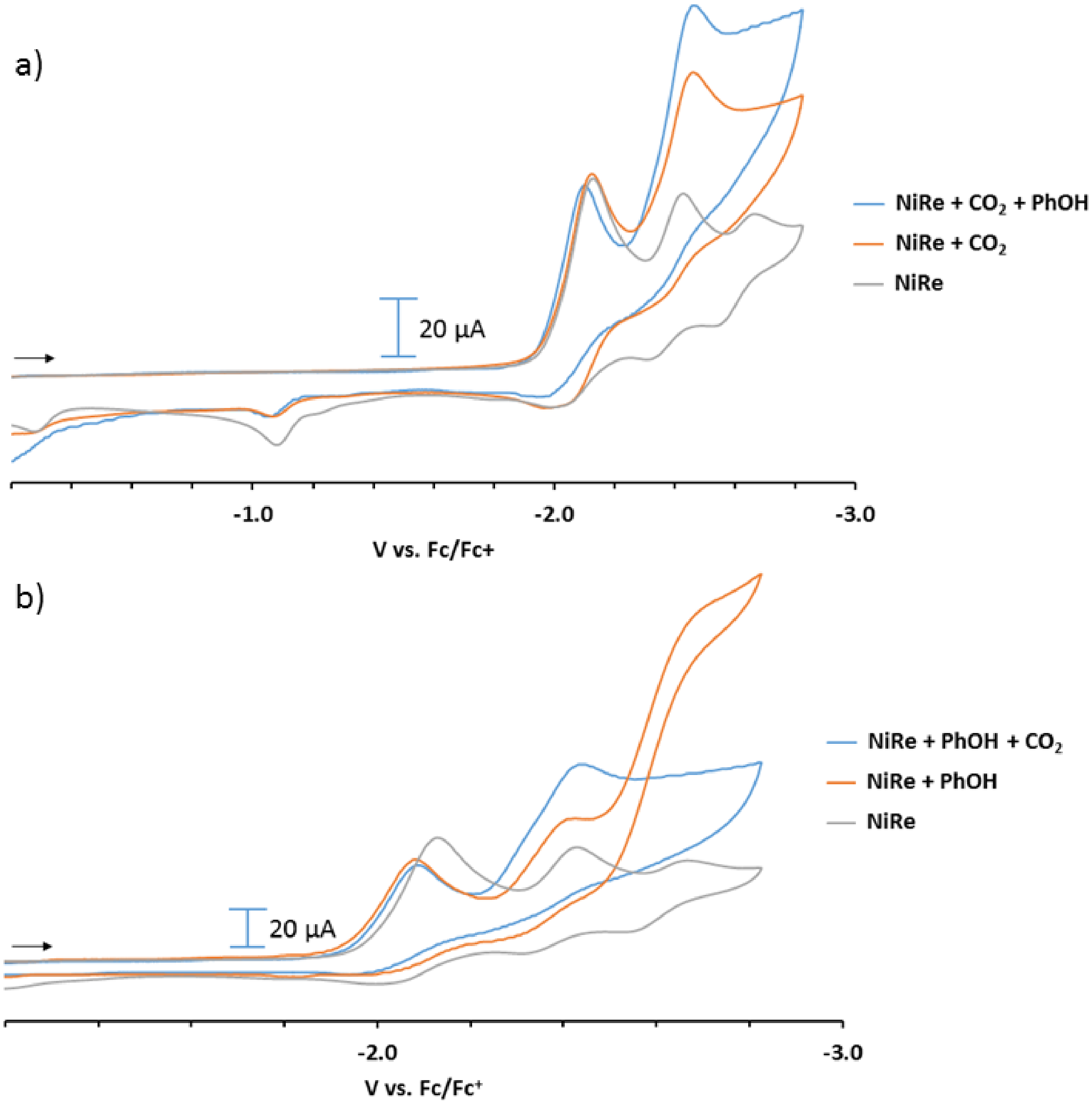

Figure VI-11. Cyclic voltammogram of 2 mM **[Ni-Re]** in DMF referenced to Fc/Fc$^+$ at a scan rate of 200 mV/s initiating the scan in the negative direction. a) **[Ni-Re]** was scanned, placed under a CO_2 atmosphere, then PhOH was added. b) **[Ni-Re]** was scanned, PhOH was added, then placed under a CO_2 atmosphere.

Whenever reducing equivalents (in this case the electrode) and protons are present, there is always the chance that protons are being reduced instead of the CO_2. On reversing the addition of presumed substrates we can observe changes in the CV and draw conclusions about the selectivity towards proton or CO_2 reduction, although ultimately bulk electrolysis is required for definitive results. When phenol is added to the electrochemical cell containing the catalyst under Ar, there is a small current enhancement in the peak at -2.43 V and a large increase at -2.67 V, Figure VI-11b. Bubbling CO_2 through the solution results in a further increase to the peak at -2.43 V and a large decrease in the peak at -2.67 V. This implies that there is probably background H_2 produced from H^+ reduction even when CO_2 is present in solution which might indicate a poor selectivity of CO_2 reduction over protons. Faradaic efficiencies for both H_2 and CO produced would support this conclusion.

Conclusions

The class of heterobimetallic complexes featuring a MN_2S_2 unit bound to a second metal center has been expanded to contain manganese and rhenium, group VII metals. Eight new complexes were synthesized and characterized using X-ray crystallography, EPR and IR spectroscopy, and cyclic voltammetry. Butterfly type structures resulted from binding of the lone pairs of the sulfur atoms to the $Re/Mn(CO)_3X$ unit, similar to previously synthesized bimetallic complexes. The NiN_2S_2 complex was the strongest σ-donating metalloligand, followed by the CoNO and FeNO complexes, but all are better donors than bipyridine. This is reflected in the shift of the CO stretching bands on the M’ and is similar to previous studies.

Electron paramagnetic resonance spectroscopy reveals coupling of the unpaired electron on the FeNO unit to the 14-N of the NO ligand in the metallodithiolate free ligand. When bound to Mn(CO)$_3$Br there is no change in the splitting pattern despite the presence of the I = 5/2 manganese center. Nevertheless, Re(CO)$_3$Cl alters the spectrum resulting in an eight-line pattern due to similar coupling of the unpaired electron to the ^{14}N and $^{185/187}$Re atoms. Hence, we conclude electronic communication exists between the iron and rhenium metals and is facilitated by the thiolate sulfur conduit.

Cyclic voltammetry of **[Ni-Re]** in DMF reveals one reversible oxidation event and three irreversible reduction events under an Ar atmosphere. Replacing the Ar atmosphere with CO$_2$ results in a current increase at the second reduction event at -2.43 V which increases further with addition of a weak acid. This may be a result of CO$_2$ reduction to CO, however bulk electrolysis and analysis is needed to affirm these conclusions.

CHAPTER VII

CONCLUDING REMARKS AND CURRENT ADVANCEMENTS

Concluding Remarks

During my time at Texas A&M University, the bioinorganic and biochemistry fields have seen great advances in the understanding of the hydrogenases, the biosynthesis of these enzymes, and the implications that features of the active sites provide towards the development of a “good” catalyst. Alongside these findings, more advanced spectroscopic and analytical techniques have become more available to the general community; they are almost necessary to publish articles in top tier journals. Many of these techniques have provided evidence for previously unobserved intermediates in catalytic cycles of both the enzymes and synthetic catalysts. Among these are advanced calculations, HYSCORE/ENDOR EPR spectroscopy, Nuclear resonance vibrational spectroscopy, bulk electrolysis measurements, and spectroelectrochemistry. In this Chapter, we will discuss the roles that these techniques have played in developing new catalytic cycles and catalysts as well as some of the more advanced complexes that have been synthesized and tested for hydrogenase activity.

Catalytic Cycle and Biohybrids

The understanding of the catalytic cycle and the involvement of all components of the H-cluster have been understood only in the last few years. Figure VII-1a displays the catalytic cycle as it was presented in 2007.[219] At this time, the identity of the central atom of the dithiolate linker was unknown from X-ray crystallography but was still expected to be NH. Nevertheless, its role as a proton shuttle was only beginning to be comprehended through DFT calculations and synthesis of model complexes.[121] This simple mechanism was the basis for all subsequent mechanisms and was built upon as further studies were done with various [FeFe]-H_2ase enzymes and more advanced EPR techniques were used.

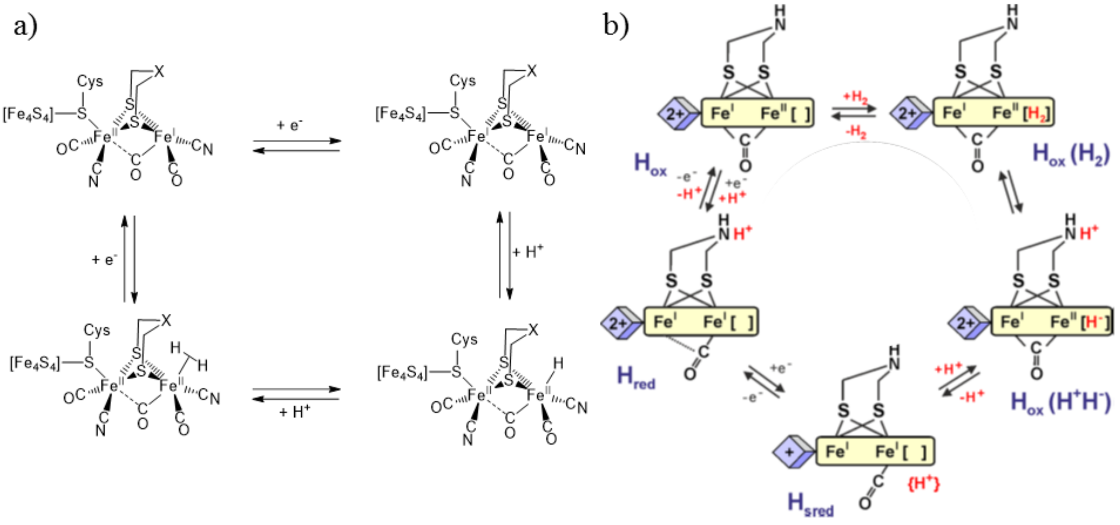

Figure VII-1. a) [FeFe]-H_2ase mechanism as proposed in 2007. b) Currently accepted mechanism (Reproduced with permission from Lubitz, W.; Ogata, H.; Rüdiger, C.; Reijerse, E. *Chemical Reviews* **2014**, *114*, 4081. Copyright **2014** American Chemical Society.[41]).

In 2012, Adamska et al. reported a new oxidation state of the enzyme termed the “super-reduced” state, see Figure VII-1b, H_{sred}.[45,49,50] This is the first time the [4Fe4S] cluster was spectroscopically observed to be reduced and the study provided a new intermediate for the catalytic cycle. The close proximity of the cluster to the 2Fe subsite implied it played a role in catalysis, but the extent to which it did was unknown until this study. Interestingly, an [FeFe]-H_2ase from a different organism was used which lacked a [4Fe4S] cluster necessary to relay electrons to the outside of the protein. Under catalytic conditions, this deficiency trapped the H_{sred} state of the enzyme and allowed it to be spectroscopically observed by EPR spectroscopy; it featured a reduced [4Fe4S] cluster as well as an Fe^IFe^I within the 2Fe unit. It is carefully designed experiments such as these, coupled with thorough spectroscopic characterization, that has led to huge advances in understanding the catalytic cycle of [FeFe]-H_2ase.

As mentioned above, the unambiguous assignment of the central atom of the S to S linker was also recently confirmed and has led to a reinvigoration of the synthetic community alongside the discovery of model insertion into apo-proteins, see Figure I-3. Prior to the synthesis and characterization of these biohybrids, careful labeling and ENDOR/HYSCORE studies provided evidence of the identity of this bridgehead atom within the S to S linker.[26,41,42,51] The final nail in the coffin came about when these biohybrids were tested for their hydrogen production abilities and it was found that only the NH bridgehead retained 100% catalytic activity as compared to the enzyme.[28,29] This has led the hydrogenase community to definitively conclude that the central atom is in fact a NH and not a CH_2 or O. Again, cutting-edge experiments and characterization have not only led to deciphering the identity of a single atom from a crystal structure, but have also led to a whole new field within the hydrogenase subfield based on the synthesis of biohybrids. For example, those with O or CH_2 in the bridgehead might be used to build up the concentration of proposed intermediates.

During the course of my graduate studies, it was reported that model complexes could initially be inserted into apo-HydF which is identified as a maturation protein in the biosynthesis of the 2Fe subunit.[28] Electron paramagnetic resonance and infrared spectroscopies were pivotal in determining how and where the diiron complex was located in the protein structure. It was revealed that the 2Fe unit was bound through the cyanide to the [4Fe4S] cluster and the orientation of the cyanide had flipped in the docking process. HYSCORE was used to make this assignment using ^{13}C labeled cyanide. While this finding may be debated, the pivotal roles that EPR, IR, and HYSCORE spectroscopies have played in analyzing these proteins is obvious.

Advances in Model Complexes

At the start of my graduate career, Helm et al. published a paper reporting a nickel electrocatalyst with a TOF of 100,000 s^{-1} for H_2 production.[196] A development in the Dubois team at PNNL, was inspired by the [FeFe]-H_2ase enzyme and was built around the idea of incorporating a pendant amine in the second coordination sphere for proton relay to the nickel. Ring strain in the ligand discouraged binding of the amine to the metal center and placed the nitrogen in optimum proximity to the nickel. Since then, this has become the paradigm by which all other proton reduction catalysts have been compared.

Due to the ease of the ligand framework seen in Figure VII-2, any number of functional groups can be incorporated into the pendant amines allowing for the electronics and sterics around the nitrogen to be tuned.[191] This also provides ways of introducing groups for immobilizing the metal complexes on electrodes, nanoparticles, and solid supports.[220] The phosphines can also be tuned to provide steric encumbrance around the metal center or tune their σ-donating ability.[31-33,190-192,196,197]

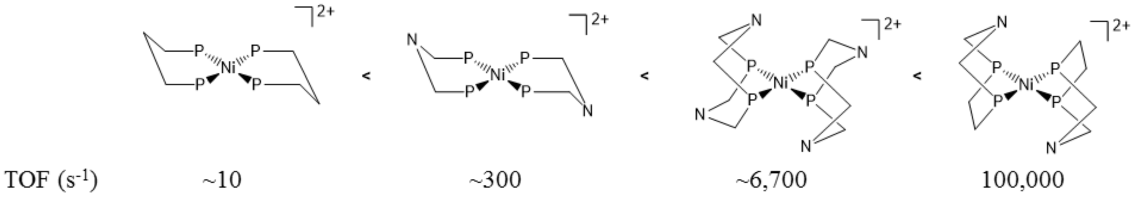

Figure VI-2. Catalyst evolution leading to the high TOF displayed in the $[Ni(P_2N)_2]^{2+}$ system. Functional groups on the phosphines and nitrogens have been removed for clarity.

Obviously this complex was not developed overnight, and it took a huge team to fully explore all the chemistry, performed largely at the PNNL. It is a good example of how catalyst optimization should be approached, given sufficient resources. Figure VII-2 displays the evolutionary steps that took place to reach this high TOF. This is also a good example where understanding the drawbacks to the current generation of catalysts can help develop and improve the design and further advance catalyst performance. It has been known for fifteen years that NiP_4 homogeneous catalysts could electrocatalytically produce H_2, albeit at fairly low TOF.[221] To possibly increase the catalytic activity, a pendant base was introduced into the second coordination sphere, modeling the NH unit of [FeFe]-H_2ase.[220,221] While there was not a dramatic increase in TOF, Small et al. realized the nitrogen had too much freedom to move and they were not actually positioned in an optimum location above the nickel center.[192] By introducing a second pendant amine to each phosphine ligand one of the NR groups would be sterically forced to reside above the nickel in ideal proximity to act as a proton relay.[190] This produced a proton reduction catalyst with a fairly high TOF, but again the catalyst suffered from drawbacks. Namely, the nitrogens on one of the phosphine ligands had a tendency to reside in a catalytically inactive, pinched-back confirmation with a proton being shared between the two amines. Finally, to overcome this problem, one of the pendant amines was removed and replaced with an ethylene group which would still force the remaining NR unit to reside above the nickel but the catalyst would not suffer from the inactive confirmation.[196] This resulted in a remarkable TOF of 33,000 s^{-1}. The group at PNNL took it one step further and actually added aliquots of water to the cyclic voltammetry cell further increasing the TOF to 106,000 s^{-1}.

Since the report of these huge advances in the electro-/photocatalytic reduction of protons, a huge variety of R-groups on both the nitrogens and the phosphines have been synthesized and attached to most of the d-block metals. These new catalysts have found application in not only proton reduction and hydrogen oxidation, but also in CO_2 reduction and nitrogen fixation.[31,33,222] While not every catalytic reaction saw the dramatic increase the proton reduction community saw when incorporating a pendant base, understanding how and why there was or was not an increase in catalytic activity, followed by making improvements to the ligand system to combat these problems, is what will drive this field to further advances.

Expectations in Electrochemical Characterizations

I was very involved in developing, instructing, and performing electrochemical characterizations of not only my complexes but also complexes from group members. Since the start of my graduate career, the scientific community has developed a greater understanding of what makes a “good” electrocatalyst, as outlined in Chapter X, and has come to expect more advanced techniques along with computational backup. Examples of these are bulk electrolysis for confirmation that current enhancements observed in CV corresponds to the expected catalytic reaction and spectroelectrochemistry to confirm redox assignments in the CV and to inspire “stalking” bulk samples of such reduced and oxidized species.

Five plus years ago it was acceptable to simply observe changes in the CV upon addition of a substrate and simply draw a conclusion regarding the identity of any observed current enhancement. Our group as well as others have found that this is a poor way of assigning catalytic activity. We have seen in at least one example where a current enhancement upon addition of acid in the CV was assigned to hydrogen production, but when bulk electrolysis was performed there was no detectable H_2 formed.[178] If bulk electrolysis was not done, this would have resulted in false assignment of the current increase. Similarly, CO_2 reduction can result in numerous different products or product distributions which cannot be assigned by simple CV but requires bulk electrolysis. Catalyst stability and Faradaic efficiencies can also be obtained from bulk electrolysis but sometimes not from cyclic voltammetry.

These issues have led to the requirement that bulk electrolysis experiments must be performed to back up CV assignments of catalytic activity, especially for publication in top tier journals. Turn-over-number, Faradaic efficiencies, TOF (obtained from CV), and overpotential (obtained from CV) have become the norm for ranking and evaluating electrocatalysts. Any number of these characterizations might have been left out or not reported in the publication five years ago.

Saveant and coworkers have been forerunners in the electrochemistry world, pioneering electrochemical calculations and characterizations including calculating TOF.[206,207] Two methods have been developed for TOF calculations using CV; the foot-of-the-wave analysis, or the ratio of current in the presence and absence of substrate, i_{cat}/i_p. Both methods have their drawbacks under certain situations but still provide a simpler method for calculating TOF without having to do advanced calculations and electrochemical measurements. It should be noted that these numbers typically reflect the maximum TOF under first order conditions.

Future Outlook

While advances have been made in my time at Texas A&M University, there is always room to learn more. Our understanding of the maturation cycle of [FeFe]-H_2ase has made leaps and bounds over the last five years as outlined in Chapter I, but there are still unanswered questions. The major one being what is the role of the HydE maturase? If it does synthesize the dithiolate linker, how does it do it? What is the substrate? I believe these will be the next major discoveries dealing with the protein.

Alongside the major advances with the protein have been a better understanding and incorporation of features of the hydrogenase active sites into synthetic model complexes and electrocatalysts. Metallothiolates have emerged as possible proton relays, as exemplified in [NiFe]-H_2ase, and I believe this field will continue to expand just as the NiP_2N_2 field has done. This is due to the possibility of synthesizing numerous complexes with different metals in the N_2S_2 binding pocket as well as changing the second metal to which the dithiolates are bridged. These catalysts have already found utility in proton reduction and H_2 oxidation studies but, I believe, will find future applications in CO_2 reduction as well as possibly N_2 fixation.

I have been greatly impressed by the advances made in the last five years of hydrogen producing/hydrogen oxidizing catalyst development and understanding of the enzymes. I look forward with great anticipation the next five years.

REFERENCES

(1) Häussinger, P.; Lohmüller, R.; Watson, A. M. In *Ullmann's Encyclopedia of Industrial Chemistry*; Wiley-VCH Verlag GmbH & Co. KGaA: 2000.

(2) Le Goff, A.; Artero, V.; Jousselme, B.; Tran, P. D.; Guillet, N.; Métayé, R.; Fihri, A.; Palacin, S.; Fontecave, M. *Science* **2009**, *326*, 1384.

(3) Jacques, P.-A.; Artero, V.; Pécaut, J.; Fontecave, M. *Proc. Natl. Acad. Sci. U.S.A.* **2009**, *106*, 20627.

(4) Gordon, R. B.; Bertram, M.; Graedel, T. E. *Proc. Natl. Acad. Sci. U.S.A.* **2006**, *103*, 1209.

(5) Eberle, U.; Felderhoff, M.; Schüth, F. *Angew. Chem. Int. Ed.* **2009**, *48*, 6608.

(6) Gasteiger, H. A.; Marković, N. M. *Science* **2009**, *324*, 48.

(7) Hambourger, M.; Kodis, G.; Vaughn, M. D.; Moore, G. F.; Gust, D.; Moore, A. L.; Moore, T. A. *Dalton Trans.* **2009**, 9979.

(8) Vignais, P. M.; Billoud, B. *Chem. Rev.* **2007**, *107*, 4206.

(9) Van Der Spek, T. M.; Arendsen, A. F.; Happe, R. P.; Yun, S.; Bagley, K. A.; Stufkens, D. J.; Hagen, W. R.; Albracht, S. P. J. *Eur. J. Biochem.* **1996**, *237*, 629.

(10) Roseboom, W.; De Lacey, A. L.; Fernandez, V. M.; Hatchikian, E. C.; Albracht, S. P. J. *JBIC Journal of Biological Inorganic Chemistry* **2006**, *11*, 102.

(11) Pierik, A. J.; Hulstein, M.; Hagen, W. R.; Albracht, S. P. J. *Eur. J. Biochem.* **1998**, *258*, 572.

(12) Chen, Z.; Lemon, B. J.; Huang, S.; Swartz, D. J.; Peters, J. W.; Bagley, K. A. *Biochemistry* **2002**, *41*, 2036.

(13) De Lacey, A. L.; Fernández, V. M.; Rousset, M.; Cammack, R. *Chem. Rev.* **2007**, *107*, 4304.

(14) Peters, J. W.; Lanzilotta, W. N.; Lemon, B. J.; Seefeldt, L. C. *Science* **1998**, *282*, 1853.

(15) Mulder, David W.; Shepard, Eric M.; Meuser, Jonathan E.; Joshi, N.; King, Paul W.; Posewitz, Matthew C.; Broderick, Joan B.; Peters, John W. *Structure* **2011**, *19*, 1038.

(16) Hiromoto, T.; Warkentin, E.; Moll, J.; Ermler, U.; Shima, S. *Angew. Chem. Int. Ed.* **2009**, *48*, 6457.

(17) Fontecilla-Camps, C. J. *JBIC Journal of Biological Inorganic Chemistry* **1996**, *1*, 91.

(18) Shima, S.; Thauer, R. K. *The Chemical Record* **2007**, *7*, 37.

(19) Fontecilla-Camps, J. C.; Volbeda, A.; Cavazza, C.; Nicolet, Y. *Chem. Rev.* **2007**, *107*, 4273.

(20) Nicolet, Y.; Lemon, B. J.; Fontecilla-Camps, J. C.; Peters, J. W. *Trends Biochem. Sci* **2000**, *25*, 138.

(21) Vignais, P. M.; Billoud, B.; Meyer, J. *FEMS Microbiology Reviews* **2001**, *25*, 455.

(22) Bethel, R. D.; Darensbourg, M. Y. In *Bioorganometallic Chemistry*; Wiley-VCH Verlag GmbH & Co. KGaA: 2014, p 239.

(23) Volbeda, A.; Charon, M.-H.; Piras, C.; Hatchikian, E. C.; Frey, M.; Fontecilla-Camps, J. C. *Nature* **1995**, *373*, 580.

(24) Nicolet, Y.; de Lacey, A. L.; Vernède, X.; Fernandez, V. M.; Hatchikian, E. C.; Fontecilla-Camps, J. C. *J. Am. Chem. Soc.* **2001**, *123*, 1596.

(25) Silakov, A.; Wenk, B.; Reijerse, E.; Lubitz, W. *PCCP* **2009**, *11*, 6592.

(26) Erdem, Ö. F.; Schwartz, L.; Stein, M.; Silakov, A.; Kaur-Ghumaan, S.; Huang, P.; Ott, S.; Reijerse, E. J.; Lubitz, W. *Angew. Chem. Int. Ed.* **2011**, *50*, 1439.

(27) Siegbahn, P. E. M.; Tye, J. W.; Hall, M. B. *Chem. Rev.* **2007**, *107*, 4414.

(28) Berggren, G.; Adamska, A.; Lambertz, C.; Simmons, T. R.; Esselborn, J.; Atta, M.; Gambarelli, S.; Mouesca, J. M.; Reijerse, E.; Lubitz, W.; Happe, T.; Artero, V.; Fontecave, M. *Nature* **2013**, *499*, 66.

(29) Esselborn, J.; Lambertz, C.; Adamska-Venkatesh, A.; Simmons, T.; Berggren, G.; Noth, J.; Siebel, J.; Hemschemeier, A.; Artero, V.; Reijerse, E.; Fontecave, M.; Lubitz, W.; Happe, T. *Nat Chem Biol* **2013**, *9*, 607.

(30) Helm, M. L.; Stewart, M. P.; Bullock, R. M.; DuBois, M. R.; DuBois, D. L. *Science* **2011**, *333*, 863.

(31) Liu, T.; Chen, S.; O'Hagan, M. J.; Rakowski DuBois, M.; Bullock, R. M.; DuBois, D. L. *J. Am. Chem. Soc.* **2012**, *134*, 6257.

(32) Liu, T.; DuBois, D. L.; Bullock, R. M. *Nat Chem* **2013**, *5*, 228.

(33) Liu, T.; Wang, X.; Hoffmann, C.; DuBois, D. L.; Bullock, R. M. *Angew. Chem. Int. Ed.* **2014**, *53*, 5300.

(34) Pandey, A. S.; Harris, T. V.; Giles, L. J.; Peters, J. W.; Szilagyi, R. K. *J. Am. Chem. Soc.* **2008**, *130*, 4533.

(35) Siebel, J. F.; Adamska-Venkatesh, A.; Weber, K.; Rumpel, S.; Reijerse, E.; Lubitz, W. *Biochemistry* **2015**, *54*, 1474.

(36) Knörzer, P.; Silakov, A.; Foster, C. E.; Armstrong, F. A.; Lubitz, W.; Happe, T. *J. Biol. Chem.* **2012**, *287*, 1489.

(37) Fontecilla-Camps, J. C.; Amara, P.; Cavazza, C.; Nicolet, Y.; Volbeda, A. *Nature* **2009**, *460*, 814.

(38) Niu, S.; Hall, M. B. *Inorg. Chem.* **2001**, *40*, 6201.

(39) Ogata, H.; Nishikawa, K.; Lubitz, W. *Nature* **2015**, *520*, 571.

(40) Happe, R. P.; Roseboom, W.; Pierik, A. J.; Albracht, S. P. J.; Bagley, K. A. *Nature* **1997**, *385*, 126.

(41) Lubitz, W.; Ogata, H.; Rüdiger, O.; Reijerse, E. *Chem. Rev.* **2014**, *114*, 4081.

(42) Lubitz, W.; Reijerse, E.; van Gastel, M. *Chem. Rev.* **2007**, *107*, 4331.

(43) De Lacey, A. L.; Santamaria, E.; Hatchikian, E. C.; Fernandez, V. M. *Biochimica et Biophysica Acta (BBA) - Protein Structure and Molecular Enzymology* **2000**, *1481*, 371.

(44) Ogata, H.; Hirota, S.; Nakahara, A.; Komori, H.; Shibata, N.; Kato, T.; Kano, K.; Higuchi, Y. *Structure* **2005**, *13*, 1635.

(45) Adamska, A.; Silakov, A.; Lambertz, C.; Rüdiger, O.; Happe, T.; Reijerse, E.; Lubitz, W. *Angew. Chem. Int. Ed.* **2012**, *51*, 11458.

(46) Goldet, G.; Brandmayr, C.; Stripp, S. T.; Happe, T.; Cavazza, C.; Fontecilla-Camps, J. C.; Armstrong, F. A. *J. Am. Chem. Soc.* **2009**, *131*, 14979.

(47) Montet, Y.; Amara, P.; Volbeda, A.; Vernede, X.; Hatchikian, E. C.; Field, M. J.; Frey, M.; Fontecilla-Camps, J. C. *Nat Struct Mol Biol* **1997**, *4*, 523.

(48) Dementin, S.; Leroux, F.; Cournac, L.; Lacey, A. L. d.; Volbeda, A.; Léger, C.; Burlat, B.; Martinez, N.; Champ, S.; Martin, L.; Sanganas, O.; Haumann, M.; Fernández, V. M.; Guigliarelli, B.; Fontecilla-Camps, J. C.; Rousset, M. *J. Am. Chem. Soc.* **2009**, *131*, 10156.

(49) Adamska-Venkatesh, A.; Krawietz, D.; Siebel, J.; Weber, K.; Happe, T.; Reijerse, E.; Lubitz, W. *J. Am. Chem. Soc.* **2014**, *136*, 11339.

(50) Adamska-Venkatesh, A.; Simmons, T. R.; Siebel, J. F.; Artero, V.; Fontecave, M.; Reijerse, E.; Lubitz, W. *PCCP* **2015**, *17*, 5421.

(51) Silakov, A.; Kamp, C.; Reijerse, E.; Happe, T.; Lubitz, W. *Biochemistry* **2009**, *48*, 7780.

(52) Artero, V.; Fontecave, M. *Coord. Chem. Rev.* **2005**, *249*, 1518.

(53) Nicolet, Y.; Fontecilla-Camps, J. C. *J. Biol. Chem.* **2012**, *287*, 13532.

(54) Dinis, P.; Suess, D. L. M.; Fox, S. J.; Harmer, J. E.; Driesener, R. C.; De La Paz, L.; Swartz, J. R.; Essex, J. W.; Britt, R. D.; Roach, P. L. *Proc. Natl. Acad. Sci. U.S.A.* **2015**, *112*, 1362.

(55) Mulder, D. W.; Ortillo, D. O.; Gardenghi, D. J.; Naumov, A. V.; Ruebush, S. S.; Szilagyi, R. K.; Huynh, B.; Broderick, J. B.; Peters, J. W. *Biochemistry* **2009**, *48*, 6240.

(56) Kuchenreuther, J. M.; Myers, W. K.; Stich, T. A.; George, S. J.; NejatyJahromy, Y.; Swartz, J. R.; Britt, R. D. *Science* **2013**, *342*, 472.

(57) Kuchenreuther, J. M.; Myers, W. K.; Suess, D. L. M.; Stich, T. A.; Pelmenschikov, V.; Shiigi, S. A.; Cramer, S. P.; Swartz, J. R.; Britt, R. D.; George, S. J. *Science* **2014**, *343*, 424.

(58) Suess, D. L. M.; Pham, C. C.; Bürstel, I.; Swartz, J. R.; Cramer, S. P.; Britt, R. D. *J. Am. Chem. Soc.* **2016**, *138*, 1146.

(59) McGlynn, S. E.; Shepard, E. M.; Winslow, M. A.; Naumov, A. V.; Duschene, K. S.; Posewitz, M. C.; Broderick, W. E.; Broderick, J. B.; Peters, J. W. *FEBS Lett.* **2008**, *582*, 2183.

(60) Shepard, E. M.; McGlynn, S. E.; Bueling, A. L.; Grady-Smith, C. S.; George, S. J.; Winslow, M. A.; Cramer, S. P.; Peters, J. W.; Broderick, J. B. *Proc. Natl. Acad. Sci. U.S.A.* **2010**, *107*, 10448.

(61) Rohac, R.; Amara, P.; Benjdia, A.; Martin, L.; Ruffié, P.; Favier, A.; Berteau, O.; Mouesca, J.-M.; Fontecilla-Camps, J. C.; Nicolet, Y. *Nat Chem* **2016**, *8*, 491.

(62) Mulder, D. W.; Boyd, E. S.; Sarma, R.; Lange, R. K.; Endrizzi, J. A.; Broderick, J. B.; Peters, J. W. *Nature* **2010**, *465*, 248.

(63) Esselborn, J.; Muraki, N.; Klein, K.; Engelbrecht, V.; Metzler-Nolte, N.; Apfel, U. P.; Hofmann, E.; Kurisu, G.; Happe, T. *Chem. Sci.* **2016**, *7*, 959.

(64) Reihlen, H.; Gruhl, A.; v. Hessling, G. *Justus Liebigs Annalen der Chemie* **1929**, *472*, 268.

(65) Woolerton, T. W.; Sheard, S.; Chaudhary, Y. S.; Armstrong, F. A. *Energy Environ. Sci.* **2012**, *5*, 7470.

(66) Cracknell, J. A.; Vincent, K. A.; Armstrong, F. A. *Chem. Rev.* **2008**, *108*, 2439.

(67) Caserta, G.; Roy, S.; Atta, M.; Artero, V.; Fontecave, M. *Curr. Opin. Chem. Biol.* **2015**, *25*, 36.

(68) Tard, C.; Pickett, C. J. *Chem. Rev.* **2009**, *109*, 2245.

(69) Lyon, E. J.; Georgakaki, I. P.; Reibenspies, J. H.; Darensbourg, M. Y. *J. Am. Chem. Soc.* **2001**, *123*, 3268.

(70) Le Cloirec, A.; C. Davies, S.; J. Evans, D.; L. Hughes, D.; J. Pickett, C.; P. Best, S.; Borg, S. *Chem. Commun.* **1999**, 2285.

(71) Lyon, E. J.; Georgakaki, I. P.; Reibenspies, J. H.; Darensbourg, M. Y. *Angew. Chem. Int. Ed.* **1999**, *38*, 3178.

(72) Li, H.; Rauchfuss, T. B. *J. Am. Chem. Soc.* **2002**, *124*, 726.

(73) Stanley, J. L.; Heiden, Z. M.; Rauchfuss, T. B.; Wilson, S. R.; De Gioia, L.; Zampella, G. *Organometallics* **2008**, *27*, 119.

(74) Stanley, J. L.; Rauchfuss, T. B.; Wilson, S. R. *Organometallics* **2007**, *26*, 1907.

(75) Singleton, M. L.; Jenkins, R. M.; Klemashevich, C. L.; Darensbourg, M. Y. *C. R. Chim.* **2008**, *11*, 861.

(76) Crouthers, D. J.; Denny, J. A.; Bethel, R. D.; Munoz, D. G.; Darensbourg, M. Y. *Organometallics* **2014**, *33*, 4747.

(77) Bethel, R. D.; Crouthers, D. J.; Hsieh, C.-H.; Denny, J. A.; Hall, M. B.; Darensbourg, M. Y. *Inorg. Chem.* **2015**, *54*, 3523.

(78) Darensbourg, M. Y.; Lyon, E. J.; Zhao, X.; Georgakaki, I. P. *Proc. Natl. Acad. Sci. U.S.A.* **2003**, *100*, 3683.

(79) Li, B.; Liu, T.; Singleton, M. L.; Darensbourg, M. Y. *Inorg. Chem.* **2009**, *48*, 8393.

(80) Liu, T.; Darensbourg, M. Y. *J. Am. Chem. Soc.* **2007**, *129*, 7008.

(81) Singleton, M. L.; Bhuvanesh, N.; Reibenspies, J. H.; Darensbourg, M. Y. *Angew. Chem. Int. Ed.* **2008**, *47*, 9492.

(82) George, S. J.; Cui, Z.; Razavet, M.; Pickett, C. J. *Chem. Eur. J.* **2002**, *8*, 4037.

(83) Gloaguen, F.; Lawrence, J. D.; Schmidt, M.; Wilson, S. R.; Rauchfuss, T. B. *J. Am. Chem. Soc.* **2001**, *123*, 12518.

(84) Wang, M.; Chen, L.; Li, X.; Sun, L. *Dalton Trans.* **2011**, *40*, 12793.

(85) Barber, J.; Tran, P. D. *J. R. Soc. Interface* **2013**, *10*.

(86) Chenevier, P.; Mugherli, L.; Darbe, S.; Darchy, L.; DiManno, S.; Tran, P. D.; Valentino, F.; Iannello, M.; Volbeda, A.; Cavazza, C.; Artero, V. *C. R. Chim.* **2013**, *16*, 491.

(87) Sun, L.; Åkermark, B.; Ott, S. *Coord. Chem. Rev.* **2005**, *249*, 1653.

(88) Pullen, S.; Fei, H.; Orthaber, A.; Cohen, S. M.; Ott, S. *J. Am. Chem. Soc.* **2013**, *135*, 16997.

(89) Jian, J.-X.; Ye, C.; Wang, X.-Z.; Wen, M.; Li, Z.-J.; Li, X.-B.; Chen, B.; Tung, C.-H.; Wu, L.-Z. *Energy Environ. Sci.* **2016**, *9*, 2083.

(90) Camara, J. M.; Rauchfuss, T. B. *Nat Chem* **2012**, *4*, 26.

(91) Zheng, D.; Wang, N.; Wang, M.; Ding, S.; Ma, C.; Darensbourg, M. Y.; Hall, M. B.; Sun, L. *J. Am. Chem. Soc.* **2014**, *136*, 16817.

(92) Winter, A.; Zsolnai, L.; Huttner, G. *Z. Naturforsch* **1982**, *37*, 1430.

(93) Reger, D. L.; Coleman, C. *J. Organomet. Chem.* **1977**, *131*, 153.

(94) Eugene Coffey, C. *J. Inorg. Nucl. Chem.* **1963**, *25*, 179.

(95) El-Tarhuni, S.; Ho, M.; Kawser, M. H.; Shi, S.; Whiteley, M. W. *J. Organomet. Chem.* **2014**, *752*, 30.

(96) Chen, C. H.; Liaw, W. F. *Inorg. Synth.* **2010**, *35*, 129.

(97) Zhao, X.; Georgakaki, I. P.; Miller, M. L.; Yarbrough, J. C.; Darensbourg, M. Y. *J. Am. Chem. Soc.* **2001**, *123*, 9710.

(98) Smith, C. R.; Zhang, A.; Mans, D. J.; RajanBabu, T. V. *Org. Synth.* **2008**, *85*, 248.

(99) Zheng, J.; Misal Castro, L. C.; Roisnel, T.; Darcel, C.; Sortais, J.-B. *Inorg. Chim. Acta* **2012**, *380*, 301.

(100) Nehring, J. L.; Heinekey, D. M. *Inorg. Chem.* **2003**, *42*, 4288.

(101) Chiang, C.-Y.; Lee, J.; Dalrymple, C.; Sarahan, M. C.; Reibenspies, J. H.; Darensbourg, M. Y. *Inorg. Chem.* **2005**, *44*, 9007.

(102) Smee, J. J.; Miller, M. L.; Grapperhaus, C. A.; Reibenspies, J. H.; Darensbourg, M. Y. *Inorg. Chem.* **2001**, *40*, 3601.

(103) Inc., B. A. Madison, WI, 2007.

(104) Inc., B. A. Madison, WI, 2007.

(105) Sheldrick, G. *Acta Crystallographica Section A* **2008**, *64*, 112.

(106) Barbour, L. J. *J. Supramol. Chem.* **2003**, *1*, 189.

(107) Frisch, M. J.; Trucks, G. W.; Schlegel, H. B.; Scuseria, G. E.; Robb, M. A.; Cheeseman, J. R.; Scalmani, G.; Barone, V.; Mennucci, B.; Petersson, G. A.; Nakatsuji, H.; Caricato, M.; Li, X.; Hratchian, H. P.; Izmaylov, A. F.; Bloino, J.; Zheng, G.; Sonnenberg, J. L.; Hada, M.; Ehara, M.; Toyota, K.; Fukuda, R.; Hasegawa, J.; Ishida, M.; Nakajima, T.; Honda, Y.; Kitao, O.; Nakai, H.; Vreven, T.; Montgomery Jr., J. A.; Peralta, J. E.; Ogliaro, F.; Bearpark, M. J.; Heyd, J.; Brothers, E. N.; Kudin, K. N.; Staroverov, V. N.; Kobayashi, R.; Normand, J.; Raghavachari, K.; Rendell, A. P.; Burant, J. C.; Iyengar, S. S.; Tomasi, J.; Cossi, M.; Rega, N.; Millam, N. J.; Klene, M.; Knox, J. E.; Cross, J. B.; Bakken, V.; Adamo, C.; Jaramillo, J.; Gomperts, R.; Stratmann, R. E.; Yazyev, O.; Austin, A. J.; Cammi, R.; Pomelli, C.; Ochterski, J. W.; Martin, R. L.; Morokuma, K.; Zakrzewski, V. G.; Voth, G. A.; Salvador, P.; Dannenberg, J. J.; Dapprich, S.; Daniels, A. D.; Farkas, Ö.; Foresman, J. B.; Ortiz, J. V.; Cioslowski, J.; Fox, D. J.; Gaussian, Inc.: Wallingford, CT, USA, 2009.

(108) Becke, A. D. *J. Chem. Phys.* **1993**, *98*, 5648.

(109) McLean, A. D.; Chandler, G. S. *J. Chem. Phys.* **1980**, *72*, 5639.

(110) Clark, T.; Chandrasekhar, J.; Spitznagel, G. W.; Schleyer, P. V. R. *J. Comput. Chem.* **1983**, *4*, 294.

(111) Hehre, W. J.; Ditchfield, R.; Pople, J. A. *J. Chem. Phys.* **1972**, *56*, 2257.

(112) Francl, M. M.; Pietro, W. J.; Hehre, W. J.; Binkley, J. S.; Gordon, M. S.; DeFrees, D. J.; Pople, J. A. *J. Chem. Phys.* **1982**, *77*, 3654.

(113) Wachters, A. J. H. *J. Chem. Phys.* **1970**, *52*, 1033.

(114) Hay, P. J. *J. Chem. Phys.* **1977**, *66*, 4377.

(115) Marenich, A. V.; Cramer, C. J.; Truhlar, D. G. *The Journal of Physical Chemistry B* **2009**, *113*, 6378.

(116) Grimme, S.; Antony, J.; Ehrlich, S.; Krieg, H. *J. Chem. Phys.* **2010**, *132*, 154104.

(117) Grimme, S.; Ehrlich, S.; Goerigk, L. *J. Comput. Chem.* **2011**, *32*, 1456.

(118) Neese, F. *Wiley Interdisciplinary Reviews: Computational Molecular Science* **2012**, *2*, 73.

(119) Weigend, F.; Ahlrichs, R. *PCCP* **2005**, *7*, 3297.

(120) Muhammad, S.; Moncho, S.; Brothers, E. N.; Darensbourg, M. Y.; Darensbourg, D. J.; Bengali, A. A. *Inorg. Chem.* **2012**, *51*, 7362.

(121) Fan, H.-J.; Hall, M. B. *J. Am. Chem. Soc.* **2001**, *123*, 3828.

(122) Liu, Z.-P.; Hu, P. *J. Chem. Phys.* **2002**, *117*, 8177.

(123) Lunsford, A. M.; Beto, C. C.; Ding, S.; Erdem, O. F.; Wang, N.; Bhuvanesh, N.; Hall, M. B.; Darensbourg, M. Y. *Chem. Sci.* **2016**, *7*, 3710.

(124) Scott, M. J.; Holm, R. H. *J. Am. Chem. Soc.* **1994**, *116*, 11357.

(125) Lim, B. S.; Holm, R. H. *Inorg. Chem.* **1998**, *37*, 4898.

(126) Shatruk, M.; Dragulescu-Andrasi, A.; Chambers, K. E.; Stoian, S. A.; Bominaar, E. L.; Achim, C.; Dunbar, K. R. *J. Am. Chem. Soc.* **2007**, *129*, 6104.

(127) Zhu, N.; Vahrenkamp, H. *Chem. Ber.* **1997**, *130*, 1241.

(128) Bignozzi, C. A.; Argazzi, R.; Schoonover, J. R.; Gordon, K. C.; Dyer, R. B.; Scandola, F. *Inorg. Chem.* **1992**, *31*, 5260.

(129) Kettle, S. F. A.; Diana, E.; Boccaleri, E.; Stanghellini, P. L. *Inorg. Chem.* **2007**, *46*, 2409.

(130) Boyer, J. L.; Rauchfuss, T. B.; Wilson, S. R. *C. R. Chim.* **2008**, *11*, 922.

(131) Manor, B. C.; Rauchfuss, T. B. *J. Am. Chem. Soc.* **2013**, *135*, 11895.

(132) Manor, B. C.; Ringenberg, M. R.; Rauchfuss, T. B. *Inorg. Chem.* **2014**, *53*, 7241.

(133) Artero, V.; Fontecave, M. *C. R. Chim.* **2008**, *11*, 926.

(134) Stoll, S.; Schweiger, A. *Journal of Magnetic Resonance* **2006**, *178*, 42.

(135) Erdem, Ö. F.; Stein, M.; Kaur-Ghumaan, S.; Reijerse, E. J.; Ott, S.; Lubitz, W. *Chem. Eur. J.* **2013**, *19*, 14566.

(136) Baraban, J. H.; Changala, P. B.; Mellau, G. C.; Stanton, J. F.; Merer, A. J.; Field, R. W. *Science* **2015**, *350*, 1338.

(137) Ramabhadran, R. O.; Hua, Y.; Flood, A. H.; Raghavachari, K. *The Journal of Physical Chemistry A* **2014**, *118*, 7418.

(138) Stephens, F. H.; Pons, V.; Tom Baker, R. *Dalton Trans.* **2007**, 2613.

(139) Smythe, N. C.; Gordon, J. C. *Eur. J. Inorg. Chem.* **2010**, *2010*, 509.

(140) Staubitz, A.; Robertson, A. P. M.; Manners, I. *Chem. Rev.* **2010**, *110*, 4079.

(141) Li, H.; Yang, Q.; Chen, X.; Shore, S. G. *J. Organomet. Chem.* **2014**, *751*, 60.

(142) Alcaraz, G.; Sabo-Etienne, S. *Angew. Chem. Int. Ed.* **2010**, *49*, 7170.

(143) Abboud, J.-L. M.; Németh, B.; Guillemin, J.-C.; Burk, P.; Adamson, A.; Nerut, E. R. *Chem. Eur. J.* **2012**, *18*, 3981.

(144) Leitao, E. M.; Stubbs, N. E.; Robertson, A. P. M.; Helten, H.; Cox, R. J.; Lloyd-Jones, G. C.; Manners, I. *J. Am. Chem. Soc.* **2012**, *134*, 16805.

(145) Al-Kukhun, A.; Hwang, H. T.; Varma, A. *Int. J. Hydrogen Energy* **2013**, *38*, 169.

(146) Stubbs, N. E.; Robertson, A. P. M.; Leitao, E. M.; Manners, I. *J. Organomet. Chem.* **2013**, *730*, 84.

(147) Johnson, H. C.; Hooper, T. N.; Weller, A. S. In *Synthesis and Application of Organoboron Compounds*; Fernández, E., Whiting, A., Eds.; Springer International Publishing: Cham, 2015, p 153.

(148) Keaton, R. J.; Blacquiere, J. M.; Baker, R. T. *J. Am. Chem. Soc.* **2007**, *129*, 1844.

(149) Yang, X.; Hall, M. B. *J. Am. Chem. Soc.* **2008**, *130*, 1798.

(150) Zimmerman, P. M.; Paul, A.; Zhang, Z.; Musgrave, C. B. *Angew. Chem. Int. Ed.* **2009**, *48*, 2201.

(151) Vogt, M.; de Bruin, B.; Berke, H.; Trincado, M.; Grutzmacher, H. *Chem. Sci.* **2011**, *2*, 723.

(152) Sutton, A. D.; Burrell, A. K.; Dixon, D. A.; Garner, E. B.; Gordon, J. C.; Nakagawa, T.; Ott, K. C.; Robinson, J. P.; Vasiliu, M. *Science* **2011**, *331*, 1426.

(153) Davis, B. L.; Dixon, D. A.; Garner, E. B.; Gordon, J. C.; Matus, M. H.; Scott, B.; Stephens, F. H. *Angew. Chem. Int. Ed.* **2009**, *48*, 6812.

(154) Tang, Z.; Chen, H.; Chen, X.; Wu, L.; Yu, X. *J. Am. Chem. Soc.* **2012**, *134*, 5464.

(155) Ramachandran, P. V.; Gagare, P. D. *Inorg. Chem.* **2007**, *46*, 7810.

(156) Hausdorf, S.; Baitalow, F.; Wolf, G.; Mertens, F. O. R. L. *Int. J. Hydrogen Energy* **2008**, *33*, 608.

(157) Summerscales, O. T.; Gordon, J. C. *Dalton Trans.* **2013**, *42*, 10075.

(158) Lunsford, A. M.; Blank, J. H.; Moncho, S.; Haas, S. C.; Muhammad, S.; Brothers, E. N.; Darensbourg, M. Y.; Bengali, A. A. *Inorg. Chem.* **2016**, *55*, 964.

(159) Lachaize, S.; Essalah, K.; Montiel-Palma, V.; Vendier, L.; Chaudret, B.; Barthelat, J.-C.; Sabo-Etienne, S. *Organometallics* **2005**, *24*, 2935.

(160) Kawano, Y.; Yamaguchi, K.; Miyake, S.-y.; Kakizawa, T.; Shimoi, M. *Chem. Eur. J.* **2007**, *13*, 6920.

(161) Dallanegra, R.; Chaplin, A. B.; Weller, A. S. *Angew. Chem. Int. Ed.* **2009**, *48*, 6875.

(162) Sohail, M.; Moncho, S.; Brothers, E. N.; Darensbourg, D. J.; Bengali, A. A. *Dalton Trans.* **2013**, *42*, 6720.

(163) Lin, T.-P.; Peters, J. C. *J. Am. Chem. Soc.* **2013**, *135*, 15310.

(164) Darensbourg, M. Y.; Bau, R.; Marks, M. W.; Burch, R. R.; Deaton, J. C.; Slater, S. *J. Am. Chem. Soc.* **1982**, *104*, 6961.

(165) Kirtley, S. W.; Andrews, M. A.; Bau, R.; Grynkewich, G. W.; Marks, T. J.; Tipton, D. L.; Whittlesey, B. R. *J. Am. Chem. Soc.* **1977**, *99*, 7154.

(166) Vance, J. R.; Schäfer, A.; Robertson, A. P. M.; Lee, K.; Turner, J.; Whittell, G. R.; Manners, I. *J. Am. Chem. Soc.* **2014**, *136*, 3048.

(167) Wang, N.; Wang, M.; Wang, Y.; Zheng, D.; Han, H.; Ahlquist, M. S. G.; Sun, L. *J. Am. Chem. Soc.* **2013**, *135*, 13688.

(168) Sloan, M. E.; Staubitz, A.; Clark, T. J.; Russell, C. A.; Lloyd-Jones, G. C.; Manners, I. *J. Am. Chem. Soc.* **2010**, *132*, 3831.

(169) Douglas, T. M.; Chaplin, A. B.; Weller, A. S.; Yang, X.; Hall, M. B. *J. Am. Chem. Soc.* **2009**, *131*, 15440.

(170) Shimoi, M.; Nagai, S.-i.; Ichikawa, M.; Kawano, Y.; Katoh, K.; Uruichi, M.; Ogino, H. *J. Am. Chem. Soc.* **1999**, *121*, 11704.

(171) Kakizawa, T.; Kawano, Y.; Naganeyama, K.; Shimoi, M. *Chem. Lett.* **2011**, *40*, 171.

(172) Buss, J. A.; Edouard, G. A.; Cheng, C.; Shi, J.; Agapie, T. *J. Am. Chem. Soc.* **2014**, *136*, 11272.

(173) Muhammad, S.; Moncho, S.; Brothers, E. N.; Bengali, A. A. *Chem. Commun.* **2014**, *50*, 5874.

(174) Li, H.; Wang, X.; Huang, F.; Lu, G.; Jiang, J.; Wang, Z.-X. *Organometallics* **2011**, *30*, 5233.

(175) Baker, R. T.; Gordon, J. C.; Hamilton, C. W.; Henson, N. J.; Lin, P.-H.; Maguire, S.; Murugesu, M.; Scott, B. L.; Smythe, N. C. *J. Am. Chem. Soc.* **2012**, *134*, 5598.

(176) Marziale, A. N.; Friedrich, A.; Klopsch, I.; Drees, M.; Celinski, V. R.; Schmedt auf der Günne, J.; Schneider, S. *J. Am. Chem. Soc.* **2013**, *135*, 13342.

(177) Can, M.; Armstrong, F. A.; Ragsdale, S. W. *Chem. Rev.* **2014**, *114*, 4149.

(178) Hsieh, C.-H.; Ding, S.; Erdem, O. F.; Crouthers, D. J.; Liu, T.; McCrory, C. C. L.; Lubitz, W.; Popescu, C. V.; Reibenspies, J. H.; Hall, M. B.; Darensbourg, M. Y. *Nat Commun* **2014**, *5*.

(179) Ogo, S.; Ichikawa, K.; Kishima, T.; Matsumoto, T.; Nakai, H.; Kusaka, K.; Ohhara, T. *Science* **2013**, *339*, 682.

(180) Nguyen, N. T.; Mori, Y.; Matsumoto, T.; Yatabe, T.; Kabe, R.; Nakai, H.; Yoon, K.-S.; Ogo, S. *Chem. Commun.* **2014**, *50*, 13385.

(181) Denny, J. A.; Darensbourg, M. Y. *Chem. Rev.* **2015**, *115*, 5248.

(182) Schilter, D.; Camara, J. M.; Huynh, M. T.; Hammes-Schiffer, S.; Rauchfuss, T. B. *Chem. Rev.* **2016**, *116*, 8693.

(183) Ogo, S. *Coord. Chem. Rev.*

(184) Ding, S.; Ghosh, P.; Lunsford, A. M.; Wang, N.; Bhuvanesh, N.; Hall, M. B.; Darensbourg, M. Y. *J. Am. Chem. Soc.* **2016**.

(185) Benson, E. E.; Kubiak, C. P.; Sathrum, A. J.; Smieja, J. M. *Chem. Soc. Rev.* **2009**, *38*, 89.

(186) Scholz, F.; Bond, A. M. *Electroanalytical methods : guide to experiments and applications. F. Scholz (ed.) ; with contributions by A.M. Bond [and others]*; Berlin ; New York : Springer, [2002], 2002.

(187) Bond, A. M.; Coomber, D. C.; Feldberg, S. W.; Oldham, K. B.; Vu, T. *Anal. Chem.* **2001**, *73*, 352.

(188) Pavlishchuk, V. V.; Addison, A. W. *Inorg. Chim. Acta* **2000**, *298*, 97.

(189) Scott, R. A.; Lukehart, C. M. *Applications of physical methods to inorganic and bioinorganic chemistry. editors, Robert A. Scott, Charles M. Lukehart*; Hoboken, N.J. : John Wiley & Sons, [2007], 2007.

(190) Wiese, S.; Kilgore, U. J.; DuBois, D. L.; Bullock, R. M. *ACS Catal.* **2012**, *2*, 720.

(191) Kilgore, U. J.; Roberts, J. A. S.; Pool, D. H.; Appel, A. M.; Stewart, M. P.; DuBois, M. R.; Dougherty, W. G.; Kassel, W. S.; Bullock, R. M.; DuBois, D. L. *J. Am. Chem. Soc.* **2011**, *133*, 5861.

(192) Small, Y. A.; DuBois, D. L.; Fujita, E.; Muckerman, J. T. *Energy Environ. Sci.* **2011**, *4*, 3008.

(193) McCarthy, B. D.; Martin, D. J.; Rountree, E. S.; Ullman, A. C.; Dempsey, J. L. *Inorg. Chem.* **2014**, *53*, 8350.

(194) Felton, G. A. N.; Vannucci, A. K.; Chen, J.; Lockett, L. T.; Okumura, N.; Petro, B. J.; Zakai, U. I.; Evans, D. H.; Glass, R. S.; Lichtenberger, D. L. *J. Am. Chem. Soc.* **2007**, *129*, 12521.

(195) Fourmond, V.; Jacques, P.-A.; Fontecave, M.; Artero, V. *Inorg. Chem.* **2010**, *49*, 10338.

(196) Helm, M. L.; Stewart, M. P.; Bullock, R. M.; DuBois, M. R.; DuBois, D. L. *Science* **2011**, *333*, 863.

(197) Rakowski DuBois, M.; DuBois, D. L. *Chem. Soc. Rev.* **2009**, *38*, 62.

(198) Kilgore, U. J.; Stewart, M. P.; Helm, M. L.; Dougherty, W. G.; Kassel, W. S.; DuBois, M. R.; DuBois, D. L.; Bullock, R. M. *Inorg. Chem.* **2011**, *50*, 10908.

(199) Appel, A. M.; Helm, M. L. *ACS Catal.* **2014**, *4*, 630.

(200) Smieja, J. M.; Benson, E. E.; Kumar, B.; Grice, K. A.; Seu, C. S.; Miller, A. J. M.; Mayer, J. M.; Kubiak, C. P. *Proc. Natl. Acad. Sci. U.S.A.* **2012**, *109*, 15646.

(201) Cheng, T.-Y.; Bullock, R. M. *J. Am. Chem. Soc.* **1999**, *121*, 3150.

(202) Sutin, N.; Creutz, C.; Fujita, E. *Comments Inorg. Chem.* **1997**, *19*, 67.

(203) Appel, A. M.; Bercaw, J. E.; Bocarsly, A. B.; Dobbek, H.; DuBois, D. L.; Dupuis, M.; Ferry, J. G.; Fujita, E.; Hille, R.; Kenis, P. J. A.; Kerfeld, C. A.; Morris, R. H.; Peden, C. H. F.; Portis, A. R.; Ragsdale, S. W.; Rauchfuss, T. B.; Reek, J. N. H.; Seefeldt, L. C.; Thauer, R. K.; Waldrop, G. L. *Chem. Rev.* **2013**, *113*, 6621.

(204) Morris, A. J.; Meyer, G. J.; Fujita, E. *Acc. Chem. Res.* **2009**, *42*, 1983.

(205) Grice, K. A.; Kubiak, C. P. In *Adv. Inorg. Chem.*; Michele, A., Rudi van, E., Eds.; Academic Press: 2014; Vol. Volume 66, p 163.

(206) Costentin, C.; Robert, M.; Savéant, J.-M. *Acc. Chem. Res.* **2015**, *48*, 2996.

(207) Costentin, C.; Drouet, S.; Robert, M.; Savéant, J.-M. *J. Am. Chem. Soc.* **2012**, *134*, 11235.

(208) Bourrez, M.; Molton, F.; Chardon-Noblat, S.; Deronzier, A. *Angew. Chem. Int. Ed.* **2011**, *50*, 9903.

(209) Sampson, M. D.; Nguyen, A. D.; Grice, K. A.; Moore, C. E.; Rheingold, A. L.; Kubiak, C. P. *J. Am. Chem. Soc.* **2014**, *136*, 5460.

(210) Smieja, J. M.; Kubiak, C. P. *Inorg. Chem.* **2010**, *49*, 9283.

(211) Keith, J. A.; Grice, K. A.; Kubiak, C. P.; Carter, E. A. *J. Am. Chem. Soc.* **2013**, *135*, 15823.

(212) Riplinger, C.; Sampson, M. D.; Ritzmann, A. M.; Kubiak, C. P.; Carter, E. A. *J. Am. Chem. Soc.* **2014**, *136*, 16285.

(213) Machan, C. W.; Sampson, M. D.; Chabolla, S. A.; Dang, T.; Kubiak, C. P. *Organometallics* **2014**, *33*, 4550.

(214) Sampson, M. D.; Froehlich, J. D.; Smieja, J. M.; Benson, E. E.; Sharp, I. D.; Kubiak, C. P. *Energy Environ. Sci.* **2013**, *6*, 3748.

(215) Denny, J. A.; Darensbourg, M. Y. *Coord. Chem. Rev.* **2016**, *324*, 82.

(216) Hess, J. L.; Conder, H. L.; Green, K. N.; Darensbourg, M. Y. *Inorg. Chem.* **2008**, *47*, 2056.

(217) Enemark, J. H.; Feltham, R. D. *Coord. Chem. Rev.* **1974**, *13*, 339.

(218) Hawecker, J.; Lehn, J.-M.; Ziessel, R. *J. Chem. Soc., Chem. Commun.* **1984**, 328.

(219) Thomas, C. M.; Darensbourg, M. Y.; Hall, M. B. *J. Inorg. Biochem.* **2007**, *101*, 1752.

(220) Seo, J.; Pekarek, R. T.; Rose, M. J. *Chem. Commun.* **2015**, *51*, 13264.

(221) Curtis, C. J.; Miedaner, A.; Ciancanelli, R.; Ellis, W. W.; Noll, B. C.; Rakowski DuBois, M.; DuBois, D. L. *Inorg. Chem.* **2003**, *42*, 216.

(222) Lilio, A. M.; Reineke, M. H.; Moore, C. E.; Rheingold, A. L.; Takase, M. K.; Kubiak, C. P. *J. Am. Chem. Soc.* **2015**, *137*, 8251.